STUDY OF THE EFFECTS OF SURFACE CLADDING ON 3D TRANSMON

BY

ZACHARY ROBERT YOSCOVITS

DISSERTATION

Submitted in partial fulfillment of the requirements
for the degree of Doctor of Philosophy in Physics
in the Graduate College of the
University of Illinois at Urbana-Champaign, 2014

Urbana, Illinois

Doctoral Committee:

Professor Alexey Bezryadin, Chair
Professor James Eckstein, Director of Research
Professor Smitha Vishveshwara
Professor Matthias Grosse Perdekamp

Abstract

Quantum computing is a very interesting field, due to the ability of quantum computers to solve many problems much faster than a classical computer. Superconducting qubits are electronic circuits composed of superconducting capacitors, inductors and Josephson junctions, which can implement a physical qubit. However they need improvements in their coherence time to create a viable quantum computing. In this work I study the effect on decoherence caused by two level systems in the native oxide that forms on the surface of qubit. To this end I fabricate 3D transmon qubits using materials grown my molecular beam epitaxy, to which a variety of different surface treatments had been applied.

I began by fabricating qubits from niobium/aluminum oxide/niobium trilayers. To this end I developed a self-aligned process for fabricating sub-micron Josephson junctions. This process presented many challenges. During the development of this process, it became clear that niobium was an inferior material for fabricating qubits compared to aluminum.

I then switched to making qubits from Aluminum. I began by studying the growth of aluminum on sapphire, and was able to achieve aluminum films with an RMS roughness of 0.2 nm by growing on c-plane sapphire that had been annealed in oxygen at 1100 °C and dipped in BOE.

Next I fabricated 3D transmon qubits by adapting the standard shadowmask process for use with MBE. I fabricated qubits with a long in situ oxidation to fully passivate the surface before exposure to air. I also passivated the surface by means of growing co deposited aluminum oxide, and by grown aluminum nitride using a nitrogen plasma source. The coherence times of these qubits were compared to those a control sample that had been exposed to air immediately after growth. Overall it doesn't appear that cladding the surface changes the coherence time much, however it is difficult to form conclusions with this small sample size. The coated samples appeared to have slightly longer coherence times than the untreated samples, with diffusive

oxidation and coating with aluminum oxide providing the largest increase in T_1 and diffusive oxidation providing the largest increase in T_2.

To my wife Jenna

Acknowledgements

I could not have completed this work without the help of many people. First I would like to thank my advisor, Professor James Eckstein for his support and guidance throughout my graduate school career.

I would like to thank the other members of the Eckstein Group, especially Allison Dove and Gus Olson who collaborated with me on the portion of this work dealing with niobium qubits which would not have been possible without them. I would also like to thank labmates Brian Mulcahy, Carolyn Kan, Can Zhang, Xiaoxiao Wang, and Che Xue for many interesting discussions about physics and their willingness to lend a hand when needed. To my former labmates Stephanie Law, Mao Zheng, and Chandra Mohapatra, I would like to say thank you for the guidance and mentoring.

I would also like to thank several other research groups. First of all I would like to thank Jaseung Ku in the Bezryadin group for preforming the qubit measurements presented in chapter 5; his work was critical to the success of this project. Next I would like to thank the Van Harlingen group here at UIUC as well as the Siddiqi Clarke groups, at University of California Berkeley for collaborating with us in the study of qubits.

I would like to that the dedicated staff at the Frederick Seitz Materials Research Laboratory Center for Microanalysis of Materials, especially Scott MacLaren for his expertise in AFM and J. G. Wen for TEM work. To the staff of the Microfabrication Facility, expecially Tony Banks, Bharat Sankaran, Mike Marshal, Tao Shang, and Shivakumar Bhaskaran, thank you for training me to use the fabrication equipment and keeping the facility running.

A special thanks to Doug Jeffers, who taught me the finer details of the maintenance and repair of the MBE system, and without whom my MBE chamber would have fallen into disrepair long ago.

Finally, I would like to thank my wife, Jenna, for her support and encouragement. She put up with my strange hours at work, and drove to the lab many rainy nights to drive me home. And

thank you to my family, my parents, Greg and Denise and my brother, Chad, thank you for all of the love and support you have provided my whole life.

This material was based in part on work supported by IARPA. This work was carried out in part in the Frederick Seitz Materials Research Laboratory Central Facilities, University of Illinois.

Table of Contents

Chapter 1 Introduction and motivation

Quantum computing is a field of great interest. This is due to the ability to use the properties of quantum mechanics to perform many functions faster than a classical computer. This includes factoring large numbers [1], searching a database [2], and simulating physical systems [3]. Building a quantum computer presents a serious technological challenge. However, in the past decade there has been tremendous progress toward the development of a quantum computer [4]. There are many systems in which work on quantum computing is being done. Such systems usually use microscopic degrees of freedom such as the polarization of single photons [5], excitations in trapped atoms [6], and nuclear spins [7]. These systems can be well isolated from their environment and thus exhibit long coherence times, but they present challenges to scalability due to the difficulty in interacting with them. Work focuses on the use of collective modes in macroscopic superconducting circuits as qubit states. Standard electrical circuits decohere very quickly due to resistive dissipation, so superconducting circuits which have no dissipation must be used. Superconducting qubits rely on Josephson junctions to provide the nonlinearity necessary to achieve an effective two state system.

Superconducting circuits are an ideal system for quantum computing for many reasons. First, being electronic circuits, with macroscopic degrees of freedom such as current and voltage they are easy to interact with. Second, they are fabricated using many of the same techniques as conventional integrated circuits, which allows for the ease of scalability. Also because the excitation energy is controlled by the circuit elements, superconducting qubits can be designed to have whatever frequency is desired (typically 5-10 GHz to be higher than thermal excitations, but low enough for ease of microwave engineering [4]). The challenge with superconducting qubits is that being macroscopic and well coupled to the environment they have much larger decoherence than microscopic systems. Great advancements have been made in the coherence times of superconducting qubits [8]. Coherence times have improved from the order of one nanosecond from the first demonstrated superconducting qubit in 1999 [9] to coherence times approaching 100 microseconds [10]. These advancements have been made both by designing

the qubits to be insensitive to particular sources of noise, and by improving materials in order to reduce the noise. This work takes the latter approach.

Once source of noise that is thought to be particularly important to the decoherence of qubits is two level systems in amorphous dielectrics [11] such as the native oxide on the surface of the superconductor. In this work, I attempt to increase the coherence time of transmon qubits by protecting the surface of the qubit structures from the formation of a native oxide by coating them with an in situ dielectric. This in situ dielectric should have fewer two level systems than the native oxide, resulting in longer coherence times. I used molecular beam epitaxy to grow my materials due to its ability to grow pure materials, with clean interfaces.

I present in this work my findings on niobium and aluminum qubits. I started with the fabrication of Josephson junctions from niobium trilayers, developing a self-aligned process to fabricate the small (one square micron or less) junctions necessary for qubits. However, it became apparent that aluminum is a more suitable material then niobium. My focus then shifted to fabricating qubits from aluminum, adapting standard shadowmask fabrication process for use with molecular beam epitaxy. I present my findings on the effect of in situ diffusive oxidation and the growth of co-deposited aluminum oxide and aluminum nitride cladding layers on the coherence times of 3D transmon qubits.

In chapter two I survey the relevant background material, discussing quantum computing, particularly superconducting qubits as well as the causes of decoherence. I present my work on niobium junctions and qubits in chapter three. Following that I present my procedure for growing aluminum films and fabricating qubits in chapter four. Chapter five contains my findings on the effect of the cladding layers on the coherence time of the qubits. I conclude with a summary of my findings and suggestions for future work in chapter six.

Chapter 2 Background

In this chapter I present the background necessary to follow the rest of this work. I begin by discussing quantum computing in general. Next I discuss superconducting qubits in particular. I present the charge qubit and show how by modifying the characteristic energy of the Josephson junction compared to the characteristic energy of the capacitor, one can make a transmon qubit which is insensitive to charge noise. I then discuss decoherence, which can be characterized by two timescales, the relaxation time and the dephasing time. I will explain how these times are measured on qubits. Then I will explain what are believed to be the major causes of decoherence, and present recent advancement in coherence made by others. Finally I will present my proposed solution to decoherence, which is to protect the surface of the qubit from forming a native oxide by growing an in situ cladding layer on it.

2.1 Quantum Computing

Although the transistors at the heart of computers rely on quantum mechanics, the treatment of the information in the computer is inherently classical. The full specification of the state at any instant is a set of numbers all of which are in principle measurable [12] Feynman showed that one cannot efficiently simulate quantum systems with a classical computer, but you could do it with a quantum computer [3]. In addition to speeding up simulations, quantum computers can also be used to solve certain problems faster than classical computers. One of the earliest quantum algorithms found was the Deutsch–Jozsa algorithm which provides an exponential speedup in discovering whether a black box function is constant or balanced [13]. Although this algorithm doesn't have any practical use, it does serve to illustrate the potential for quantum computing to solve some problems faster than classical computing. A more useful algorithm, in fact probably the main reason that quantum computing has received so much attention, is Shor's algorithm. Shor's algorithm provides an exponential speedup in factoring integers into their prime factors [1]. Another useful algorithm is Grover's algorithm which provides a quadratic speed-up in searching an unstructured database [2].

Just as classical computers are composed of bits that can either be in a 1 or 0 state, a quantum computer is composed of quantum bits (or qubits) which have states of $|0\rangle$ and $|1\rangle$.

Quantum mechanics allows for superpositions of the $|0\rangle$ and $|1\rangle$ states with a general form of $a|0\rangle + b|1\rangle$ where a and b are complex numbers. When a qubit state is measured it collapses to either the $|0\rangle$ with probability $|a|^2$ or $|1\rangle$ with probability$|b|^2$. Taking into account the fact that $|a|^2+|b|^2=1$ (since the total probability must sum to unity) and ignoring an overall phase factor which does not have any observable effects the general state can be re-written as $\cos\frac{\theta}{2}|0\rangle + e^{i\varphi}\sin\frac{\theta}{2}|1\rangle$ and plotted on the Bloch Sphere [14] as shown in Figure 2.1. The phase difference, φ, between the$|0\rangle$ and $|1\rangle$ precesses at a rate equal to the energy separation between the $|0\rangle$ and $|1\rangle$ states divided by ħ; if this energy changes with time in an uncontrolled manner the precession rate will speed up or slow down which leads to the accumulation of phase errors.

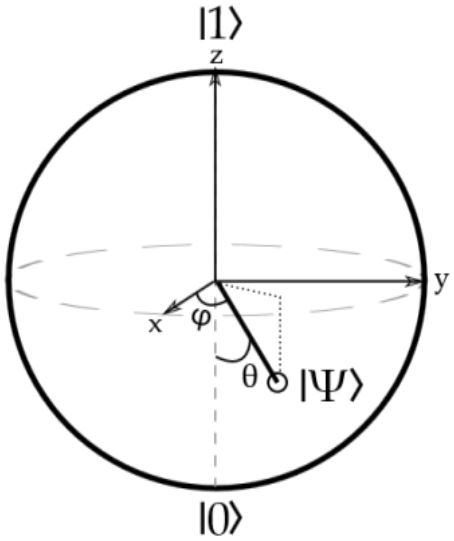

Figure 2.1: State of a single qubit can be plotted on the Bloch Sphere.

David DiVencenzo devised 5 criteria for suitable physical qubits [15]:

1. A scalable 2-state quantum system.
2. The ability to initialize all qubits to the $|0\rangle$ state.
3. Long coherence times, much longer than the gate operation time
4. "A universal" set of quantum gates.
5. The ability to read out the qubit state.

In the following section I will show how superconducting qubits meet these criteria.

2.2 Superconducting Qubits

Many quantum systems have been proposed to make physical qubits such as excitations in cold atoms or polarization of photons. Another system which qubits can be made from is superconducting electronic circuits, which this work focuses on specifically the Transmon and 3D Transmon qubit designs.

Superconducting circuits provide a quantum system due to the fact that all of the Cooper pairs share the same wave function. Superconducting circuits are also scalable since their fabrication process employs the same techniques as the fabrication of semiconductor microelectronics. Two basic elements of superconducting circuits are inductors and capacitors, however circuits made using only these 2 elements cannot satisfy DiVencenzo's criterion 1 as they will produce a harmonic oscillators with a ladder of states. In order to have an effective 2-state system a nonlinear element is needed. Note that it is not necessary to have a system with exactly 2 states if the spacing between each energy level is different, such that each level can be addressed individually. The only nonlinear, non-dissipative circuit element known is the Josephson junction, which consists of a thin insulating barrier sandwiched between 2 superconducting layers [16]. The insulating barrier is thin enough that cooper pairs can tunnel from one side to the other. Josephson Junctions act as non-linear inductors. Josephson junctions are discussed in greater detail in section 2.2.1.

Criterion 2 (initialization) can be achieved by cooling the qubits to a low temperature, such that thermal fluctuations on the order of K_bT are well below the transition energy and the qubits thermalize into the ground state. Criteria 4 (gate operation) and 5 (readout) can easily be implemented since electrical signals on wires are very efficient coupling methods [17].

I have left out criterion 3, long coherence time, which still needs to be achieved before a viable quantum computer can be made. I will discuss coherence as well as some of the causes of decoherence in section 2.3.

2.2.1 Josephson Junctions

The current and voltage of Cooper pairs through an ideal Josephson junction is given by the Josephson relations [18]:

$$I = I_c \sin\varphi$$

$$V = \frac{\hbar}{2e}\frac{\partial\varphi}{\partial t}$$

Where φ is the phase difference in the superconducting wave function across the junction, and I_c, the critical current, is the maximum current that can tunnel through the junction, which depends on the barrier thickness and the area of the junction. These two equations can be combined to give:

$$V = \frac{\hbar}{2eI_c cos\varphi}\frac{\partial I}{\partial t}$$

This looks like the equation for an inductor with inductance:

$$L = \frac{\hbar}{2eI_C cos\varphi}$$

Since inductance is a function of φ, which itself is a function of I, the inductance of the junction is non-linear in current. A non-ideal junction also has some capacitance since it is essentially formed from a parallel plate capacitor.

At a finite DC bias, quasiparticles tunnel through the barrier [19]. The current-voltage relationship governing quasiparticle tunneling is best explained using the density of states diagram as shown in Figure 2.2. The vertical axis represent energy, and the horizontal axis is density of states. Filled states are colored purple and unfilled states are green. Cooper pairs reside at the Fermi level shown as a dashed line. The pairs act as bosons and the condensate can contain virtually all of the valence electrons when the junction is not biased. Quasiparticle states exist an energy difference Δ, the superconducting energy gap, from the Fermi energy. A DC voltage bias across the junction shifts the Fermi level of one side relative to the other. In order for tunneling to occur, there must be an empty state to tunnel into at the same energy as the

filled state the electron is tunneling from. This cannot happen until there is a voltage bias of 2Δ/e. This results in an I-V curve as shown in Figure 2.3. At finite temperatures, an exponentially small number of quasiparticle states are thermally excited above the energy gap, allowing for tunneling below 2Δ/e, this results in a leakage current in the subgap region of the I-V curve. In an ideal junction, this leakage current would vanish as the temperature approaches zero.

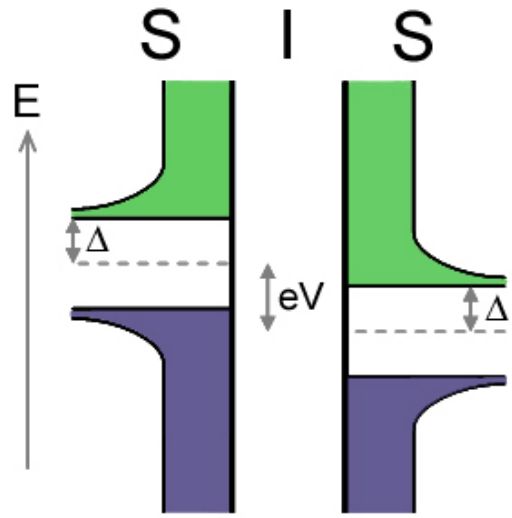

Figure 2.2: Energy diagram of quasiparticles in Josephson junction. Figure from [20].

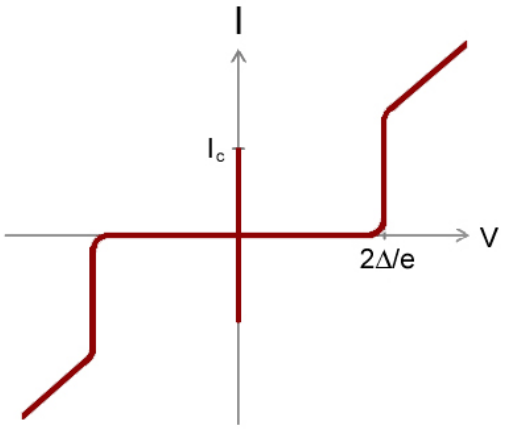

Figure 2.3: I-V characteristics for an ideal junction at zero temperature. Figure from [20]

2.2.2 Charge Qubits

In general, superconducting qubits can be grouped into 3 distinct types based on their relevant degree of freedom: charge [21] [9], phase [22] and flux [23]. The transmon is based on the charge qubit [24], so I will begin by explaining the charge qubit, also known as the Cooper pair box. It consists of a small superconducting island with a Josephson junction connected to it. The island is biased with a gate capacitor. The right side of Figure 2.4 shows a schematic of such a device. This circuit has a relatively simple Hamiltonian given by:

$$\widehat{H} = 4E_c\left(\hat{n} - n_g\right)^2 - E_j \cos\hat{\varphi}$$

The first term is the charging energy of the capacitor. $4E_c$ is the energy of a single Cooper pair on the capacitor, E_C is given by:

$$E_c = \frac{e^2}{2C_{total}}$$

The total capacitance:

$$C_{total}=C_g+C_j$$

is the sum of the gate capacitance C_g and the junction capacitance C_j, $\hat{n}$ is the operator for the number of cooper pairs on the island, n_g is the offset charge controlled by the gate electrode:

$$n_g=C_gV_g/2e$$

The second term is the energy of the Josephson junction. E_j is the Josephson energy given by:

$$E_j = \frac{\hbar I_c}{2e}$$

$\hat{\varphi}$ is the operator for the phase across the junction. The Eigen state can be explicitly solved In the phase basis [25], where

$$\hat{n} = \frac{1}{i}\frac{\partial}{\partial\varphi}$$

$$\hat{\varphi} = \varphi$$

The Eigen states are Mathieu's functions, and the energy levels are given by

$$E_k = \frac{E_c}{4}\mathcal{M}_A\left(k+1-(k+1)[mod\ 2]+2n_g(-1)^k, -\frac{2E_j}{E_c}\right)$$

Where $\mathcal{M}_A$ are the Mathieu characteristic values, and k is the energy level (0,1,2,etc).

The charge qubit is typically operated in the regime of low Ej/Ec and has energy levels as shown in the right side of Figure 2.4. The black line represents $E_0(n_g)$, the red line is $E_1(n_g)$ and the blue line is $E_2(n_g)$. Note that there is a large change in the energy difference between the first 2 levels with a small change in n_g; this makes the charge qubit very sensitive to noise in the gate bias. The charge qubit is typically operated at n_g=1/2, where there is only second order dependence of the energy spacing on n_g. There will be noise in n_g, even if the voltage source is perfect, due to electrons hopping into and out of charge traps in the dielectric of the gate capacitor.

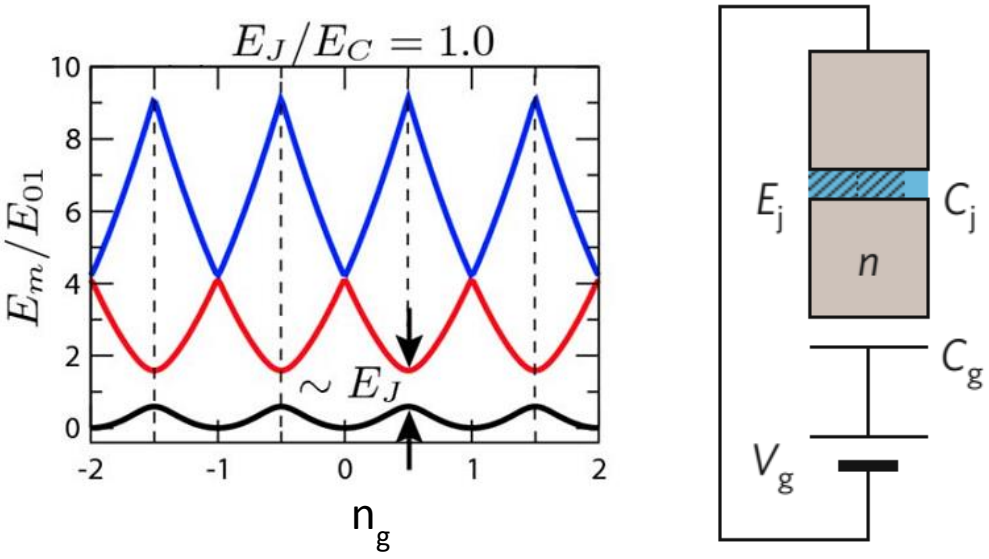

Figure 2.4: Left: Eigen energies E_m of the first 3 levels of the charge qubit Hamiltonian as a function of n_g. Image from [24] Right: Schematic of a charge qubit. Image from [26].

2.2.3 Transmon Qubits

The transmon qubit consists of junction shunted by an interdigitated capacitor and coupled to a coplanar waveguide resonator with a gate capacitor. A schematic is shown in Figure 2.5. The transmon has the same Hamiltonian as the charge qubit, where here $\hat{n}$ is now the

difference in the number of Cooper pairs across the junction. The resonator allows for the readout of the qubit. The qubit causes a dispersive shift in the resonant frequency of the resonator which is dependent on the state of the qubit. By detecting the differerence is the cavity frequency, one can tell the state of the qubit, this is discussed in more detail in secion 5.2.1. In addition, with the resonant frequency detuned from the qubit frequency, spontaneous emission from the qubit is suppressed due to the purcell effect [27].

The energy levels of charge type qubits vary with the ration of E_j to E_C; as E_j/E_C increases, the energy levels flatten out. The transmon has a large E_j/E_c ratio giving it energy levels as shown in Figure 2.6 (d). The energy spacing is now very flat with changes in n_g, removing its susceptibility to charge noise, and eliminating the need to give it a DC gate bias. The shunt capacitor has a vacuum gap (mostly, there is a thin native oxide on the surface of the shunt capacitor, which has contribution to loss), so it should have less resistive loss than the junction capacitance, which has an AlO_x dielectric. Since the capacitance is the sum of the junction capacitor and the shunt capacitor and increasing E_c Is accomplished by increasing the shunt capacitance, the participation ratio of the junction capacitance (C_j/C_{total}) is reduced, and thus loss from the junction capacitor should be reduced. In the asymptotic limit of high E_j/E_c the energy spacing between the first 2 energy levels becomes:

$$E_{01} = \sqrt{8E_cE_J}$$

It is easy to see how this happens. In particular, this energy can be calculated by considering the transmon as an LC oscillator. The resonant frequency of an LC circuit is:

$$\omega = \frac{1}{\sqrt{LC}}$$

As mentioned earlier the inductance for a junction is:

$$L = \frac{\hbar}{2eI_C cos\varphi}$$

Since we are considering the lowest transition, we can treat φ as small so that cosφ is approximately 1. From this we get:

$$L = \frac{\hbar}{2eI_c} = \left(\frac{\hbar}{2e}\right)^2 \frac{1}{E_J}$$

We can rearrange the formula for E_C to get:

$$C = \frac{e^2}{2E_C}$$

Substituting these into the formula for energy we get:

$$E_{01} = \hbar\omega = \frac{\hbar}{\sqrt{\frac{\hbar^2}{4e^2E_j}\frac{e^2}{2E_C}}} = \frac{\hbar}{\sqrt{\frac{\hbar^2}{8E_CE_J}}} = \sqrt{8E_CE_J}$$

Which is what we were solving for.

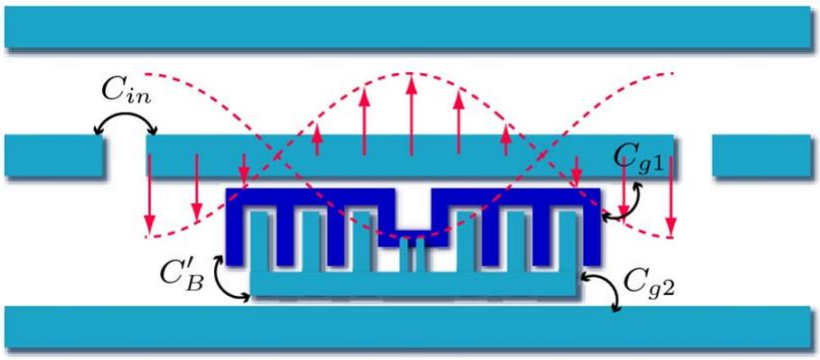

Figure 2.5: Schematic of a transmon qubit. Image from [24].

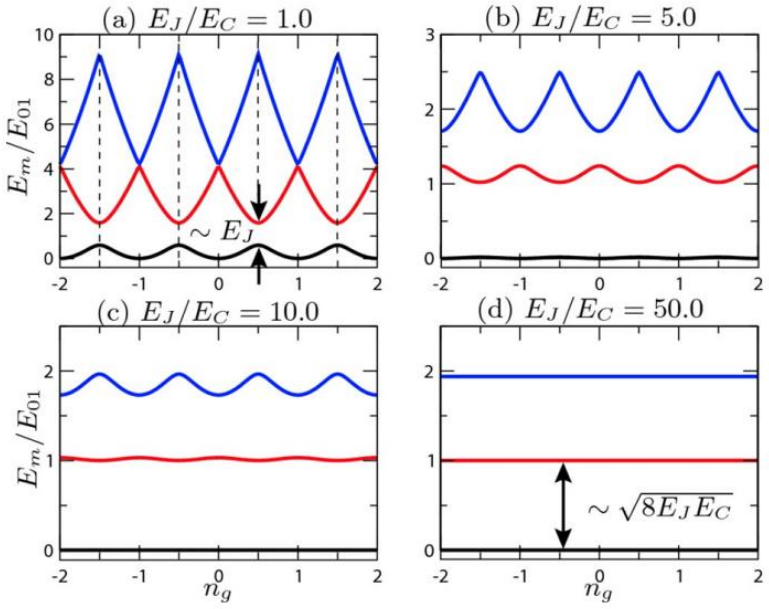

Figure 2.6: Energy level spacing of charge (or transmon) vary with EJ/EC. The transmon uses high EJ/EC as shown in (d). Figure from [24].

A further refinement of the transmon qubit is the 3D transmon [28]. The 3D transmon consists of a single Josephson junction between 2 large superconducting electrodes as shown in Figure 2.7. The capacitance between the electrodes forms the shunting capacitor, and the pair of electrodes together form a dipole antenna which capacitively couples to the cavity, which acts as a resonator. This greatly simplifies the fabrication process by eliminating the need for an on chip resonator. The large capacitor paddles also reduces the sensitivity to surface dielectric losses.

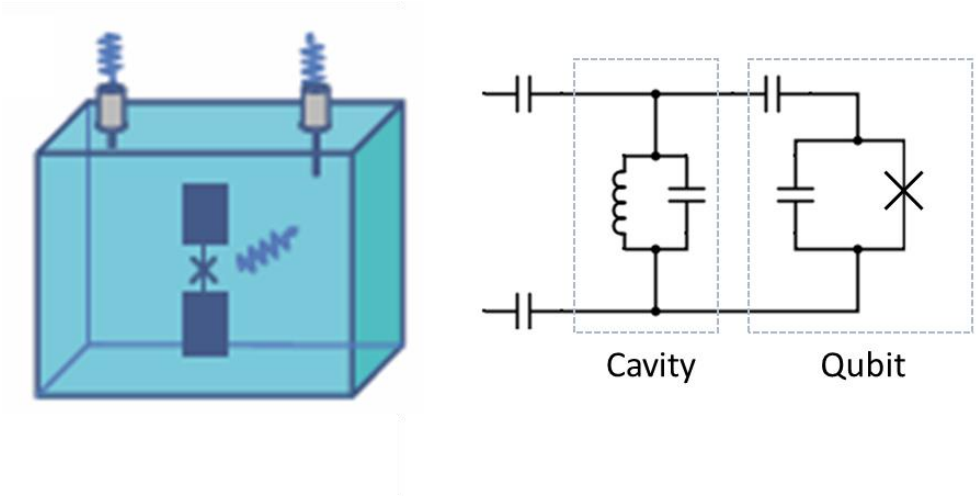

Figure 2.7: Left: Schematic of 3D transmon qubit in cavity. Image from [28]. Right: Effective circuit diagram for 3D Transmon.

2.3 Coherence

Qubits are quantum mechanical objects. As such they can exhibit quantum behavior such as being in superposition states, exhibiting interference and being entangled with one another. The timescale over which they exhibit this quantum mechanical behavior is referred to as the "coherence time" [29].

2.3.1 Relaxation and Dephasing

Rather than a single coherence time, decoherence can be characterized by two times T_1 and T_2. T_1 is the relaxation time which is the time required for the qubit to relax from the first excited state to the ground state. This corresponds to changes in θ on the Bloch sphere. This involves the loss of energy from the qubit.

T_2 is the dephasing time, which is the time it takes for the phase of the qubit to be randomized. It corresponds to integrated changes in φ, on the Bloch sphere. Dephasing is caused by changes in the qubit transition frequency, which changes the precession rate and causes phase errors to build up. T_2 depends on both the relaxation time and the pure dephasing time, T_ϕ as follows:

$$\frac{1}{T_2} = \frac{1}{2T_1} + \frac{1}{T_\phi}$$

The pure dephasing time is the time it would take the qubit phase to be randomized in the absence of added dephasing due to relaxation (i.e. if T_1 were infinite.)

2.3.2 Measurement of Coherence Times

In order to understand coherence times it is useful to know how they are measured. The first type of measurement I will discuss is Rabi oscillations [30]. Rabi oscillations are not a measure of coherence time, but they are an important calibration for performing these measurements. To measure Rabi oscillations a variable length microwave pulse at the qubit frequency is sent in to the cavity. This pulse has the effect of rotating the qubit state around the x-axis of the Bloch sphere. This is illustrated in Figure 2.8. Immediately after this pulse the state of the qubit is measured, returning either a zero or a 1 state. This process is repeated many times, in order to perform an ensemble measurement, and the probability of being in the excited state as a function of pulse length is plotted; It shows a sinusoidal pattern which decays over time due to decoherence. Figure 2.9 shows an example of this. Rabi oscillations are used to find π pulses and π/2 pulses which are used in the experiments to measure T_1 and T_2. A π pulse is the pulse length required to excite the qubit from the ground state to the excited state; it is called a π pulse because this is a rotation of the qubit state of π radians around the x-axis of the Bloch sphere. Likewise a π/2 pulse is the pulse length required to excite the qubit state to point along the y-axis of the Bloch sphere which is the state $\frac{1}{\sqrt{2}}|0\rangle + \frac{1}{\sqrt{2}}|1\rangle$.

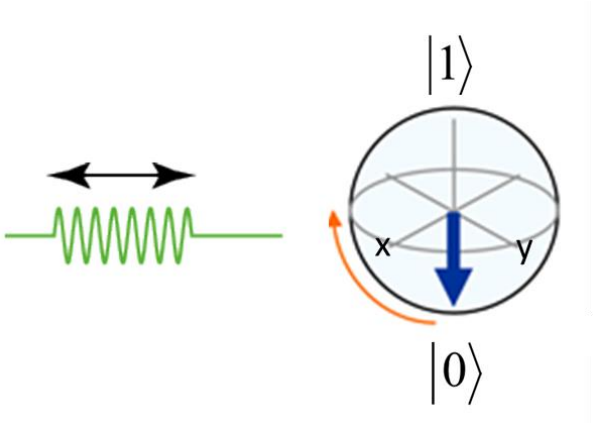

Figure 2.8: In a Rabi experiment, the probability of the qubit being in the excited state is measured as a function of pulse length. Image from [31].

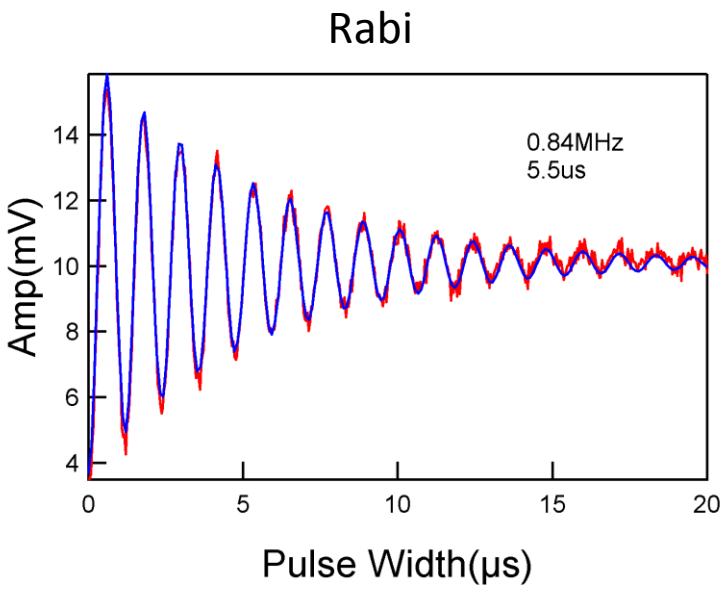

Figure 2.9: Example of Rabi oscillations.

To measure T_1, the relaxation time of the qubit , a π pulse used to put the qubit into the excited tate. Afterwards there is a variable delay time, and the state of the qubit is measured, as illustrated in Figure 2.10. This process is repeated many times to give an ensemble measurement comptue the probability that the qubit remains in the excited state as a function of delay time. An exponential is fitted to this and the decay time is T_1. Figure 2.11 shows an example of such a measurement performed twice on the same qubit resulting in relaxiation times of 20.9 and 22.9 microseconds.

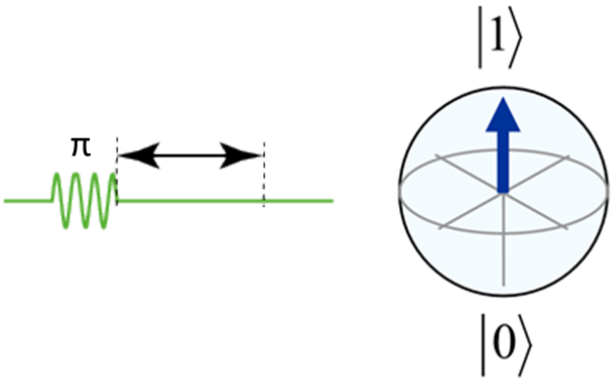

Figure 2.10: Measurement of relaxation time. Qubit is put in excited state and probability that it is still there as a function of time is measured. Image from [31].

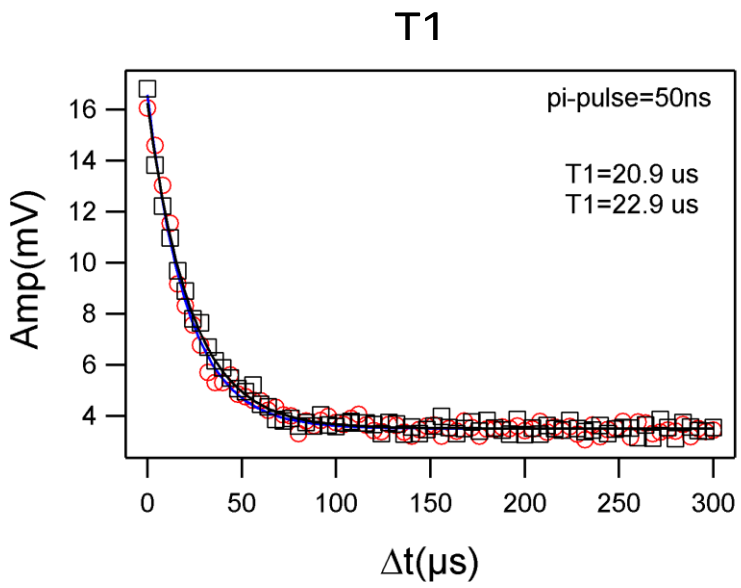

Figure 2.11: An example of a measurement of T_1.

The intrinsic dephasing time T_2, is distinguished from the result of an ensemble measurement which is T_2*. These are different because ensemble measurements average large numbers of runs and are susceptible to low freqency fluctuations in the qubit frequency which are stable over the timescale of a single run, but vary from run to run, which reduces the measured dephasing time to T_2*.

T2* can be measured using Ramsey fringes [32]. A $\pi/2$ pulse is used to excite the qubit to the y-axis of the Bloch sphere. Then there is a variable delay time during which the qubit state precesses around the equator of the Bloch sphere at the qubit frequency, and then a second $\pi/2$ pulse moves the qubit state to a position on the Bloch sphere dependent on its overall phase. If it has precessed half way around the Bloch sphere (a phase of π), the second $\pi/2$ pulse would return the qubit to the ground state. Likewise, if it has precessed all the way around the Bloch sphere (a phase of 2π) the second $\pi/2$ pulse would move it to the excited state. In the absense of any dephasing, the probabilty of being in the excited state should be a sinusoid as a function of delay between the two pulses. However, if the phase randomized, it has an equal probability or returning to the ground state as it does of entering the excited state. This causes the sinusiod to decay, with T_2* being the decay rate. Figure 2.12 illustrates this process. Figure 2.13 shows an example of Ramsey fringes.

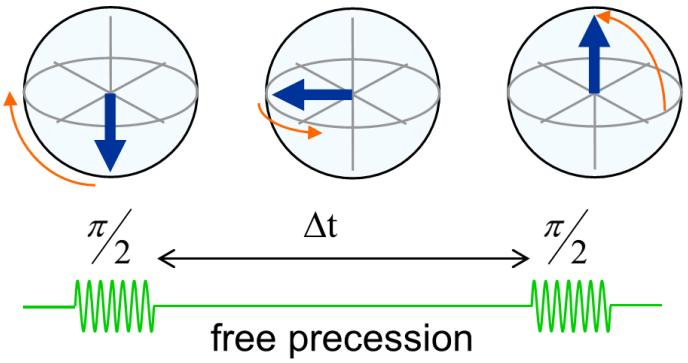

Figure 2.12: In a Ramsey experiment, the qubit is put in a superposition state, then it is allowed to precess around the Bloch sphere, finally it is given a π/2 pulse, which depending on the phase of the precession, puts it in either the excited or ground state (or somewhere in between). Image from [31].

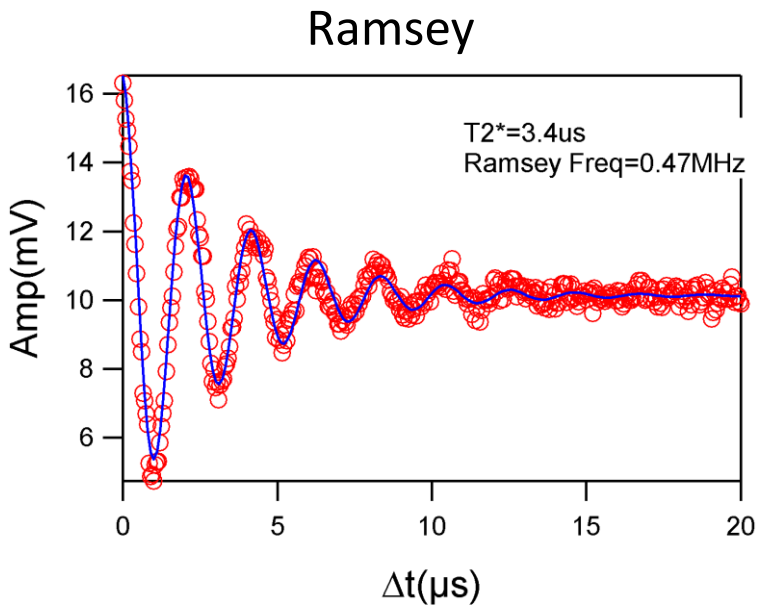

Figure 2.13: Example of Ramsey fringes

The effect of low frequency fluctuations can be corrected for using the spin echo technique, allowing for a measurement of T_2. This is a refinement of the Ramsey technique in which a π pulse is inserted midway between the π/2 pulses. This makes it such that if the phase was leading before the π pulse it is now lagging, and vice versa. This has the effect that if it is processing at a constant rate throughout the run it ends up at the negative y-axis, regardless of what that rate was, and so the second π/2 pulse returns it to the ground state. In this way the effect of fluctuations in the qubit frequency between runs are filtered out leaving only the effect of

fluctuations within a single run. However, if the rate of precession was not constant, the final position on the equator of the Bloch sphere is not the negative –y axis, and so it does not return to the ground state. This procedure is shown in Figure 2.14.

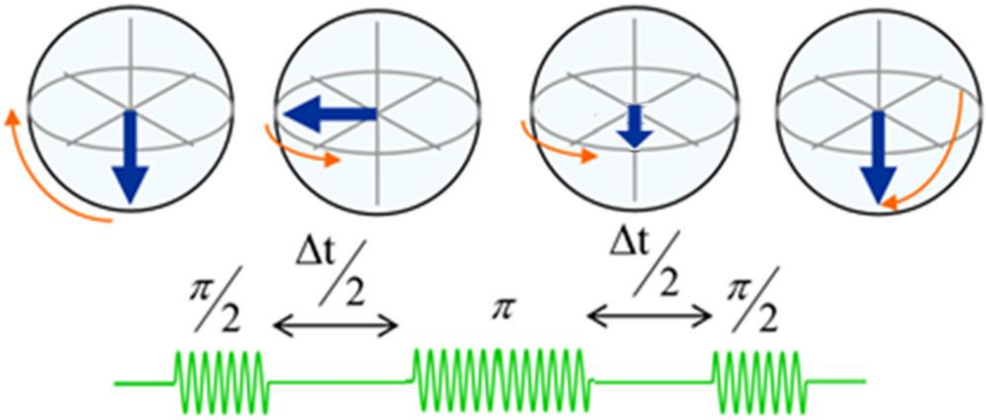

Figure 2.14: A spin echo measurement is performed by using a π/2 pulse to put the qubit in the superposition state, then it is allowed to precess, then a π pulse flips it around the x axis and it continues to precess, and a second π/2 pulse returns it to the x axis. Image from [31]

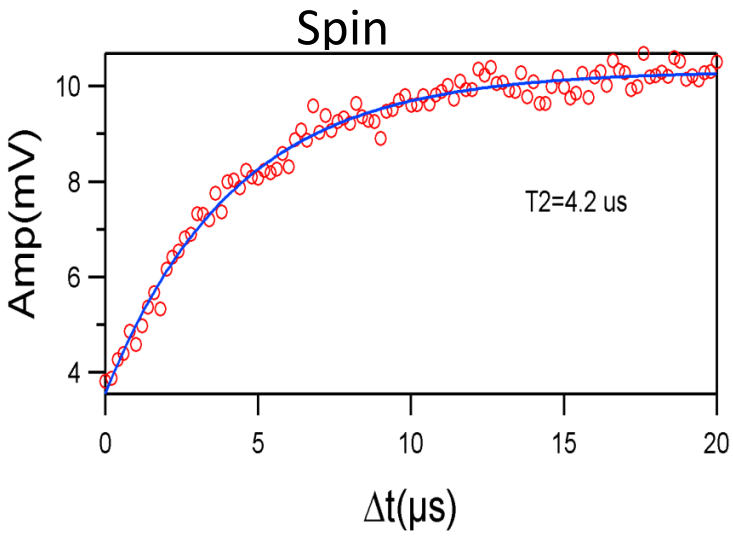

Figure 2.15: Example of spin echo measurement.

2.3.3 Recent improvements in coherence

In recent years great strides have been made in in the improvement of the coherence times of superconducting qubits [8]. This is illustrated in Figure 2.16. The first demonstrated superconducting qubit (a charge qubit) in 1999 showed a coherence on the order of 1 nanosecond [9]. In 2002 the quantronium qubit was developed which had a coherence time on the order of hundreds of nanoseconds [33]. In 2007 the Shoelkopf group developed the transmon qubit with a coherence time on the order of a few microseconds [34], in 2011 they developed the 3d transmon with a coherence time on the order of 20 microseconds [28]. These advances were all the result attempting to minimize the qubit's sensitivity to specific sources of noise though design modifications. There is another approach that has also been important to the rapid rise in the coherence time of qubits shown in Figure 2.16. That is the study of the materials sources of the noise, and the improvement of the materials and fabrication process to reduce this noise. My work follows this second approach.

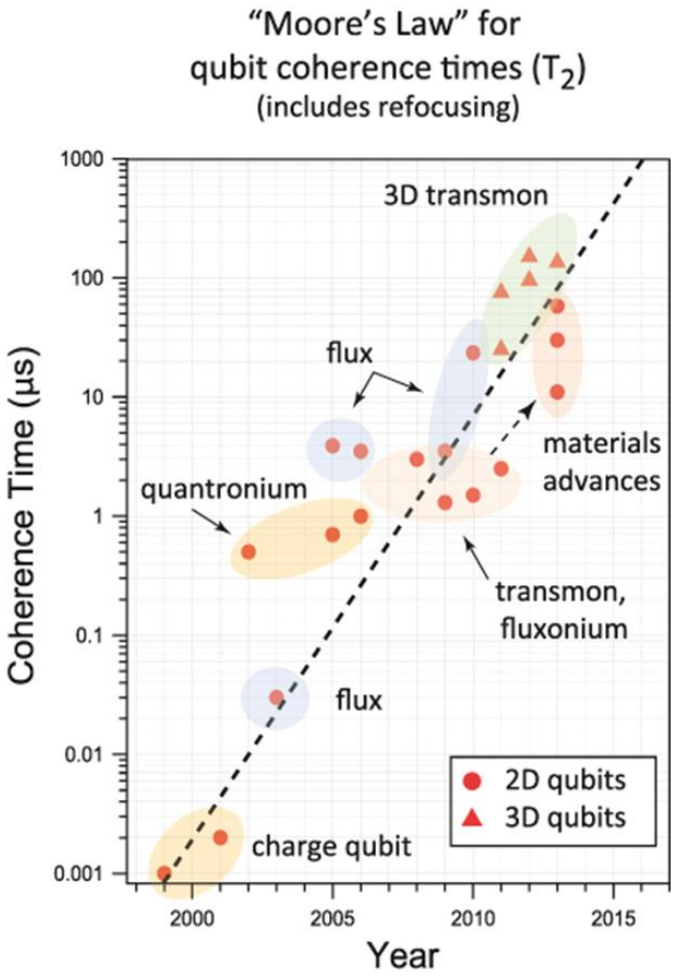

Figure 2.16: There have been rapid increases in coherence times achieved in superconducting qubits. Image from [29].

2.3.4 Materials sources of decoherence

The dominant source of decoherence is thought to be two level systems in non-crystalline dielectric materials. These TLS's are thought to be either an electron on an ion that can tunnel between two spatial states, which are caused either by defects in the crystal structure or through polar impurities such as OH^- [29]. Two level systems were first seen in phase qubits in 2004 [35] and in flux qubits shortly thereafter [36].

One source of these TLS's is in the barrier of the tunnel junction. Josephson junctions are typically formed by diffusive oxidation of aluminum to form AlO_x, which is known to have a measurable density of TLS's [37]. One way TLS's in the barrier can lead top dephasing is though critical current noise. All types of superconducting qubits are susceptible to dephasing from

critical current fluctuations [26]. Critical current noise in Josephson junctions is observed to have a 1/f spectrum [38] [39] [40]. This spectrum is caused by the ensemble average of telegraph noise from a large number of charge traps in the barrier [40]. Charges hop into and out of these traps and prevent tunneling of cooper pairs in a region ΔA around the trap due to coulomb repulsion, which reduces the critical current by $\Delta I_0 = I_0(\Delta A/A)$ as illustrated in Figure 2.17. This is not thought to be a dominant source of decoherence at the moment but could become important in the future once other noise sources are reduced.

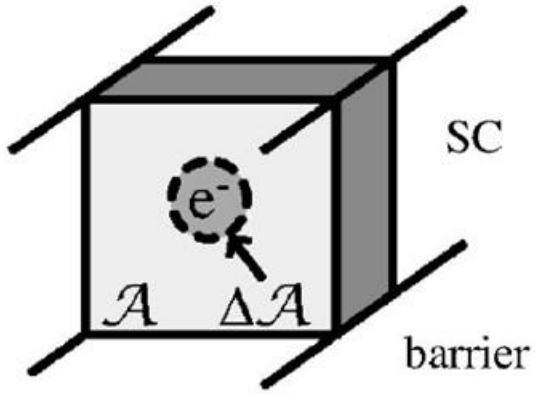

Figure 2.17: A charge trap blocks tunneling in a region ΔA, reducing the critical current. Image from [19]

There is another way that TLS's can lead to decoherence in the qubit. If the TLS's are in resonance with the qubit, they can couple to it. The TLS can exchange energy coherently with the qubit. The TLS couples to the strain field and it can decay from its excited state by emitting a phonon, which loses the energy to the environment [41].

Very little work has been done to reduce the density of TLS's in Josephson junction barriers. Oh et al. have shown that epitaxial barriers have a reduced density of TLS's [42]. Paul Welander (a former member of the Eckstein research group) grew amorphous barriers by co-depositing aluminum in an oxygen environment [43]. He showed that Josephson junctions grown this way had ideal transport in the subgap region, while junctions formed by diffusive oxidation had excess leakage as shown in Figure 2.18. This could be an indication of reduced TLS's in a co-deposited barrier.

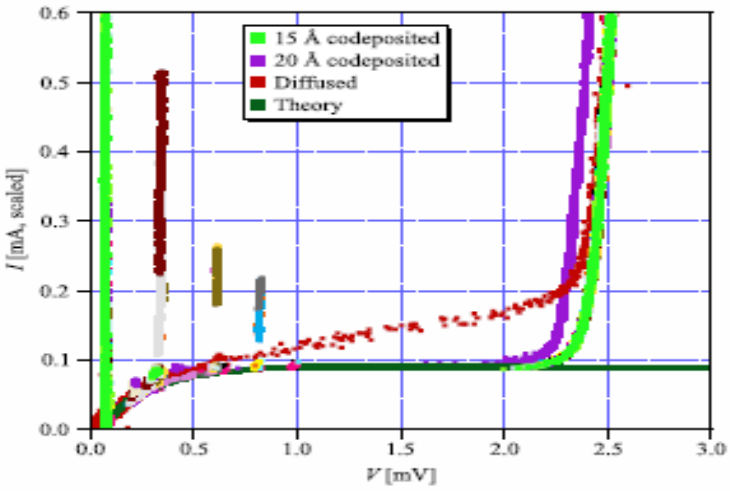

Figure 2.18: Co-deposited barriers show ideal subgap transport, while diffused barriers have increased leakage current. Image from [43].

TLS's can also exist either on the surface of the superconductor or at the substrate interface [44]. Megrant et al. improved the quality factors (Q) of MBE grown aluminum resonators, by careful substrate preparation prior to growth, to remove any contamination between the substrate and the aluminum [45]. They found that by outgassing their substrates at 850 °C in the presence of activated oxygen, they were able to improve the epitaxy of their aluminum films and achieve a quality factor of over one million. Chang et al. have improved the coherence time of qubits by eliminating loss in surface oxides by using titanium nitride electrodes, which are stable against oxidation [46].

Another source of decoherence is quasiparticles tunneling through the junction [47] [48]. Quasiparticles can be generated in a few ways. The first is through non-equilibrium quasiparticles which have been excited through stray radiaton or have diffused from a higher temperature region of the sample. The other is through breaking Cooper pairs which can occur at qubit energies if there exits quasiparticle density of states in the gap, which has been seen experimentaly and is perhaps caused by broadening of the gap edge by impurities [49].

2.3.5 Proposed Solution to decoherence

My approach is to use MBE, to grow junctions with single crystal base electrodes. I carefully prepare my substrates using a procedure inspired by [45] in order to prevent any TLS's at the substrate-superconductor interface.

Starting with state of the art transmon qubits, I study the effect on the coherence time of 3D transmon qubits due to growing high quality in situ dielectrics on the surface of the qubit structures in order to try to decrease the density of TLS's from that of the native oxide. First I study the effect forming a diffusive oxide in situ with UHP oxygen compared to the native oxide formed in air. Next I grow a co-deposited oxide similar to that done in [43]. Finally I grow aluminum nitride on the surface of the transmons which is stable against oxidation.

Chapter 3 Niobium Trilayer Qubits

In this chapter I will discuss the growth in Niobium/Aluminum oxide/Niobium trilayers by MBE, and their subsequent processing into Josephson Junctions. Initially, niobium seemed like an ideal material to fabricate into qubits, due to its relatively high T_C. The use of MBE to grow the films results in junctions with all interfaces made in situ, which should have a reduced density of defects. I will begin by first describing the MBE system. Then I will describe the process for growing the films. A single crystal niobium base layer is grown. Then a thin single crystal aluminum layer is grown on the niobium. An aluminum oxide barrier is grown by the co-deposition of oxygen and aluminum. A polycrystalline niobium counter electrode is grown on top. I will then discuss the process for fabricating this trilayer film into junctions. This process is self-aligned and is capable of fabricating junctions on the order of 1 square micron. I will discuss the results we had for this process, including some of the problems with it. Ultimately I will conclude that niobium is not a good material for qubits, due to the existence of quasiparticles in the energy gap, which lead to loss and decoherence.

3.1 MBE System

Molecular beam epitaxy (MBE) is a technique that grows epitaxial films from beams of evaporated source material interacting with a crystalline substrate forming one layer at a time, under ultrahigh vacuum (UHV). Due to the UHV conditions the mean free path is very large resulting in atoms with essentially a straight line path from source to the substrate. Sources are usually in the form of effusion cells, also known as Knudsen cells, which consist of a frame that holds a crucible open at one end, a heater filament and a thermocouple to measure and control the temperature. Effusion cells can reach temperatures up to 1500 °C. These sources are equipped with shutters which can quickly cover and uncover individual sources allowing for rapidly changing the beam species.

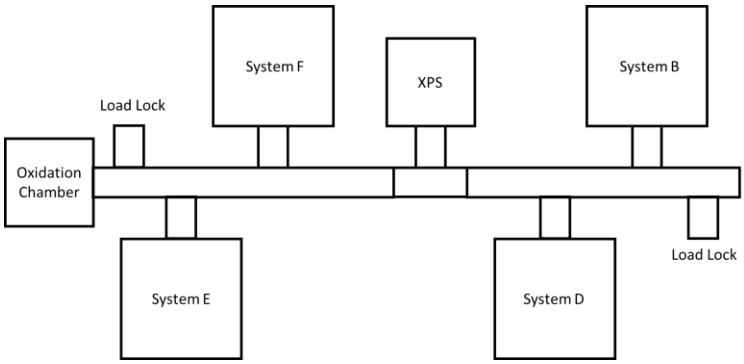

Figure 3.1: Layout of MBE system

Film growths for the work were done in one of two MBE chambers, which are part of a larger MBE system consisting of four MBE chambers connected with a high vacuum transfer tube. The layout of this facility is shown in Figure 3.1. Also connected to the transfer tube is an X-ray photoelectron spectroscopy (XPS) system and an oxidation chamber. Each chamber is configured for the growth of a different material type. The films studied in this work were grown in Systems E and F, which are configured for the growth of metals as well as metal-oxides (System E) and metal nitrides (System F). A schematic of these systems is shown is Figure 3.1

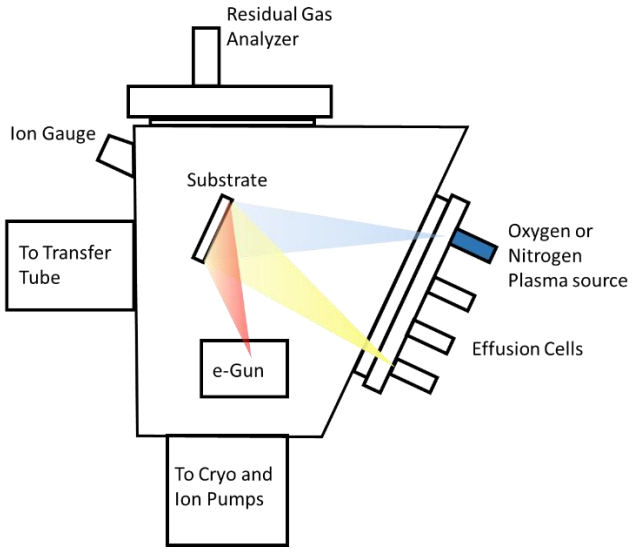

Figure 3.2: Schematic of systems E and F

These chambers are pumped by cryo pumps, ion pumps and titanium sublimation pumps,

which when combined with internal liquid nitrogen cryo shrouding result in a pressure of about 10^{-11} Torr, which is measured by ion gauges in the chamber. These chambers each have a source flange that can hold up to eight effusion cells all pointed at a common position where the substrate is held. The sources are mounted at 24° with respect to the normal of the substrate; this angle is important to the creation of shadowmask junctions discussed in Chapter 4. Currently, system E has effusion cells loaded with aluminum, gold, and titanium while system F has aluminum and titanium.

Each chamber has one port taken up on the source flange with a quartz crystal monitor (QCM) to measure the deposition thickness. A QCM uses a quartz crystal oscillating at its resonant frequency. As mass is deposited on the crystal the resonant frequency changes, and by constantly measuring the resonant frequency the deposited mass can be calculated. In order to accurately measure deposition rate, three parameters are necessary: density, Z-ratio, and tooling factor. Density is used to convert from deposited mass, to deposited thickness. Z-ratio is the ratio of the acoustic impedance of the deposited material to that of quartz, and it is used to correct for changes to frequency due to acoustic impedance mismatch between quartz and the deposited material. Tooling factor compensates for the fact that the QCM is located at a different position than the substrate, and thus receives a different flux. The angular distribution of flux should be independent of total deposition rate, and the tooling factor is the ratio of the deposition rate at the location of the substrate to that at the QCM. Density and Z ratio are materials properties that can be looked up for commonly deposited materials, but tooling factor depends on the position of the QCM relative to the source and the type of source used, and it must be calibrated for each source. To calibrate the tooling factor, it is first set to 1 on the QCM controller. Then about 1000 Å of material is deposited on the substrate according to the QCM. The actual thickness of the deposited material is measured (say by etching a portion of the film down to the substrate, and using AFM to measure the step edge). The tooling factor is then calculated by (measured thickness)/(thickness reported by QCM). This must be done for each source, since each one is in a different position relative to the QCM.

For materials requiring higher evaporation temperatures than an effusion cell can provide, electron beam evaporation is used. Electrons are accelerated at 10 kV, and steered by

the use of electromagnets into the source material, which sits in a water cooled copper hearth. Upon colliding with the source material the electron imparts its kinetic energy to the source material heating it up, causing it to evaporate and deposit on the substrate. Our system uses a Thermionics HC series, linear four pocket e-gun, which currently has 3 of the pockets filled with niobium and the fourth filled with rhenium. For niobium, to deposit 0.3 Å/s (a typical growth rate), requires a temperature of about 2400 °C, which requires an emission current of about 200 mA.

System E is equipped with an oxygen gas injector for the growth of oxides. A bottle containing UHP oxygen is connected to a manifold, though a needle valve which restricts the oxygen flow from the bottle; the pressure in the manifold is reduced by a roots pump. A roots pump is a displacement pump that consists of two counter-rotating lobed rotors, which trap gas at the inlet and compress it as it is moved to the exhaust. Since these pumps contain no oil, there is no risk of contamination to the oxygen line from back streaming. From this manifold an on/off valve and a needle valve connect to the chamber. The needle valve allows the control of the oxygen pressure in the chamber in the range from 10^{-9} to 10^{-5} Torr. Inside the chamber a large aspect ratio tube directs the gas flow at the substrate. I estimate the oxygen flux at the surface of the substrate to be approximately $4x10^{15}$ oxygen molecules per square centimeter when the chamber pressure is at $5x10^{-6}$ Torr.

System F is equipped with a nitrogen plasma source for the growth of nitrides (SiN, TiN, AlN). This source is connected to a bottle of UHP nitrogen gas through a precision leak valve, which is capable of controlling the nitrogen pressure in the chamber in the range from 10^{-9} to 10^{-5} Torr. The plasma supply is powered by an RF power supply, with a manual RF matching unit, capable of supplying up to 500 W. It supplies a flux of reactive nitrogen, for example it allows the growth of TiN at a pressure of 10^{-6} Torr and a temperature of 1100 K

The substrate is mounted on a rotatable stage, which is equipped with a heater that can heat the substrate up to 1200° C. System F is equipped with a thermocouple to measure the temperature of the substrate, whereas system E is not. This thermocouple makes poor contact with the substrate and thus is somewhat unreliable, so a pyrometer is usually used to measure

the temperature of substrates. Pyrometers work by measuring the thermal emission in some band (usually the infrared). To determine the temperature accurately, the emissivity of the object being measured must be known. Emissivity depends on the material, the surface finish, and the temperature of the material. Because the substrates are transparent to infrared, the backside of the substrate must be coated with metal (usually titanium). This serves two purposes, first it absorbs the infrared emitted by the heater, allowing the substrate to be heated radiatively, and second it allows the pyrometer to measure the temperature of the substrate. Due to difficulties with determining the true emissivity, as well as errors due to the absorption of IR by the windows of the chamber, the pyrometer reading is not a very accurate reading, however it is reproducible, and can be used to compare one film grown in the same chamber under similar conditions to another.

The chambers are also equipped with quadrupole mass spectrometer residual gas analyzers (RGAs) to detect the components of the residual gas in the chamber. After the chamber is vented, the RGA shows a considerable amount of water, which goes away after the chamber has been baked for about 10 days. The bake is performed by placing heaters around the chamber, and covering both the chamber and the heaters with insulating fiber glass blankets. Thermocouples are placed at various positions around the camber to monitor the temperature of the bake. The temperature should be above 100 °C to evaporate the adsorbed water, but below 200 °C to prevent damage to the equipment. Figure 3.3 shows RGA scans of system E after being vented before being baked (top) and after being baked (bottom). Before the system was baked the pressure was $6x10^{-9}$ Torr, and the RGA scan had a large amount of water as well as other gasses. After the bake, the pressure had reduced to $1.5x10^{-10}$ Torr (with the cryo panels warm) i.e. the pressure decreased by a factor of 40. The RGA scan shows that water and other gasses are greatly reduced. There is residual hydrogen, carbon monoxide and carbon dioxide in the chamber after the bake, which outgas from the stainless steel and cannot be eliminated.

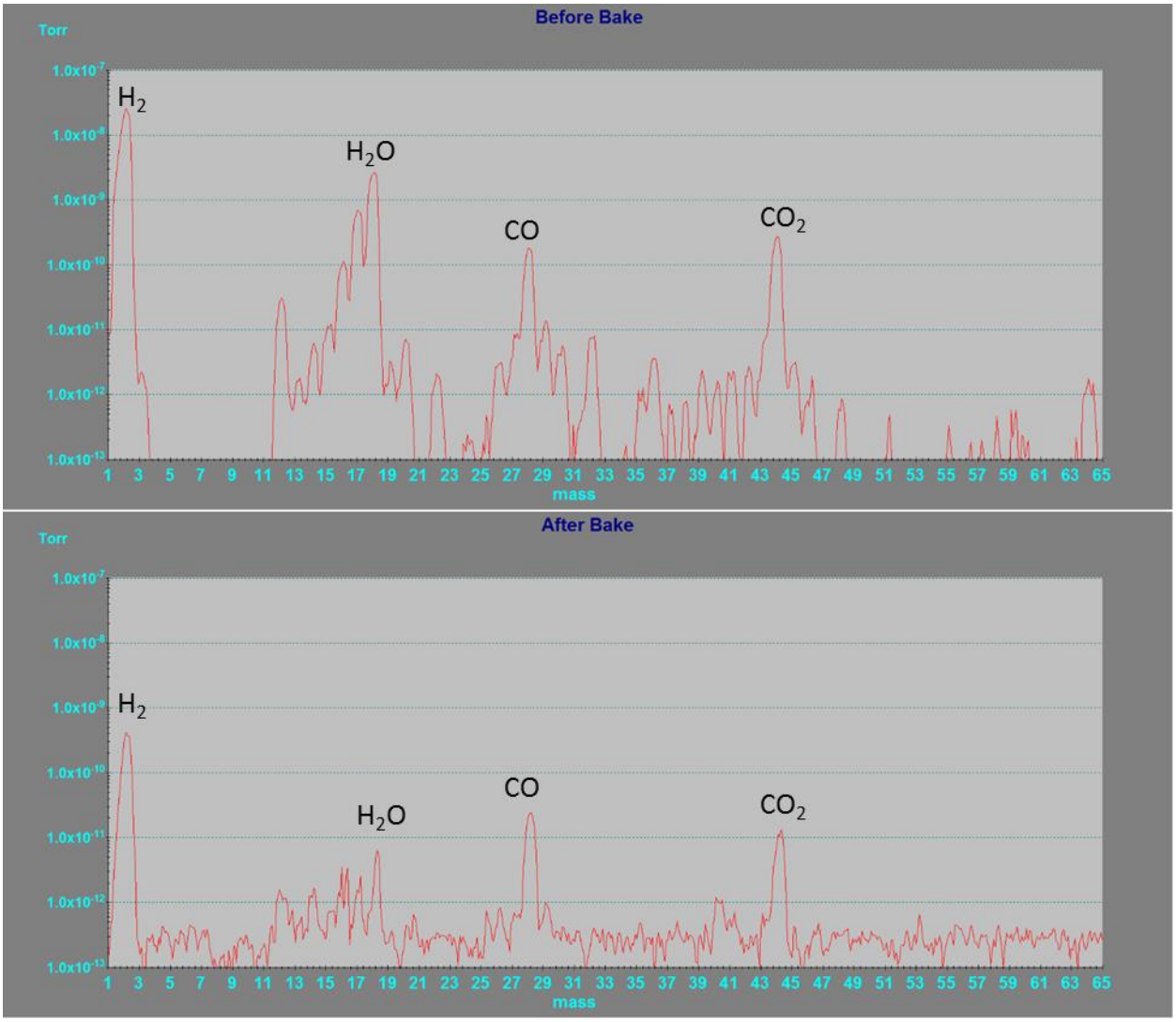

Figure 3.3: RGA scans of chamber after a vent, both before the bake (top) when the pressure was $6x10^{-9}$ Torr and after the bake (bottom) when the pressure was $1.5x10^{-10}$. All of the gas is reduced, water (18) expecially. Residual gasses left after bake are hydrogen (2) carbon monoxide (28) and carbon dioxide (44) which outgas from stainless steel.

The RGA is also useful for detecting leaks by the presence of nitrogen, oxygen, and water in the ratio of that of air. It is also useful for locating leaks by monitoring the helium level in the chamber while spraying helium gas at one of the flanges at a time, until the helium level spikes, indicating that that flange is leaking.

An in-situ reflection high energy electron diffraction (RHEED) system is incorporated into each chamber to monitor the growths. In RHEED an electron gun emits high energy electrons (10 kV in our system) which strike the surface of the film at a glancing angle (about 1°). The electrons diffract off the periodic crystal lattice, creating a pattern on a phosphor screen. The

glancing angle causes the electrons to only interact with the first top monolayer of the crystal. For diffraction at a grazing angle the Laue condition is $\vec{k}_{\parallel,outgoing} = \vec{k}_{\parallel,incoming} + \vec{q}$. Where $\vec{q}$ is the reciprocal space vector of the crystal's lattice, and ∥ indicates the components parallel to the sample surface. Because the scattering is restricted to two dimensions, the reciprocal space points of the lattice are extended along the surface normal becoming rods; the RHEED pattern is formed by the intersection of these rods with the Ewald sphere, a sphere of radius k, the momentum of the incident electron beam.

3.2 Growth

In this section I will discuss the growth of niobium/aluminum-aluminum oxide/niobium trilayers that will be processed into Josephson junctions. The structure of these trilayer films is shown in Figure 3.4. First single crystal niobium is grown on c-plane sapphire at a temperature of about 700 °C. Next a thin single crystal aluminum layer is grown on top of the niobium base layer at room temperature. Then an amorphous aluminum oxide barrier is grown on the aluminum at room temperature. Finally a polycrystalline niobium counter electrode layer is grown at room temperature. Most of the growth procedure presented in this section was developed by Dr. Paul Welander, a former member of the group [50].

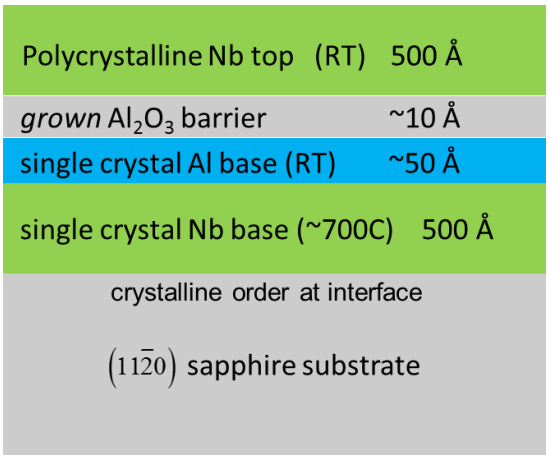

Figure 3.4: Structure of trilayer films

3.2.1 Substrate Preparation

The natural choice of substrate for this work is sapphire (α-Al2O3), because it is a low loss material suitable for obtaining long coherence times. It is also a good choice of substrate due to

the special three dimensional relationship that sapphire has with single crystal niobium, which was first discovered by Durbin et al [51]. By choosing the orientation of the sapphire substrate the orientation that the niobium grows in can be selected. The reason for this was discovered by Gutekunst et al [52]. The surface of the sapphire is oxygen terminated, and the niobium atoms in the first monolayer fill in the lattice positions that the aluminum would have, had the sapphire lattice continued.

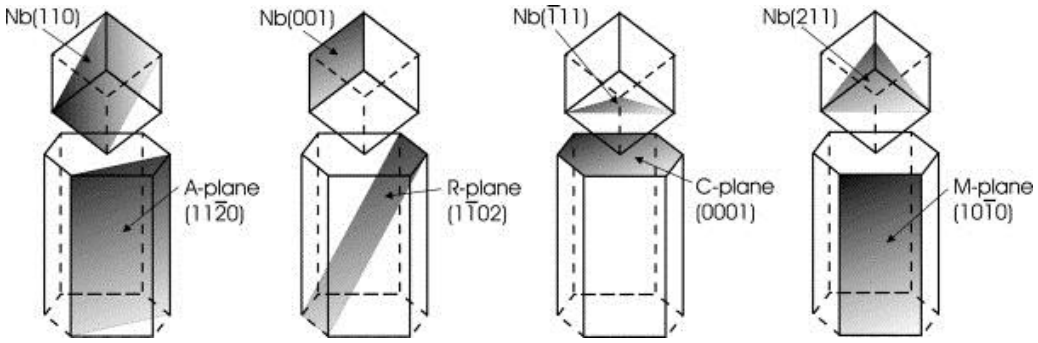

Figure 3.5: Three dimensional relationship of epitaxial niobium grown on sapphire figure from [53]

The Niobium Aluminum oxide trilayer films were all grown on A-Plane $(11\bar{2}0)$ sapphire which has one side polished for MBE. The first step in preparing the substrate is to scrub the back (unpolished) side with trichloroethylene (TCE). Next it is sonicated for five minutes each in a bath of TCE then in a bath of acetone, finally, in a bath of isopropyl alcohol (IPA). At this point the back side of the substrate is coated with 3000 Å of titanium. This titanium coating is needed because the substrate is heated radiatively in the chamber, and the clear sapphire substrates have poor absorbance in the IR; it also helps make the heating more uniform across the entire substrate. After the titanium backside coating, the front surface of the substrate is scrubbed with TCE, and the sonication is TCE, acetone, and IPA is repeated. At this point it is mounted on a substrate holder and loaded into UHV transfer tube through the loadlock. Figure 3.6 shows a substrate mounted in the substrate holder, there is a hole behind the substrate so that radiation from the heater shines directly on the back of the substrate. It is placed on a heater stage in the transfer tube and heated to about 300° C and left to outgas overnight, approximately 12 hours. This is done in the transfer tube rather than the growth chamber in order to keep the chamber as clean as possible.

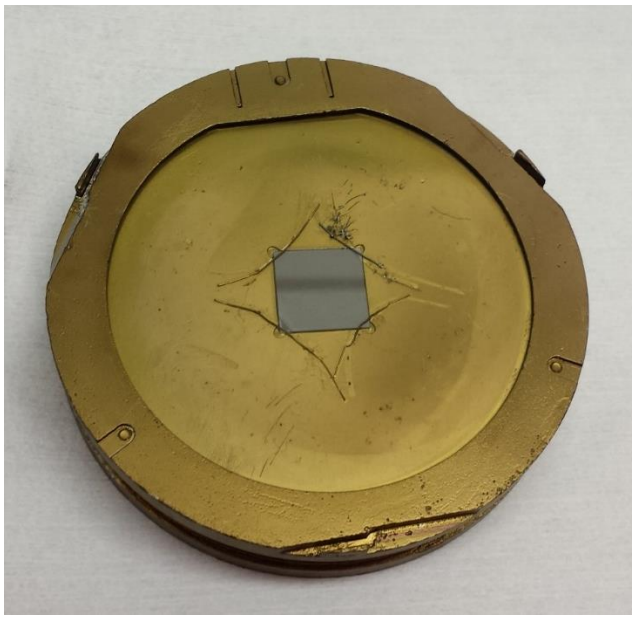

Figure 3.6: Backside Coated substrate mounted in substrate holder

3.2.2 Base layer

After the substrate has been outgassed in the tube overnight it is then loaded into the chamber to grow the base electrode layer of niobium. Once the substrate has been loaded into the chamber liquid nitrogen is started flowing through the cryo panels to cool them. The substrate is heated up to the growth temperature over the course of an hour. When the substrate is near the desired temperature, a pyrometer with its emissivity set to that of titanium ($\varepsilon = 0.58$) is used to measure its temperature and the power output of the heater is adjusted to bring it to the desired growth temperature. Figure 3.7 shows a heated substrate as seen through the pyrometer window. The niobium films in the present work were grown between 550 and 800 °C.

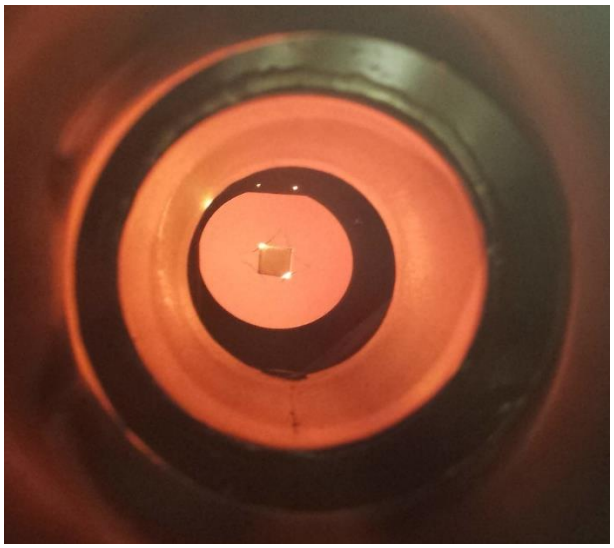

Figure 3.7: Heated substrate as seen through pyrometer window at a temperature of about 750°C.

Once the substrate is up to temperature, niobium is deposited using an e-beam evaporator. First the substrate is covered with a mask, and the shutter on the e-gun is opened. (Since the e-gun is water cooled it is important to check that cooling water is flowing before turning on the e-gun to avoid overheating it and causing damage.) The high voltage on the e-gun is slowly ramped up to 10 kV. Next the emission current is slowly increased. During the ramp up of the emission current the source material should be visually inspected periodically through a window in the top of the chamber, to ensure that the e-beam is hitting the source material and not the copper hearth. Over time the e-beam digs a hole in the niobium source material where it evaporates, so it is best to grow with the e-beam hitting a different position each time. Eventually after many growths this results in the surface of the source material being very uneven. This can be corrected by slowly sweeping the e-beam across the surface to melt the niobium back into a uniform surface.

As the emission current is increased and the niobium begins to melt, the QCM us used to measure the deposition rate, and to adjust the current to get the desired rate. The niobium films for this project were all grown at 0.3 Å/s, which happens at an emission current of approximately 200 mA. Once the desired deposition rate has been reached the substrate mask is removed and deposition begins. During the growth as the e-beam begins to dig a hole in the source material the deposition rate slowly begins to drop, and the emission current must be increased to

compensate. The niobium film is grown to a thickness of 500 Å, and the growth is stopped by closing the shutter on the e-gun. The emission current and high voltage are then ramped down.

After the niobium growth is finished the substrate heater is turned off and the substrate is allowed to cool for 3 hours, which is sufficient to bring it down to room temperature. At this point RHEED is performed on the surface of the niobium film. Figure 3.8 shows such a RHEED image. This image exhibits well defined first order streaks, an elongated specular spot and Kikuchi lines, which are indicative of long rang order across a flat surface.

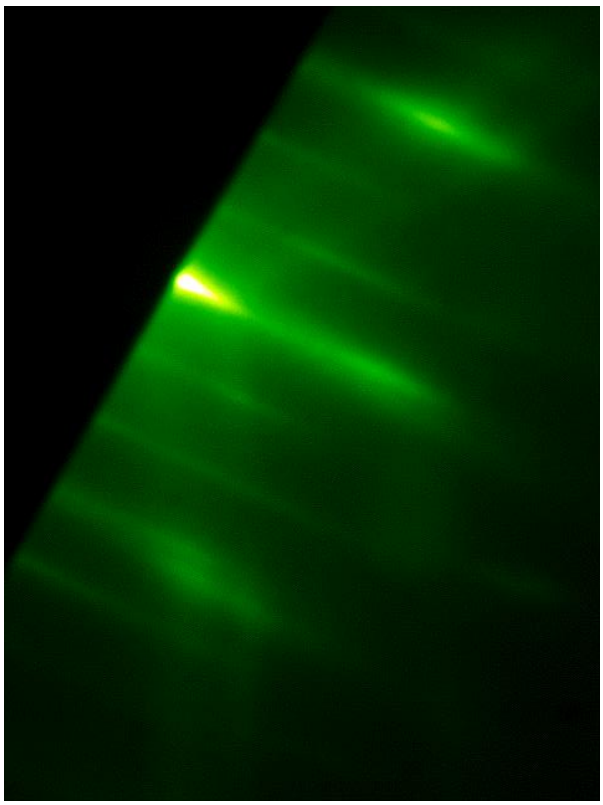

Figure 3.8: RHEED image of Niobium base layer

Atomic force microscopy can be used to confirm the flatness of the niobium film. Unfortunately it is an ex-situ technique, and so a growth must be pulled from vacuum after the niobium growth, and cannot be made into a trilayer. Atomic force microscopy (AFM) is a type of scanning probe microscopy that scans a very sharp tip across the surface of a film. The tip is at the end of a cantilever, the position of which is controlled by piezoelectric elements, and the deflection is monitored by a laser reflected off of the cantilever. In contact mode AFM the height

of the tip is adjusted to keep the deflection constant as the tip is scanned across the surface. This can result in large forces between the tip and the sample, which can result in damage to both the tip and the sample. This problem is solved by the use of tapping mode which works by vibrating the cantilever and measuring the amplitude with the laser. As the tip is brought near the surface of the film, Van der Waals repulsion dampens the amplitude. The height is adjusted with feedback to keep the amplitude constant (thus keeping the height above the surface constant) as the tip is scanned across the surface of the film. The voltage on the piezoelectric element is monitored as a function of position, and is used to make a height profile of the surface. All of the AFM images in the present work were done using tapping mode. Figure 3.9 shows an AFM image of a 500 Å thick niobium film. It exhibits single atomic layer steps, and has an RMS roughness of 155 pm.

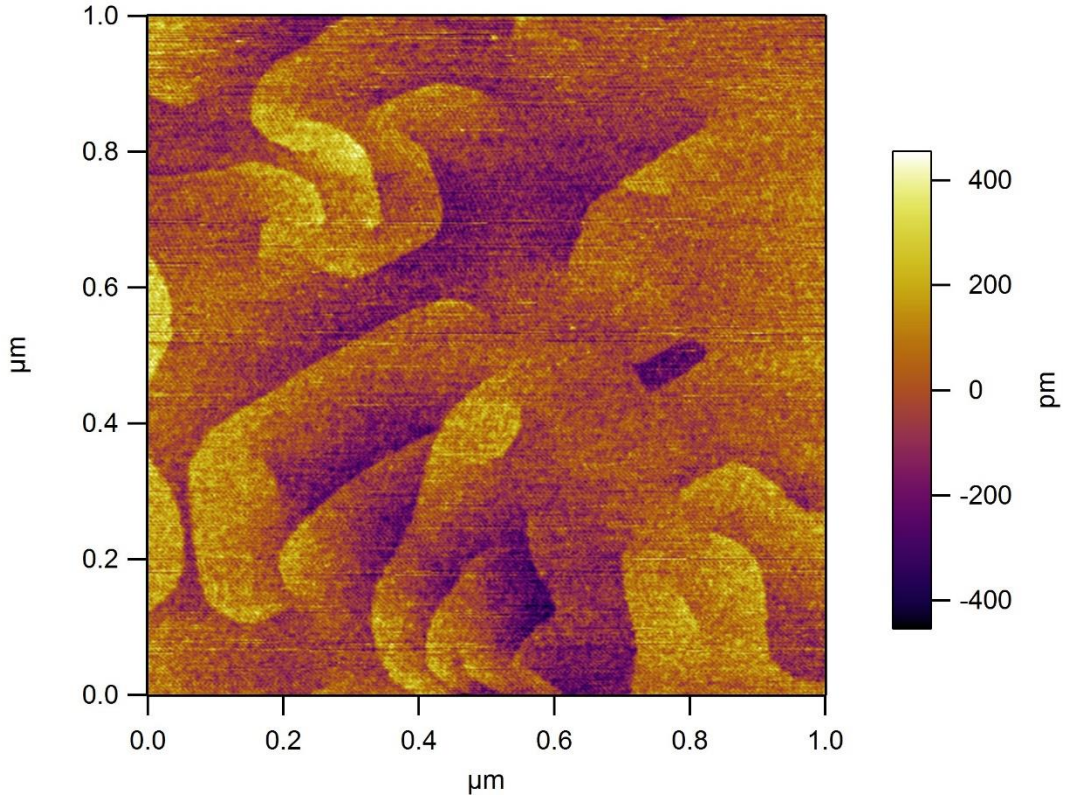

Figure 3.9: AFM image of 500 Å thick Niobium film. It exhibits single atomic layer steps, and has an RMS roughness of 115 pm.

Figure 3.10 shows an image of the interface between niobium and the sapphire substrate collected using scanning transmission electron microscopy (STEM) with an annular dark field detector by the staff of the Center for Microanalysis of Materials at the Frederick Seitz Materials

Research Laboratory at UIUC. Transmission electron microscopy (TEM) uses a beam of electrons that is transmitted through a very thin sample, then image is then focused onto an imaging device such as a CCD. STEM is an advancement of TEM that rasters a tightly focused beam of electrons across the sample; rather than focusing an image on a CCD, it uses a detector that reconstructs the image based on the location of the electron beam at the time of detection. It can either use a bright field detector, which detects electrons that pass straight through the sample, or an annular dark field detector, which detects electrons scattered into an annulus around the beam. Annular dark field images have Z contrast. In Figure 3.10 a dislocation due to the lattice mismatch between sapphire and niobium is visible.

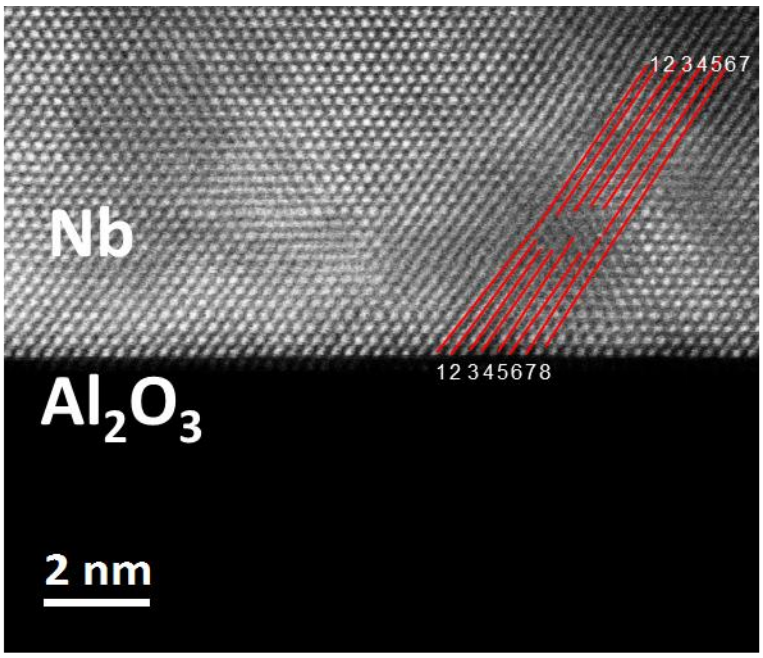

Figure 3.10: Annular dark field STEM image of niobium on sapphire substrate, shows a dislocation due to the lattice mismatch between niobium and sapphire.

3.2.3 Barrier

After the substrate has cooled down and RHEED has been taken of the niobium base layer, it is time to grow the barrier. The barrier is made of aluminum oxide, however to prevent the niobium from oxidizing during barrier growth an aluminum metal buffer layer is grown first. This layer is thin, approximately 50 Å, and proximity couples to the niobium, such that it results in a negligible change in the superconducting gap of the junctions. The barrier is formed by growing amorphous aluminum oxide by depositing aluminum in the presence of oxygen.

To grow the aluminum layer, the aluminum effusion cell is heated from its idle temperature (800 °C) to the desired growth temperature (typically around 1025 °C) over the course of 30 minutes. Then the substrate mask put in place and the aluminum shutter is opened and the aluminum deposition rate is left to settle for 60 minutes. The mask is then removed and the growth begins. The growth is two dimensional and results in RHEED oscillations that can be used to precisely determine the growth rate. As a new layer starts to nucleate the small islands of aluminum form, which reduces order on the surface, lowering the intensity of the diffracted RHEED beam. Each new atom on the surface reduces the order until 50 percent coverage is reached. At this point each new atom fills in holes in the layer, thereby increasing order and increasing the intensity of the diffracted specular reflection. Intensity reaches a maximum when the layer is complete. This process is illustrated schematically in Figure 3.11. Plotting the intensity of the RHEED image a function of time gives a sinusoid with each cycle indicating one monolayer of deposition. This allows for a very precise measurement of the deposition thickness. Figure 3.12 shows actual RHEED oscillations from an aluminum growth. The intensity of the oscillations decays as the growths shifts from a mode in which islands form and merge, to a step height disordered state where the instantaneous flatness is time independent.

Partly through the aluminum growth the RHEED is stopped and the oscillation period is measured and the growth rate calculated. Once the desired thickness of aluminum metal is grown, the mask is put in place to stop the growth.

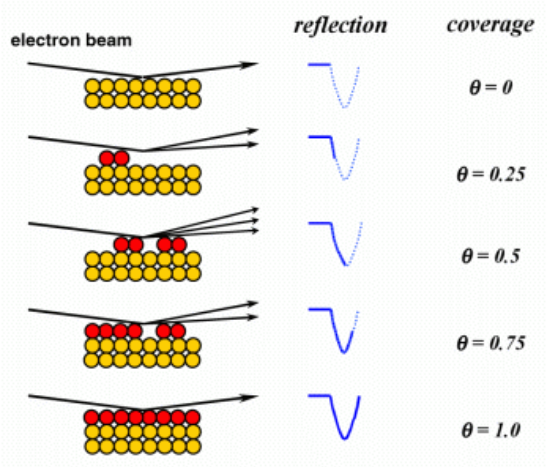

Figure 3.11: RHEED intensity oscillates as a function of time, going through a full cycle with each monolayer deposition, Image from [54].

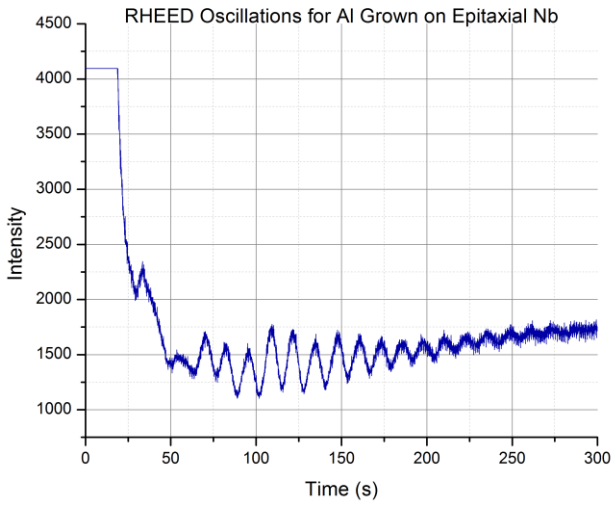

Figure 3.12: RHEED Oscillations from aluminum grown on niobium.

At this point the oxide is grown. The chamber pressure is brought up to the desires oxygen pressure (typically $5x10^{-6}$ Torr) using the oxygen injector described earlier. Once the oxygen pressure has been stabilized (the needle valve must be constantly adjusted to keep the pressure stable) the mask is removed and the oxide is grown for the desired thickness (5-15 Å) using the very accurate deposition rate of the aluminum from the RHEED oscillations during the aluminum metal step and stopped with the aluminum shutter with the oxygen beam left on for an additional 30 seconds. I estimate the oxygen flux at the surface of the substrate to be approximately 100 times larger than the aluminum flux.

After the oxygen is turned off, the chamber is left to pump down below 10^{-8} Torr which takes approximately 45 minutes. The substrate is then moved to the oxidation chamber, which has a base pressure of around 10^{-9} Torr. The chamber is brought up to 30 Torr of UHP oxygen and the sample is exposed to this oxygen environment for 60 minutes. This is to allow the oxygen to diffuse into the aluminum oxide and fill any vacancies. It also oxidizes the aluminum underneath, covering any pinholes in the oxide layer, preventing shorting through these pinholes. Once this oxygen exposure is complete the oxidation chamber is pumped to below 10^{-8} Torr, and the sample is returned to the growth chamber (System E).

Figure 3.13 shows a STEM (bright field) image of a thick amorphous aluminum oxide layer on top of the single crystal (111) aluminum on top of the niobium.

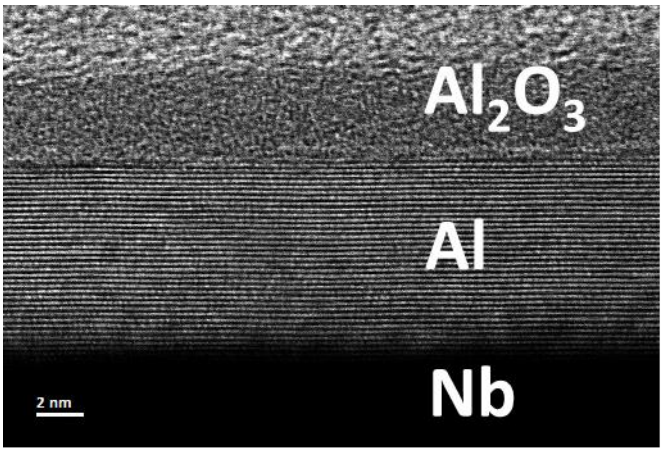

Figure 3.13: Bright field STEM Image showing amorphous aluminum oxide on single crystal aluminum on top of niobium

3.2.4 Counter electrode

At this point the niobium counter electrode is grown. It is grown in the same way that the base electrode was grown except that it is grown with the substrate at room temperature. This is to prevent oxygen from diffusing out of the barrier into the niobium above and aluminum below. Since the aluminum oxide layer that the counter electrode is grown on is amorphous, this layer will be polycrystalline regardless of the growth temperature. The counter-electrode is typically grown to a thickness of 500 Å.

3.3 Self-Aligned Process

We have developed a novel self-aligned process for the fabrication of small Josephson junctions from trilayer films for use in qubits. It eliminates the need to create a via-hole which can be difficult to align on small devices. It can create small area junctions using only three lithography steps without requiring precise alignment. The dimensions of the junctions are defined by 2 separate lithography steps, one for each in plane direction. This way each lithography step only has one critical dimension.

A schematic of this process is outlined in Figure A.1. Starting with an MBE trilayer film (Figure A.1 A), grown as outlined in the previous section, the film is patterned using both e-beam

and photo lithography. It is then etched into a narrow bar (Figure A.1 B). Reactive ion etching is used to etch through the niobium and an acid etch is used to etch through the aluminum and aluminum oxide

Following the device isolation etch, the sidewalls are electrically passivated by coating with a dielectric (Figure A.1 C) using atomic layer deposition. This is done with the photoresist from the etching still in place. The photoresist protects the surface of the top electrode from being coated with dielectric.

Next a wire-up layer of niobium with an aluminum cap is deposited across the device isolation bar (Figure A.1 D). This wireup layer is deposited using magnetron sputtering.

The wafer is then placed in the RIE, and the niobium of the top electrode is etched away except where it is protected by the aluminum of the wireup (Figure A.1 E), leaving a junction formed where the wire-up crosses the device isolation bar, a schematic of which is shown in Figure A.1 F. This process is discussed in greater detail in Appendix A.

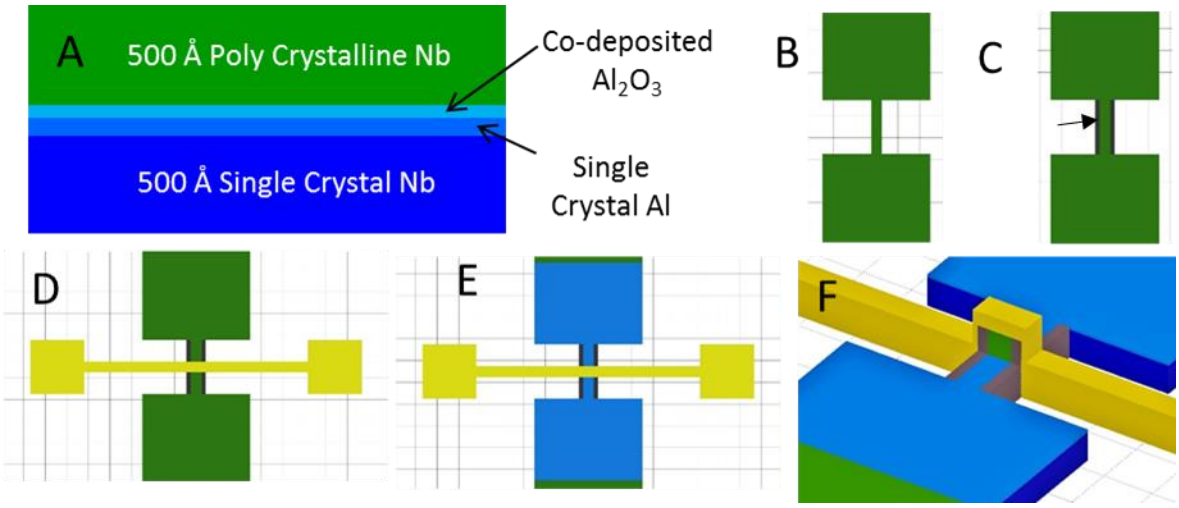

Figure 3.14 Schematic of Self aligned process. Images courtesy of Allison Dove.

3.4 Results

3.4.1 Transport

Completed junctions had their electrical transport tested using a four point measurement. Probes for the positive and negative voltage, and for the positive and negative current were connected to the device. Each lead had a 1000 ohm resistance to reduce noise. Current was supplied by the use of a function generator, outputting a triangle wave at a frequency of 1 Hz. Current was measured, by connecting a 500 ohm resistor in series with the device, and measuring the voltage across it. The voltage across both the device and the current sensing resistor were measured using a low noise preamplifier connected to a DAQ board. Temperature is measured using a DT-470 temperature sensing diode.

The device is slowly lowered into a bath of liquid helium and the resistance is measured as a function of temperature. The resistance is measured by fitting a line to the I-V curve. Such a measurement for a typical is shown in Figure 3.15. The resistance rises as the temperature is lowered and then levels off. This is due to the fact that at high temperatures, electrons are thermally excited above the Fermi level, reducing the relative height of the barrier and increasing the probability of tunneling. The sharp upturn in resistance at T_C is due to measuring the resistance in the gap of the junction.

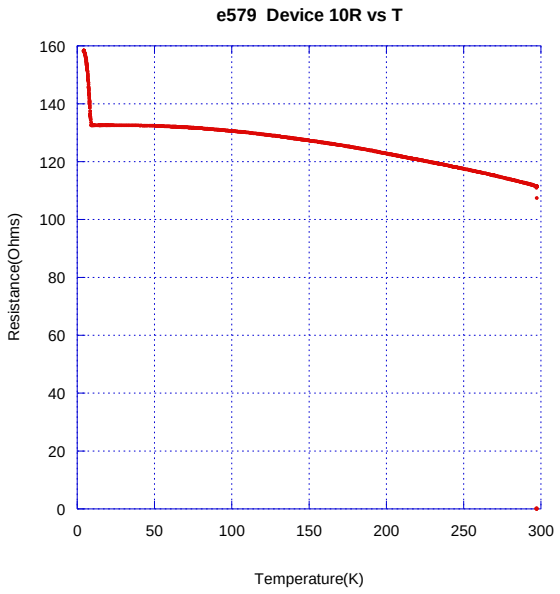

Figure 3.15: Resistance vs. Temperature of a typical niobium Josephson junction.

Once the junction is fully cold (4.3 K), an I-V curve of the junction is taken. Figure 3.16 shows the I-V curve of a good junction. The super current is suppressed due to noise in our testing setup. This essentially reproduces the current-voltage characteristics of an ideal junction. There is very little current, and no differential resistance in the gap region, and a sharp turn up of current at 2Δ. Unfortunately, this is not the only junction characteristics that were seen, and in fact were in the minority. There were several kinds of defective junctions that we found. The first problem we found is shown in Figure 3.17. Rather than the current being flat in the gap region, it increases linearly with voltage. This is indicative of a resistive short in parallel with the junction itself. This is most likely explained by the ALD coating on the sidewalls chipping off during liftoff, allowing the wireup to make a partial short to the base electrode.

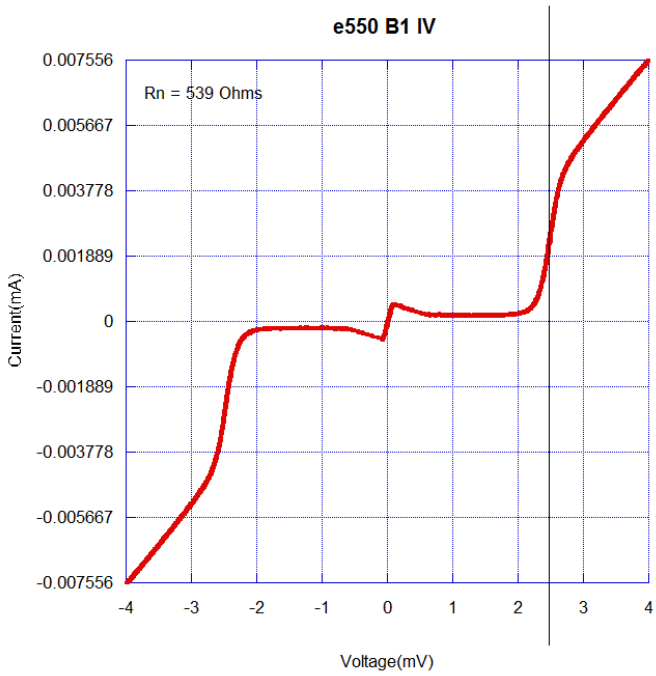

Figure 3.16: I-V curve of a good junction.

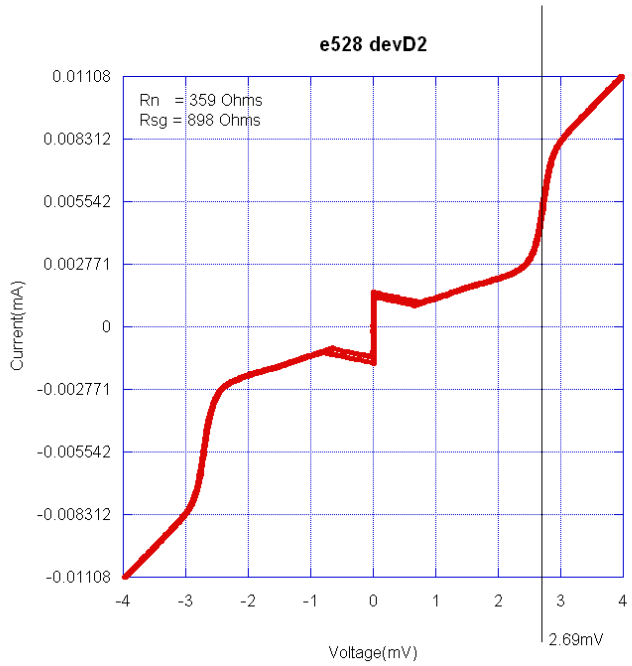

Figure 3.17: Junction with resistive shorting.

The other two kinds of problems are more baffling. The first type of problem is what we refer to as “bowing” in the gap region. This type of device is shown in Figure 3.18. The current slopes up in the gap region, but it is not ohmic. The intercept for projecting the current in the gap to zero voltage is not at zero, as one would expect for a resistive short, but is in fact negative.

The other type of defective Josephson junction is shown in Figure 3.19. This junction appears almost as if it is a NIS (normal metal-insulator-superconductor) junction, rather than a standard Josephson junction which is SIS (superconductor-insulator-superconductor). It is possible that this is actually the same problem as the bowing in the gap, but much stronger, such that it overwhelms the normal junction characteristics.

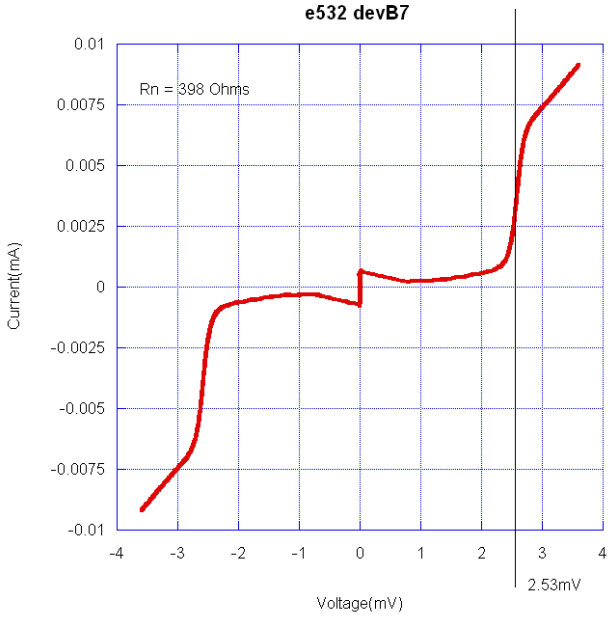

Figure 3.18: Junction with "bowing" in the gap.

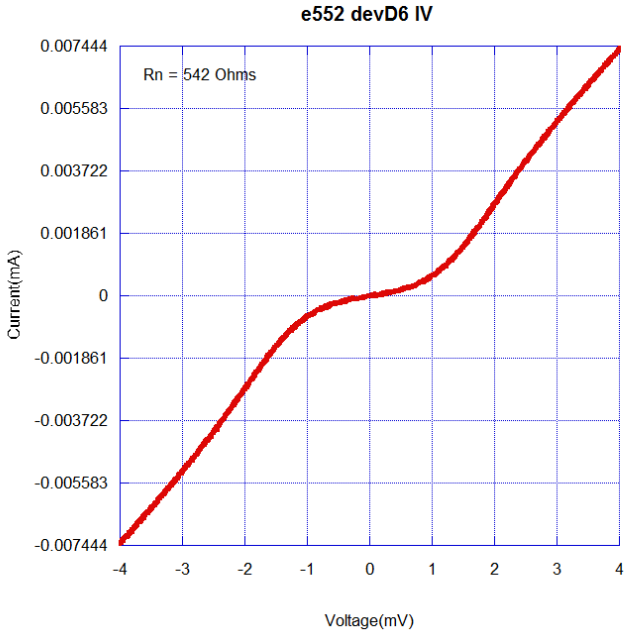

Figure 3.19: Junction with NIS like I-V curve.

3.4.2 Scaling with Barrier Thickness

We studied the effect of different barrier growth conditions on the normal state resistance of the junctions. This resistance can be related the critical current of the junction using the Ambegaokar-Baratoff relation [55]:

$$J_c = \frac{G_n}{A}\left(\frac{\pi\Delta(T)}{2e}\right)\tanh\frac{\Delta(T)}{2k_bT}$$

Where J_C is the critical current density, G_n is the normal state conductance, A is the area of the junction, and Δ(T) is the superconducting energy gap. Using the approximation that in the range of interest the hyperbolic tangent is approximately 1, and Δ(T) is approximately Δ(0), this can be rearranged to:

$$J_C R_n A = \frac{\pi}{2}\frac{\Delta}{e}$$

Where R_n is the normal state resistance. For niobium, Δ is approximately 1.3 meV, which leads to:

$$J_C R_n A \approx 2mV$$

This allows us to get J_C once the resistance is measured. The shape of R_nA vs temperature is known, so that measuring the resistance at room temperature suffices to reveal how different barrier growth processes lead to different junction characteristics.

Figure 3.20 shows the normal state resistance versus barrier thickness for different growth conditions; each data point is obtained from a different wafer. The barrier thickness is given in monolayers of aluminum, which is the amount of aluminum needed to grow 1 monolayer of (111) aluminum (which is 2.34 Å thick). This is the natural thickness variable to use, because the aluminum rate as measured by RHEED oscillations is given in monolayers per second. Graded O_2 dose means that at the start of the growth the pressure of oxygen in the chamber was $5x10^{-7}$ Torr and was gradually increased to $5x10^{-6}$ Torr, by doubling the oxygen pressure after each fifth of the total thickness was grown. For increasing oxygen pressure resistance of the junctions at a given rate increased. The slope of the log(R_nA) vs barrier thickness also increased. This shows that for the lower oxygen pressure growths, the aluminum oxide was not fully oxidized, allowing some leakage current though the barrier.

We also measured how the length of the oxygen anneal following the growth of the barrier affects the subgap leakage. This is measured by dividing the quasiparticle current above the gap (at 3 millivolts) by the leakage current in the gap just before the current begins to turn up. This shown in Figure 3.20. All barriers were grown at an oxygen pressure of $5x10^{-7}$ Torr, and then exposed to oxygen in the oxidation chamber for varying doses. Longer exposure results in lower leakage (i.e. higher ratio or quasiparticle current to leakage current) indicating that the barrier is not fully oxidized during growth.

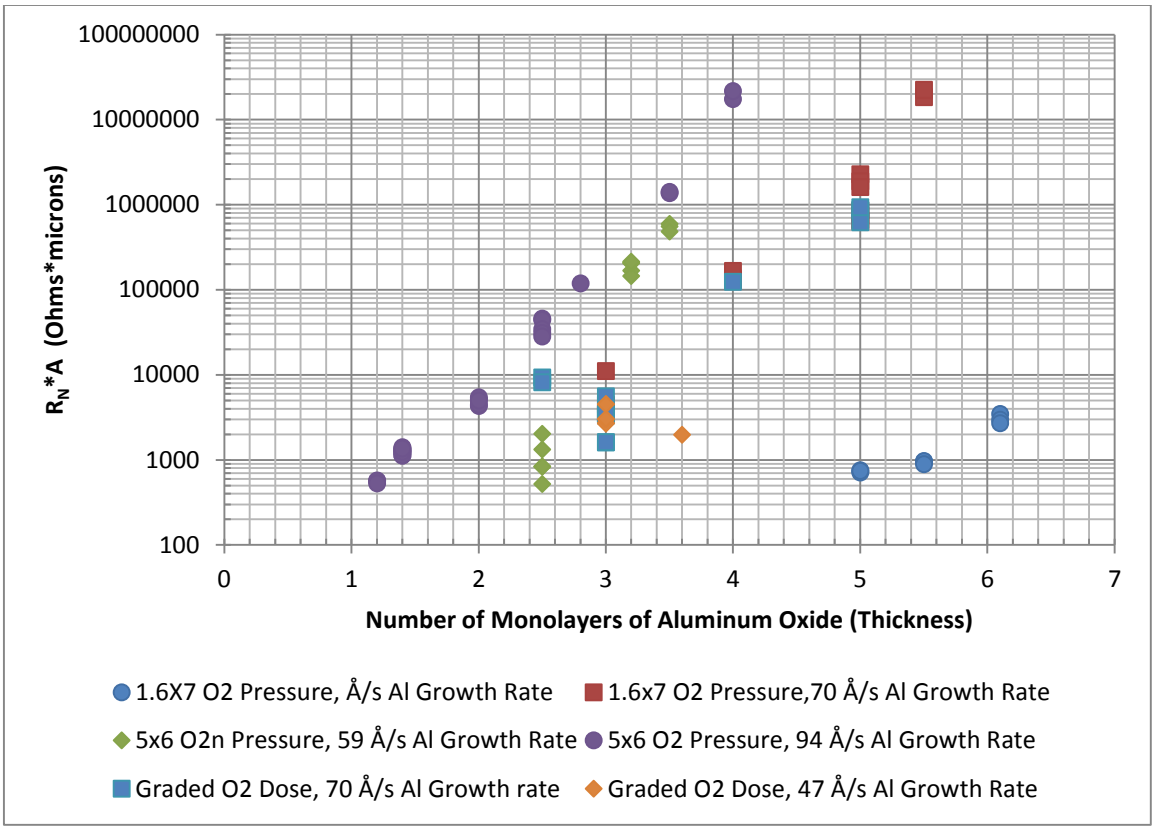

Figure 3.20: Normal state resistance versus barrier thickness for various growth conditions.

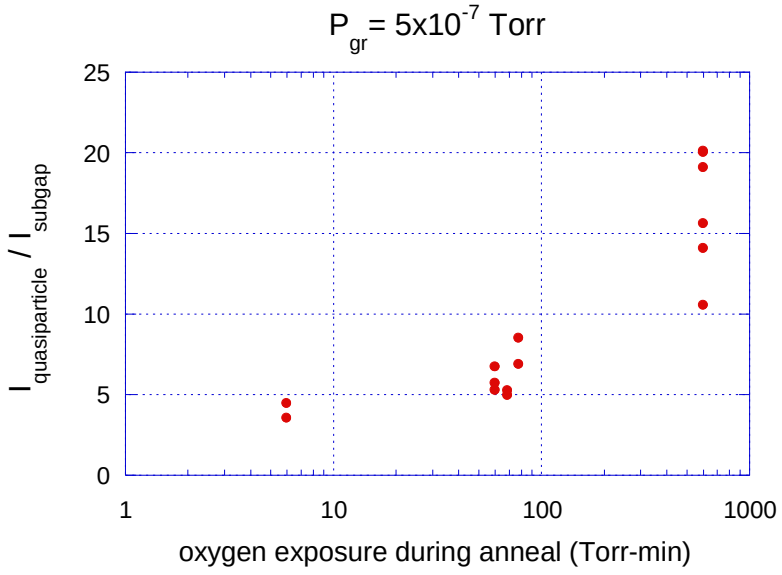

Figure 3.21: Effect of the oxygen exposure after the growth of the barrier on the subgap leakage.

3.4.3 Scaling with Area

We fabricated on each substrate a 10 x 10 array of junctions, with each row having a different size of junction. Figure 3.22 shows a subset of one of these arrays. Each junction has contact pads to make four point measurements using a probe station at room temperature. Figure 3.23 shows the room temperature resistance plotted versus nominal area for one such array, which is typical of the results we have achieved. The resistance should scale inversely with area, for successful junctions. This allows us to quickly asses the yield of our process at different sizes. The yield is essentially perfect above 1 square micron, with many shorted junctions at and below 1 square micron. The slope of the graph also increases at the lower end of the nominal area, indicating that the actual area of the junctions is smaller than the nominal area for these sized. Because the problems with bowing and the NIS like junctions only show up below TC, this array cannot detect this failure mode; it can only find the number of junctions that are shorted.

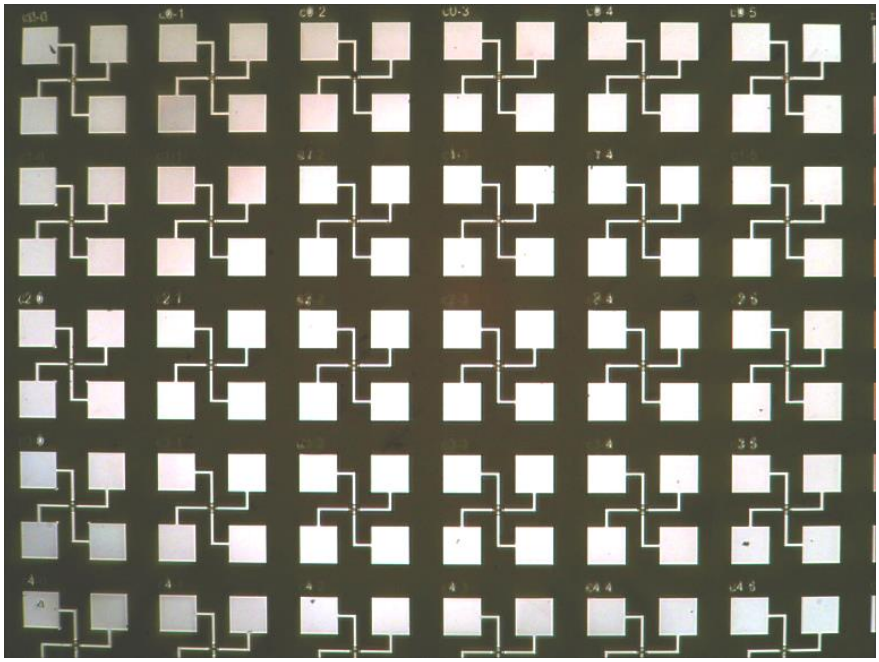

Figure 3.22: Part of junction array to test area scaling.

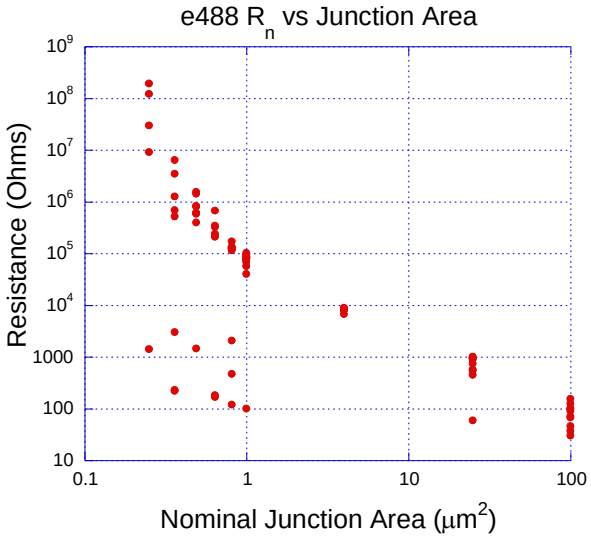

Figure 3.23: Room temperature resistance of junctions plotted against nominal area.

3.4.4 Imaging

In order to diagnose the shorting problem that we were having with our junctions, we imaged them. First AFM was performed. An AFM image of a junction is shown in Figure 3.24. The purple bar from the upper left to the lower right is the niobium base electrode covered with the aluminum oxide barrier from the device isolation that is left after the final etch. The orange bar that goes from lower left to upper right is the wireup. The junction is the lighter colored square in the center. There are raised strips along either side of the device isolation bar, which referred to as "rabbit ears." We originally believed that these rabbit ears were caused by incomplete etching of the top electrode during the final etch, however after several attempts at using more aggressive etches to, remove theses rabbit ears nothing succeeded, and in fact some seemed to make them worse.

We needed a new imaging technique to figure out what was happening. The problem with AFM is that is only provides a height profile, which gives a top down view of the device. With scanning electron microscopy (SEM) we can get a side view by imaging at an angle.

SEM works by rastering an electron beam across the surface and detecting secondary electrons emitted by atoms which have been excited by the electron beam. SEM images can

resolve features less than 1 nm in size, which is about 250 times better than the best optical microscopes. Figure 3.25, Figure 3.26, and Figure 3.27, are SEM images of the device isolation bar. These figures show that the rabbit ears seen in AFM are caused by the film delaminating from the substrate at the edges of the bar and curling upwards. This seems to be caused by the RIE etch undercutting the aluminum barrier, and etching inwards on the base electrode niobium, which delaminates it from the surface. Strain from the growth then causes it to curl up.

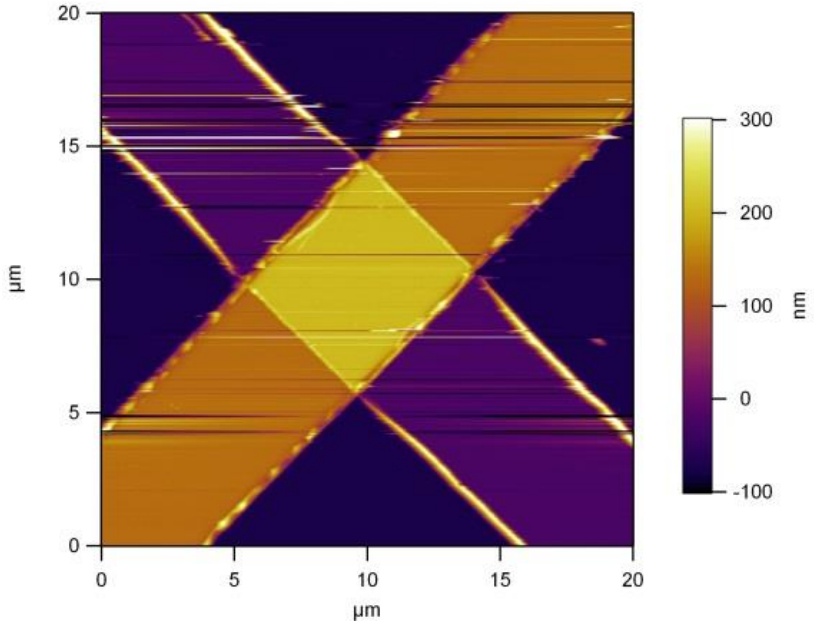

Figure 3.24: AFM of a junction reveals large rabbit ears on sides of device isolation bar.

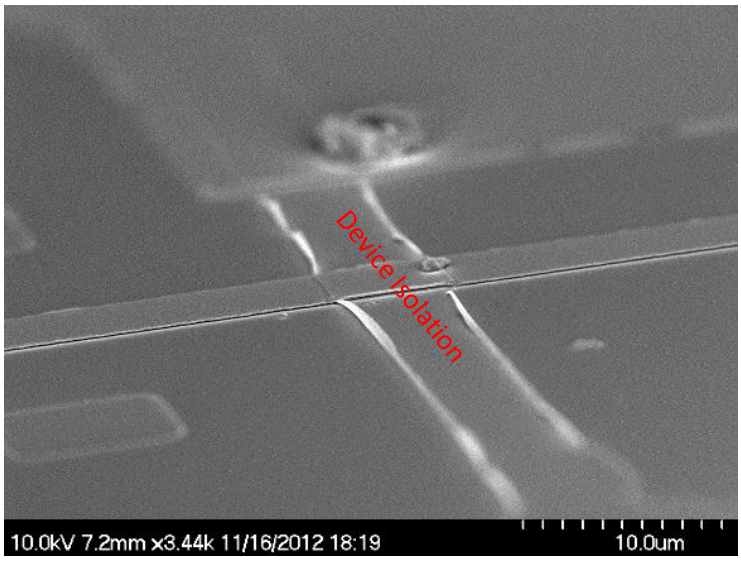

Figure 3.25: SEM image of junction reveals that rabbit ears are edges of the device isolation bar curling up

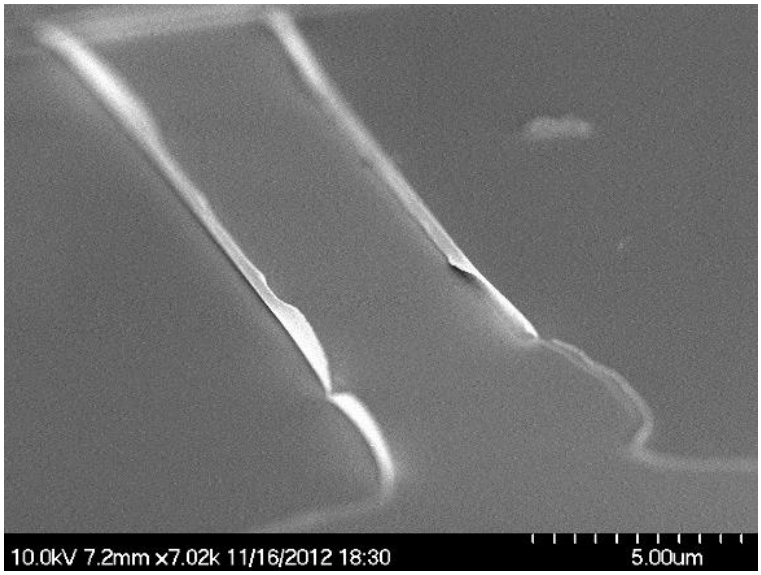

Figure 3.26: A closer view of the curling at the edges of the device isolation bar

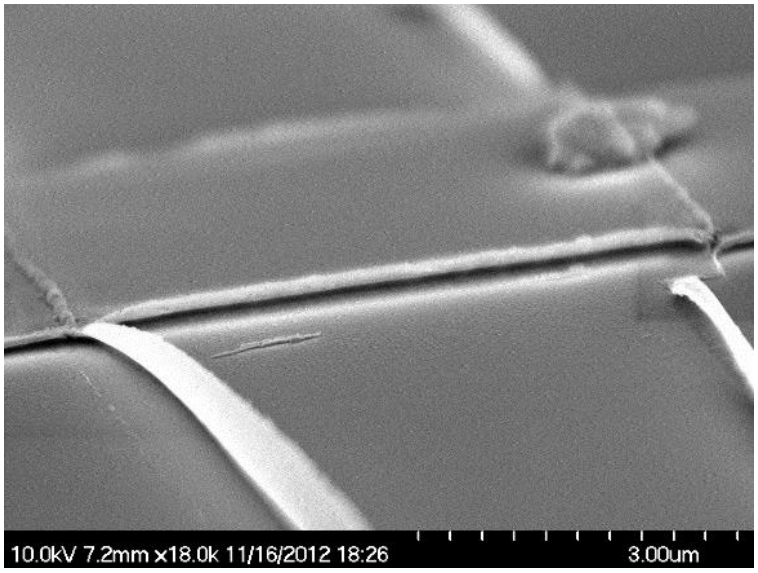

Figure 3.27: Curling of the device isolation bar near the junction.

After discovering this curling, we decided to study the undercutting caused by the RIE etch. I grew niobium films on silicon, with an aluminum etch mask on top. Since aluminum is impervious to SF_6 RIE etches, an aluminum etch mask allows me to study the effect of the etch recipe independently from the effect the etch recipe on PMMA. After etching the wafers were cleaved to allow a cross sectional view of the etch profile. The thickness of the niobium was such that the standard niobium RIE etch, could etch through it in 60 seconds. Figure 3.28 shows the effect of the standard niobium etch after 120 seconds on such a sample. The overhang is the aluminum etch mask, with the niobium undercut very far. This means that the standard niobium etch—which had been selected due to its slow etching of PMMA—is not very directional.

It is known that decreasing the pressure of an RIE etch can increase the directionality, by making the etch rely more on physical sputtering and less on chemical reaction. A small amount of oxygen can also be added to the etching gas, to passive the sidewalls against reacting to the fluorine ions. The surface is not affected by this because the physical sputtering is enough to remove the oxide layer and allow the fluorine ions to react with the niobium underneath. I developed an etch recipe that uses 20 SCCM of SF_6, 1 SCCM of O_2, a pressure of 82 mTorr, and a power of 15 Watts. Lowering the pressure increases the etch rate of niobium, lowering the

power 15 Watts (compared to 35 Watts for the standard etch) lowers the etch rate to keep it the same as the standard etch recipe. Figure 3.28 shows the effect of this new etch. This etch has no undercut and sloping sidewalls. This etch attacks PMMA at a much larger rate than the standard etch, and would require increasing the thickness of the PMMA used to pattern the device. However due to reasons that will be discussed in section 3.5, it was decided to move away from making niobium Josephson junctions, and study of the necessary adjustments to the fabrication process to prevent curling of the edges of the device isolation bar was not pursued further.

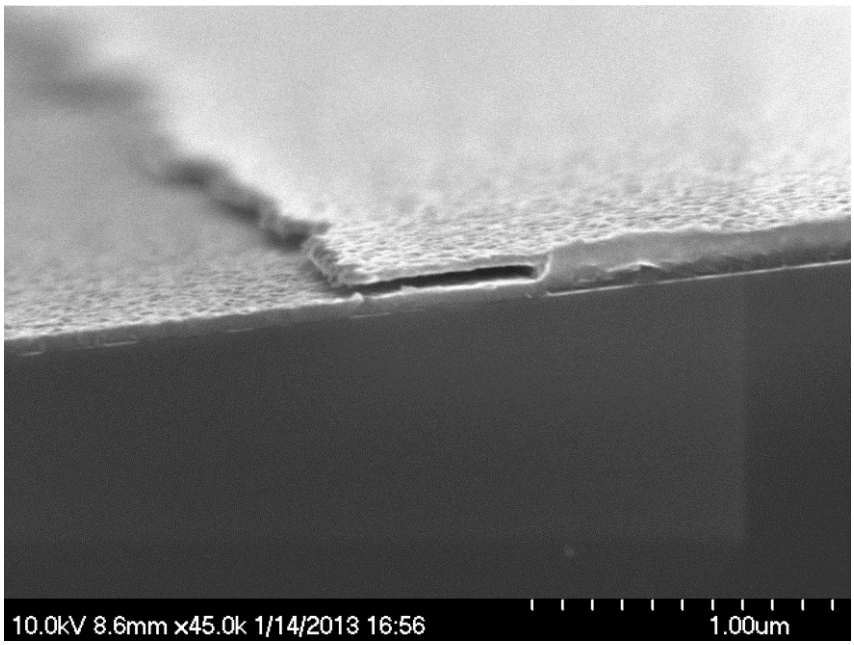

Figure 3.28: Standard niobium etch creates large undercut.

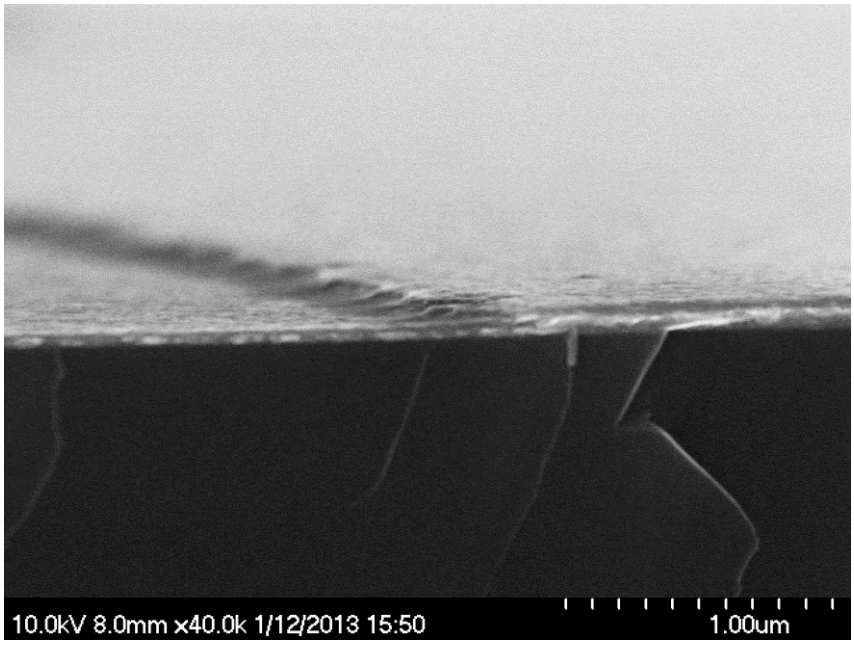

Figure 3.29: Lowering the pressure and adding oxygen to the etch recipe gets rid of undercut.

3.4.5 Transmons

Trilayer junctions made using the self-aligned process were fabricated into 3D transmon qubits. Figure 3.30 shows such a qubit. These qubits were tested by the Siddiqi group at University of California at Berkeley. They measured T1 and found it to be 1.2 microseconds, as shown in Figure 3.31. They also performed a Ramsey experiment to measure T2*, which they found to be 850 nanoseconds, as shown in Figure 3.32. Theses coherence times are considerably shorter than the coherence times measured from 3D transmons made of aluminum (e.g. Paik found T_1 on the order of 50 microseconds [28]), which are on the order of 10s of microseconds. The reason for this short coherence time may be in part due to defects from processing but it is consistent with decoherence from quasiparticle tunneling. Theoretical work—which is discussed in the next section—puts a limit of 20 microseconds on T1 for niobium transmons due to quasiparticle tunneling.

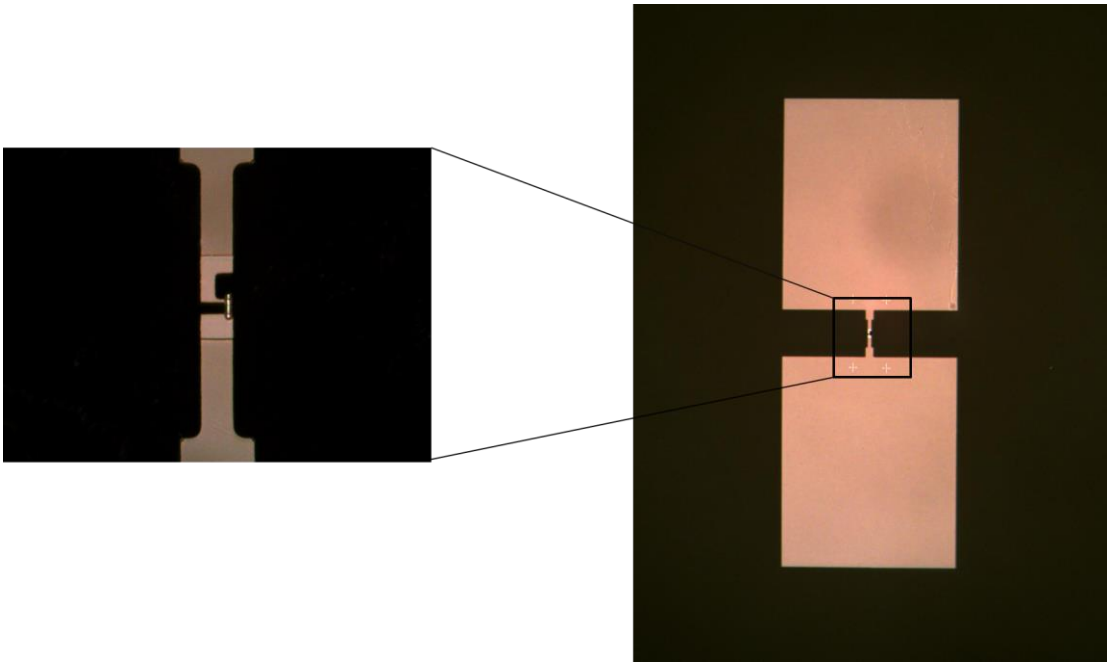

Figure 3.30: 3D transmon fabricated using self-aligned process.

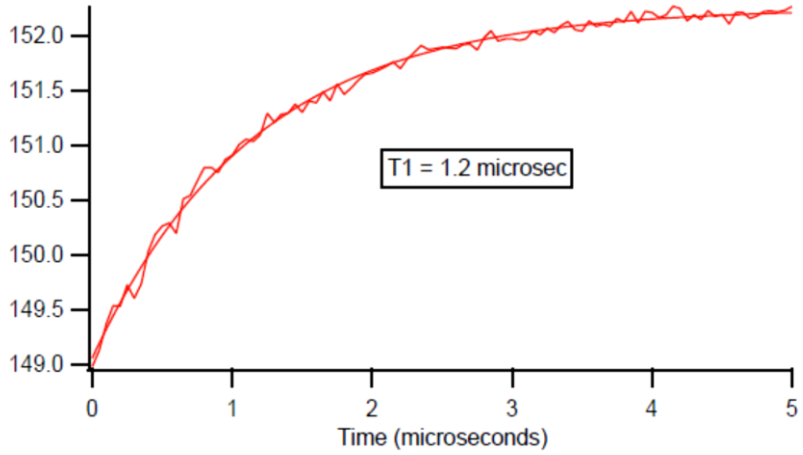

Figure 3.31: T_1 measurement of niobium trilayer 3D transmon qubit, gives T_1 of 1.2 microseconds.

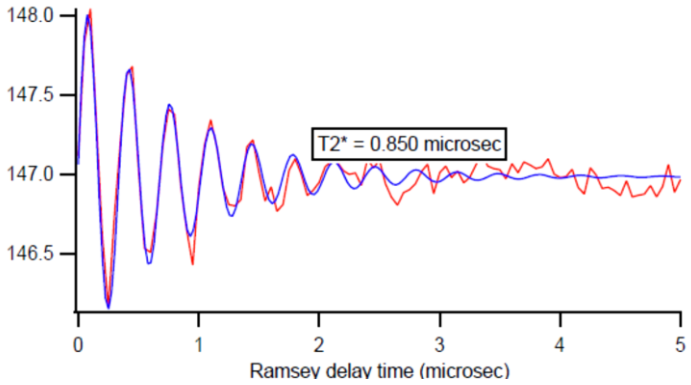

Figure 3.32: Ramsey measurement of niobium trilayer transmon qubit, shows a T_2 of 850 nanoseconds.*

3.5 Decoherence to Quasiparticle tunneling

Leppäkangas and Marthaler analyzed the decoherence of superconducting qubits due to quasiparticle tunneling [47]. They considered two types of quasiparticle sources. The first source is non-equilibrium quasiparticles, which is caused by quasiparticles diffusing from higher temperature regions of the sample, or from stray radiation. The second source of quasiparticles is the breaking of a Cooper pair which occurs if there is an extended quasiparticle density inside the energy gap. Measurements have shown that non-equilibrium quasiparticles dominate in aluminum while, subgap quasiparticle energy states dominate in niobium. They calculate the relaxation (T_1) and dephasing (T_2) times of various types of qubits using quasiparticle densities reported by experiments. They found that the dephasing rate was dominated by relaxation, rather than pure dephasing. They found that the calculated relaxation rate for niobium qubits was much higher than for aluminum qubits. Their model reproduced the coherence times that had been seen for niobium flux qubits, indicating that, niobium flux qubits were limited by quasiparticle tunneling. For transmon qubits, they calculated a maximum relaxation time of 20 microseconds due to quasiparticle tunneling, while for aluminum is was 1.2 milliseconds.

They find that T_1 is given by

$$T_1 \approx CR_n \left(\frac{\Delta}{\Gamma_D}\right)^2$$

Where C is the capacitance of the transmon, R_n is the normal state resistance of the junction, and Γ_D is the Dynes parameter, which describes a broadening of the energy gap edge in the quasiparticle density of states:

$$N(E) = Re\left\{\frac{E + i\Gamma_D}{\sqrt{(E + i\Gamma_D)^2 - \Delta^2}}\right\}$$

Transport data of the junction in the transmon can be used to estimate Γ_D, whichis approximately one quarter of the full width half max of the differential conductance peak around 2Δ [56]. Figure 3.33 shows transport data for a junction that was made the same way as the transmon measured above. This junction has the same design and went through the same fabrication steps, so it should be a reliable guide to the junction in the measured transmon. I too the derivative of this curve, which is shown in Figure 3.34. I found that the conductance peak has a full width half max of 0.093 mV, which corresponds to a Dynes parameter of 0.023 mV. This corresponds to $\frac{\Gamma_D}{\Delta}$ = 0.0195 (by using Δ = 1.2 mV). This transmon had a capacitance of 135 femto farads, and a resistance of 9.8 kilo ohms, which results in a relaxation time of 3.7 microseconds, which is in rough agreement with the measured relaxation time of 1.2 microseconds.

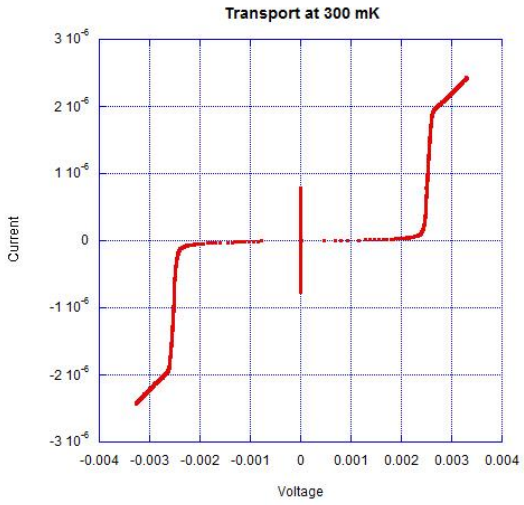

Figure 3.33: Transport data for a junction that matches the one in the transmon measured above.

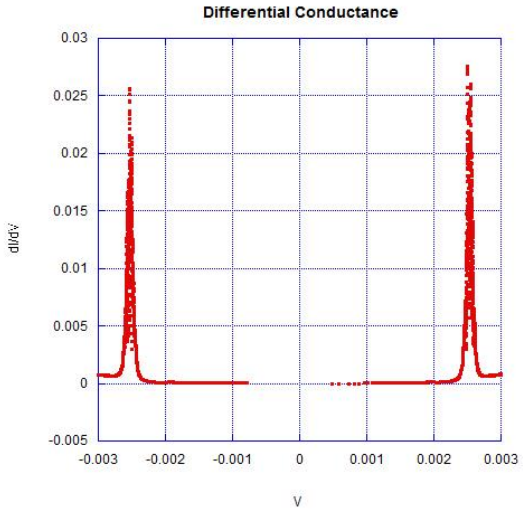

Figure 3.34: Differential conductance, of junction that matches the one in the transmon measured above.

Given the low coherence times that we have been able to achieve with niobium transmons, as well as the analysis by Leppäkangas and Marthaler showing that quasiparticle tunneling limits the achievable coherence times of niobium much shorter than that of aluminum, as well as the fact that others have seen a decrease in coherence in niobium qubits relative to aluminum qubits [57], it was decided that our work with niobium was not worth pursuing. At this point we abandoned work to try to improve the self-aligned process for making niobium Josephson junctions, and began adapting our use of MBE to making shadowmask aluminum junctions.

Chapter 4 Aluminum Qubits

In this chapter I will discuss the fabrication of aluminum shadow mask qubits. Aluminum allows for the fabrication of qubits using shadowmask evaporation because single crystal aluminum can be grown at room temperature on clean c-plane sapphire. Shadowmask evaporation presents fewer challenges than the etching based process required for fabricating junctions from trilayers. In section 4.1 I study the growth of aluminum films using careful substrate preparation. I have achieved the growth of flatter films than those Megrant in [45]. In section 4.2, I discuss the process I used for making qubits using shadowmask evaporation. After growing these junctions, the top electrode is coated with various in situ dielectrics in order to prevent the formation of a native oxide. I discuss this process in section 4.3.

4.1 Aluminum Film Growth

Before fabricating transmons I first studied how to achieve the best aluminum film possible. In this section I will discuss the growth procedure that I developed which was based off of the work of Megrant et al [45].

4.1.1 Substrate Preparation

The first step to growing aluminum films is choosing a substrate and preparing it for growth. Sapphire is a good substrate, due to its low microwave loss tangent $\delta \sim 10\text{-}8$ [58]. Megrant et al [45] used C-plane sapphire. We decided to try both C-plane sapphire and A-plane sapphire. As shown below, the results on the C-plane sapphire were considerably better.

The first step in preparing the substrate is to perform ultrasonic cleaning using TCE, acetone, and IPA as described in section 3.2.1. These substrates do not need to be backside coated with titanium, because the substrates are mounted on closed back substrate holders and the growths are done at lower temperatures. After the substrates are cleaned they are annealed in a tube furnace at 1100 °C in an environment of UHP oxygen at atmospheric pressure for six hours. This is inspired by the in situ oxygen plasma anneal performed in [45] which may fill in oxygen vacancies near the surface of the substrate.

After the oxygen anneal is complete, the substrate undergoes ultrasonic solvent cleaning again. Then it is etched for 30 seconds in Buffered Oxide Etchant (BOE). BOE is a mixture of hydrofluoric acid (HF), ammonium fluoride (NH_4F) and water. The ammonium fluoride acts as a buffer which reduces the etching rate, and keeps the PH constant as the HF is used up in the reaction. We believe that the BOE acts to chemically roughen the surface providing more nucleation sites, which leads to a flatter film. After the BOE etch the substrate is rinsed with deionized water and blown dry with nitrogen. The substrate is then mounted on a substrate holder and loaded into the vacuum system.

4.1.2 Growth Procedure

Once the prepared substrate is loaded into the MBE chamber, it is heated to about 135 °C. This is done by running the substrate heater at 10 W. The temperature reading is from the substrate thermocouple in system F, because the pyrometer cannot measure temperatures this low. The substrate is left at this temperature overnight to outgas. The next morning the liquid nitrogen cryo panels are cooled, which brings the pressure in the chamber to about $5x10^{-11}$ Torr. After this the aluminum cell is ramped up to a temperature of 1125 °C over the course of 15 minutes. The mask is then put in place over the substrate and the aluminum shutter is opened and the aluminum deposition rate is left to stabilize for 5 minutes. We begin the growth by removing the mask. The aluminum is deposited for the desired amount of time to grow the desired thickness. Unfortunately the QCM is poorly positioned to receive flux from the aluminum cell, and so gives an unreliable measure of the deposition rate. However, the deposition rate of effusion cells at a given temperature is very reproducible. The rate can be calibrated by growing a film at a given temperature for a set amount of time, then etching a region of the film down to the substrate, and finally using AFM to measure the height of the step edge the created by etching which provides us with the thickness. Dividing the measured thickness by the deposition time gives the deposition rate. At 1125 °C the deposition rate in our system was found to be 0.72 Å/s in system E and 0.6 Å/s in system F.

4.1.3 Results

The aluminum film grown on the untreated a-plane sapphire was granular with an RMS roughness of 6.5 nm, as shown in Figure 4.1. The film grown on untreated c-plane sapphire was much smoother, with an RMS roughness of 2.6 nm, as shown in Figure 4.2. This demonstrates that c-plane sapphire is the better choice of substrate. Additionally, the surface of the aluminum grown on the c-plane sapphire that had been prepared with an 1100 °C oxygen anneal and a 30 second dip in BOE, was much smoother than the film grown on the untreated sapphire. With an RMS roughness of only 0.2 nm, the surface was approximately half as rough as the best film grown by Megrant et al in [45]. An AFM image of the surface of this film is shown in Figure 4.3. One can see that the surface is smooth with regularly spaced striations. Zooming in on one of these striations, one can see that they are about 1.7 nm deep and have a width of about 100 nm as shown in Figure 4.4. Although they look very deep due to the height exaggeration of the AFM image, the sidewalls only have a slope of approximately 2 degrees.

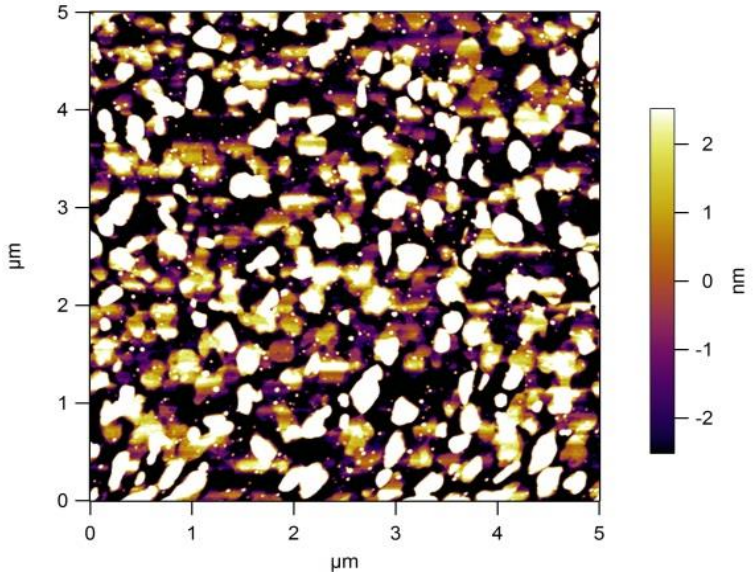

Figure 4.1: AFM image of aluminum grown on untreated A-Plane sapphire has an RMS roughness of 6.5 nm.

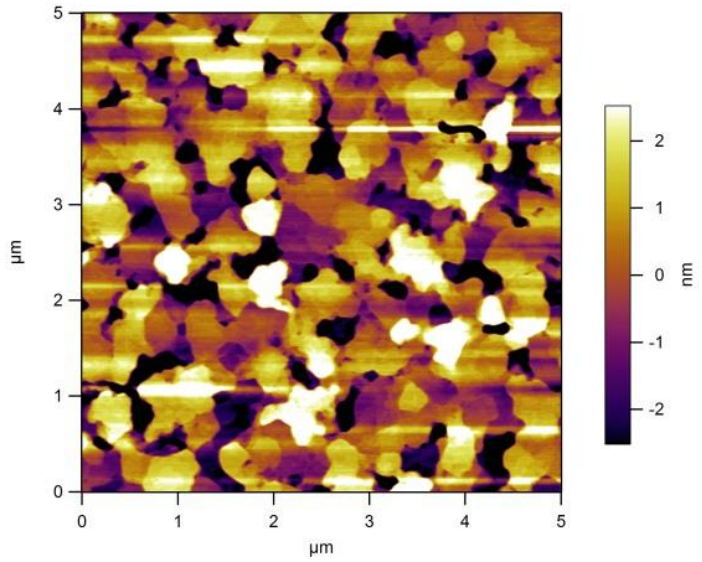

Figure 4.2: AFM image of aluminum grown on untreated C-plane sapphire has RMS roughness of 2.6 nm.

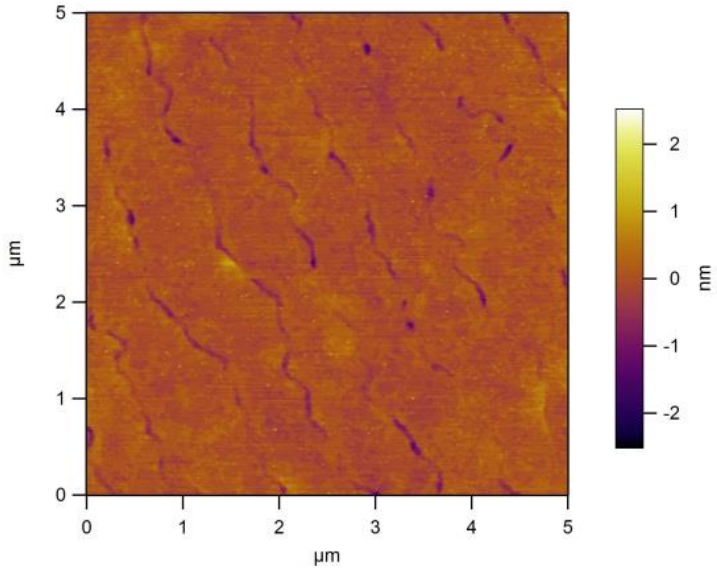

Figure 4.3: AFM image of aluminum film grown on C-plane sapphire that has been oxygen annealed and etched with BOE, has an RMS roughness of 0.2 nm

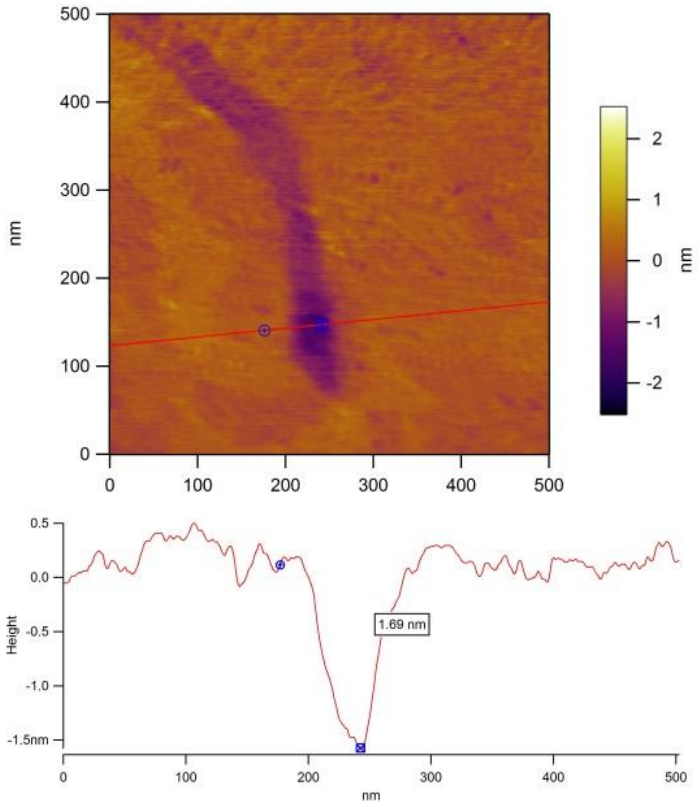

Figure 4.4: Line scan through one of the striations on aluminum film shows it to be 1.7 nm deep

In addition to AFM, I have also done a radial x-ray diffraction (XRD) scan of the aluminum film grown on c plane sapphire. The XRD was performed in a Philips X'Pert system, which uses Cu Kα x-rays (λ = 1.5406 Å). The incoming x-rays make an angle ω with the surface of the film, and the detector is placed at angle 2θ to the incoming x-rays. The radial scan, also known as a longitudinal scan or a 2θ-ω scan, varies both the detector and source angles such that ω=2θ. The x-rays diffract off of the crystallographic planes of the film and the substrate following Braggs Law nλ=2dsinθ, where d is the spacing of the crystallographic plane. In Figure 4.5 which shows this scan, one can see the peaks of the substrate and the aluminum (111) film

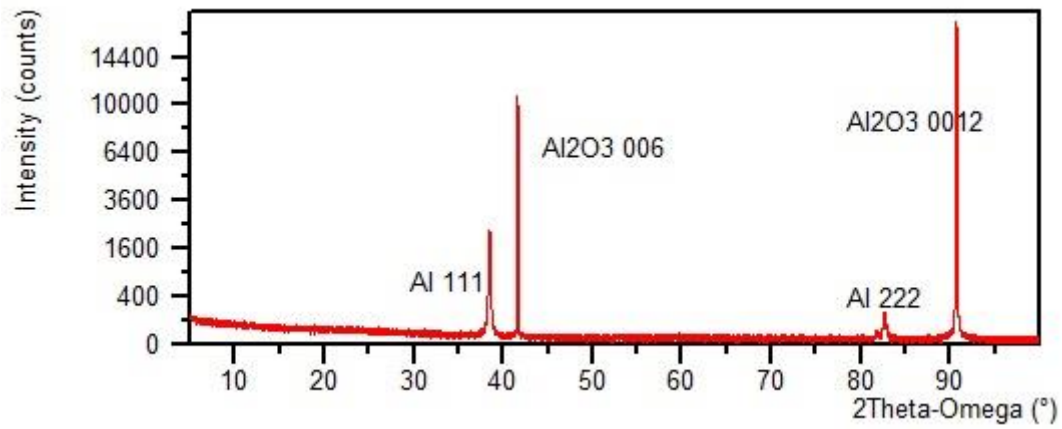

Figure 4.5: XRD for aluminum film shows peaks for c-plane sapphire, and 111 aluminum

4.2 Qubit Fabrication

After studying the growth of aluminum films, I moved on to fabricating Josephson junctions using the shadowmask evaporation technique. Also known as double angle evaporation, this process requires a single lithography step. Additionally, this process is additive rather than subtractive which means it is easily capable of producing junctions of .01 μm^2. Shadowmask junctions are created by using a photoresist mask like the one shown in Figure 4.6 which has a 2 layer resist structure with the bottom layer undercut from the top layer. The top layer of photoresist forms a suspended bridge over a section of bare substrate, which is known as a Dolan bridge after G. J. Dolan who developed the shadowmask process [59]. In order to form the junction, aluminum is first deposited at an angle to the normal of the substrate as shown in Figure 4.7 A. This forms the base electrode of the junction. The surface of the aluminum is then oxidized to form a tunnel barrier. After this aluminum is deposited at the opposite angle, forming the counter electrode, as shown in Figure 4.7 B. The junction is formed by the small region of overlap under the photoresist bridge. The junctions on either side are of much larger area (essentially infinite) and so act as superconductors rather than Josephson junctions. After deposition the photoresist is dissolved, removing with it any aluminum deposited on top of it.

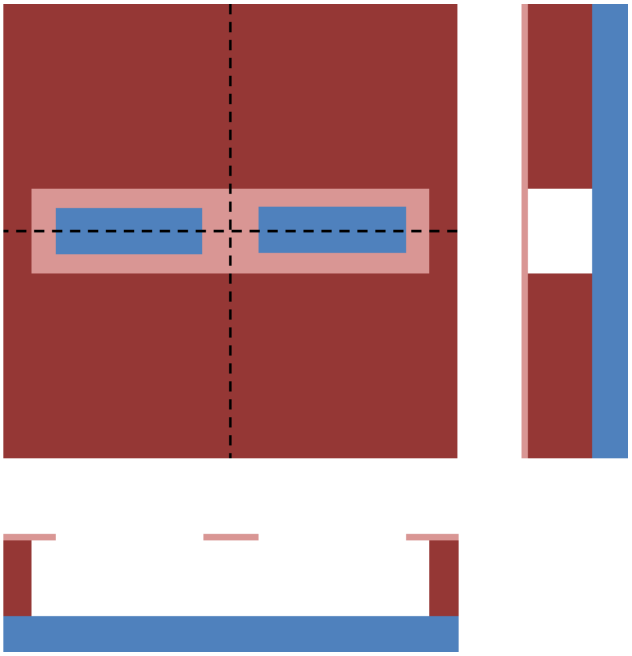

Figure 4.6: Top down and cross sectional views of photoresist pattern for shadowmask junctions

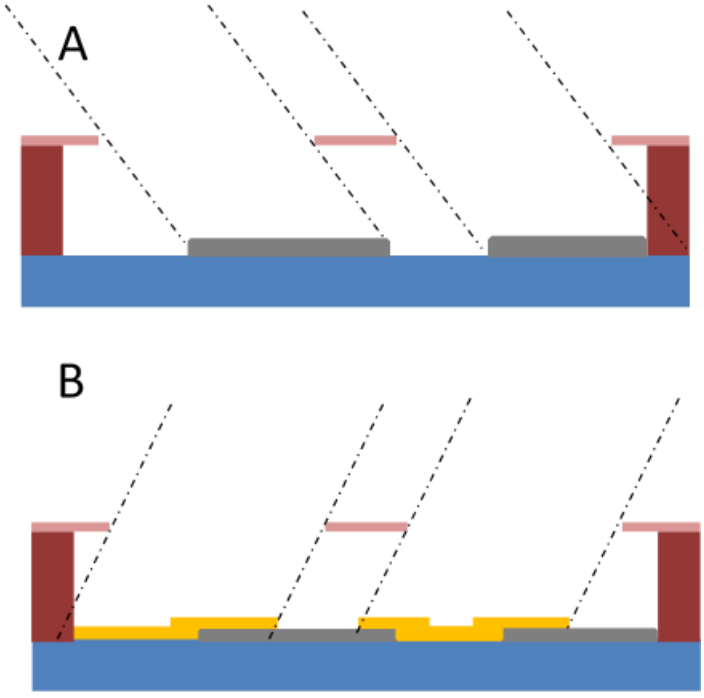

Figure 4.7: Aluminum deposition for Shadowmask Junctions

Figure 4.8 shows a typical junction fabricated using the shadowmask technique. The qubits fabricated in this section were designed as shown in Figure 4.9. The capacitor paddles were each 250 microns wide and 500 microns tall; they were separated by a distance of 25 microns. This arrangement has a capacitance of about 65 femtofarads. Remembering that $E_c = \frac{e^2}{2C}$, this gives us an E_C of $1.97*10^{-25}$ joules. The junctions in these transmons had an area of 0.75*0.4 = 0.3 square microns. The barrier in these junctions is grown such that the critical current is about 22 nA. Remembering that $E_j = \frac{\hbar I_c}{2e}$, this gives us E_j=$7.2*10^{-24}$ joules. The energy spacing can then be calculated: $E_{01} = \sqrt{8E_cE_J}$ = $3.4*10^{-24}$ joules. This corresponds to a frequency $f_{01}=E_{01}/h$=5.1 GHz. Actual qubits varied between 4.9 and 5.6 GHz due to unintended variation in the critical current of the junctions.

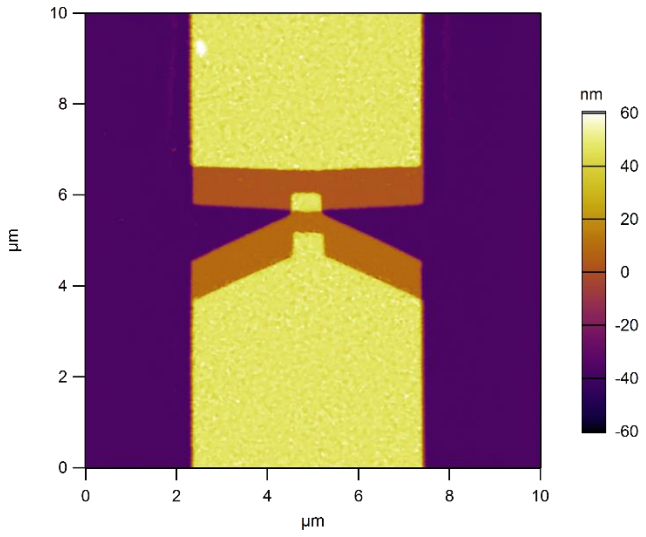

Figure 4.8: AFM image of Josephson junction made by shadowmask technique.

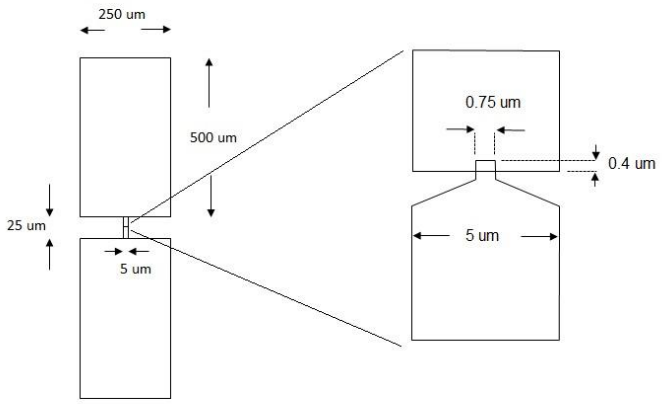

Figure 4.9: Design of 3D transmons fabricated in this section.

4.2.1 Substrate Preparation and Lithography

The first step to fabricating shadowmask junctions and transmons is to prepare the substrate. This is similar to the substrate prep that was done for the aluminum films. As with the aluminum films, the substrate first goes through ultrasonic cleaning in solvents, then goes through the oxygen anneal, and the second ultrasonic cleaning. However, the BOE etch is held off until after lithography.

After cleaning the substrate needs to be prepped for lithography. First it is baked on a hotplate at 200 °C to remove any water from the surface. Next MicroChem (8.5) MMA EL-13 copolymer is spun on at 2000 RPM, this copolymer is more viscous than the EL-9 used for the wireup step of the niobium trilayer junctions, and so spins on thicker. Next the substrate is baked at 200 °C for 3 minutes to evaporate the solvents from the MMA. ZEP 520 A7 resist is then spun on at 2000 RPM, and it is baked for 10 minutes at 2000°C. Finally, aquaSAVE is spun on at 1500 RPM and the substrate is baked for 5 minutes at 70°C.

ZEP is a high performance e-beam resist made by Zeon chemicals [60] that has high resolution and a high resistance to dry etching. The importance of the resistance to dry etching for the present application will be discussed in the following section. Another property of ZEP

that is important for making shadowmask junctions is that it is developed by n-amyl acetate and not by MIBK. Whereas the MMA underlayer is developed by MIBK and not n-amyl acetate. This allows the two layers to be developed using different temperatures and times which allows for the undercut to be controlled ZEP 520 A7 has a molecular weight of 57000 and a viscosity of 7 mPa·s and uses anisole as its solvent. At 2000 RPM it spins on at a thickness of 3000 Å.

After the resist is prepared the sample is loaded into the e-beam lithography system. The e-beam is set to a voltage of 20 kV, with a 10 micron aperture, which gives a beam current of about 0.04 nA. The electron beam is then focused and the stigmation and aperture alignment are corrected. The coordinate system of the pattern is aligned such that the X-axis is aligned with the bottom edge of the substrate, and the origin in the bottom left corner. A recognizable speck of dust if found and its location noted. The features near the junction are written with an exposure dose of 160 $\mu C/cm^2$.

Next the aperture is increased to 120 microns, which increases the beam current to about 5 nA. This is necessary to write the capacitor paddles, which due to their large size would take a prohibitively long time to expose at a lower beam current. The change in aperture introduces a shift in the beam. This is corrected by locating the speck of dust found earlier and shifting the coordinate system so that it is at the same location as with the 10 micron aperture. After adjusting the aperture, the writefield size is increases to 1000 microns. This allows the capacitor paddles to be written with no stitching necessary. The paddles are then written with an exposure dose of 200 $\mu C/cm^2$. It has been found that this larger exposure dose is necessary for the large features to develop out fully, however a dose this large would cause the small features to be overexposed.

After lithography the resist needs to be developed. The first step is to remove the aquaSAVE by rinsing in water for 60 seconds. Next the ZEP is developed using n-amyl acetate in an ice bath (which gives a temperature of 2 °C) for 60 seconds. The development is stopped by rinsing with IPA and blowing dry with nitrogen. Next the MMA layer is developed in 1:3 IPA:MIBK for 140 seconds at room temperature. This long development gives a large undercut and ensures that the Dolan bridge is fully suspended. Figure 4.10 shows a micrograph of the developed

photoresist. The gray regions are the bare substrate, the greenish gray regions are the MMA-ZEP bilayer resist, and the light regions are suspended ZEP.

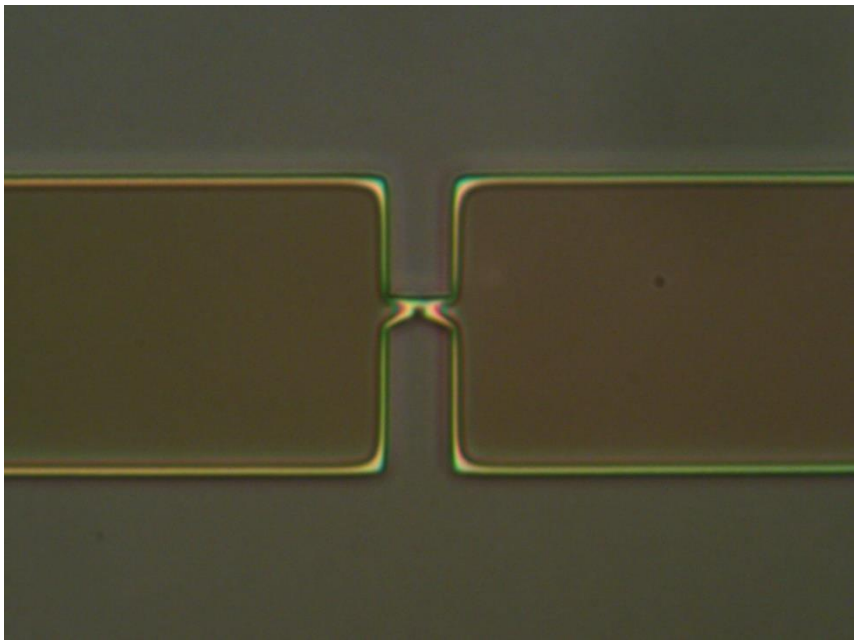

Figure 4.10: Lithography for shadowmask junctions.

4.2.2 Removing residue from developed areas

Once the substrate has been developed, there will be some remaining residue in regions that should be bare substrate. This is shown by the white dots on the left side of Figure 4.11. This residue would interfere with the epitaxy of the base electrode layer. The residue would act as a source of TLS's, which would lead to loss and decoherence of the transmons. To remove this residue an oxygen plasma clean can be used. This cleaning process is outlined below.

After the photoresist is developed the substrate is loaded into the RIE and allowed to pump for 5 minutes. Then the oxygen ash recipe is run. After the oxygen ash, the sample is dipped in BOE for thirty seconds, to prepare the surface of the substrate for growth, as for the aluminum films discussed in section 4.1. The BOE dip has been held off until this point so that it is the last thing done to the sample before it is mounted on a substrate holder and loaded into the vacuum system. The right side of Figure 4.11, shows the surface of the substrate after a 30 second oxygen ash and a 30 second BOE dip. The photoresist residue has been removed.

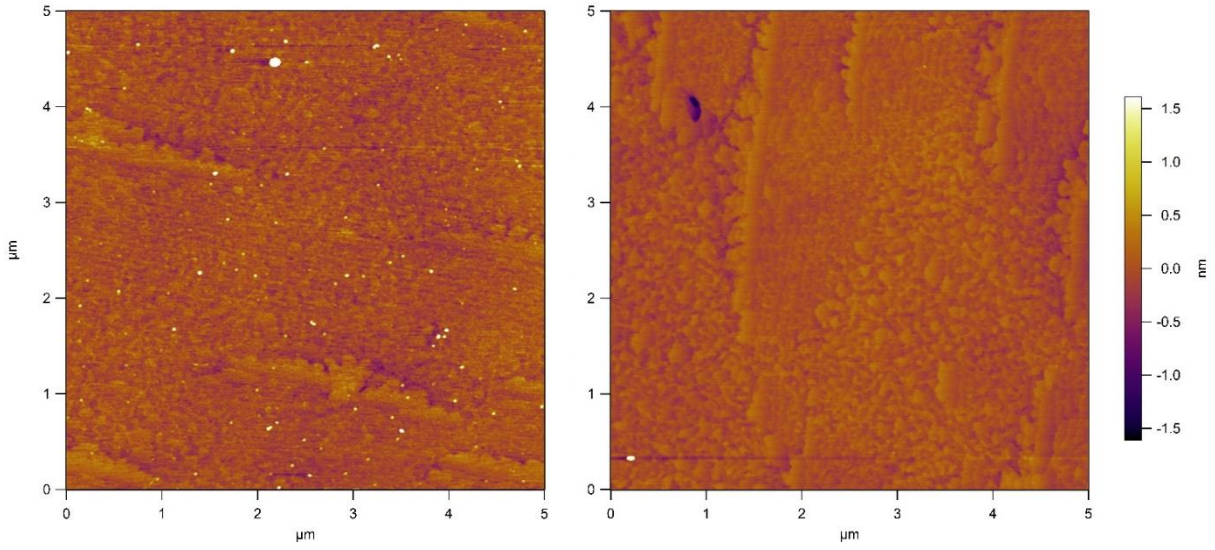

Figure 4.11: Left: developed out regions of the substrate still have photoresist residue which appear as white dots. Right: A 30 second oxygen ash and a 30 second BOE dip removes this.

As mentioned earlier, PMMA—which was the original photoresist that we planned to use for the shadowmask junctions—does not have much resistance to plasma etches. Figure 4.12 shows a before and after picture of a PMMA-MMA bilayer patterned to form a junction. On the left image the green color is the bilayer, the dark yellow is exposed substrate, and the lighter yellow is suspended PMMA, forming the Dolan bridge. On the right image, the darker yellow is the PMMA-MMA bilayer, this color change is due to the oxygen plasma clean thinning out the PMMA. The lighter yellow is the exposed substrate. The suspended PMMA Dolan bridge is completely gone. It is for this reason that I switched to using ZEP resist.

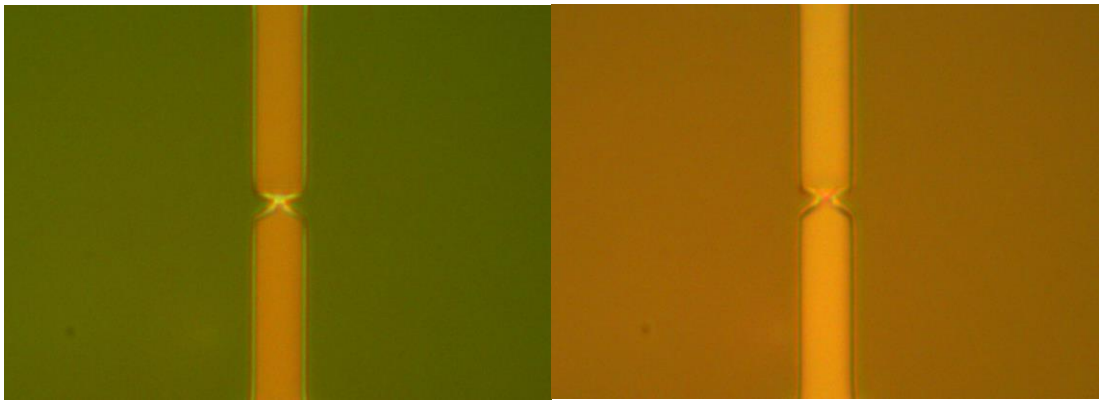

Figure 4.12: Oxygen plasma clean destroys Dolan bridge made of PMMA. Left before oxygen plasma clean. Right: After oxygen plasma clean.

I studied the effect of the oxygen ash time on the subsequent growth of the aluminum. Figure 4.13 shows AFM images of the base electrode grown on samples that had a 30 second ash, a 60 second ash and a 120 second ash. The aluminum on the substrate with the 30 second ash had a roughness of 539 pm; the one with the 60 second ash had a roughness of 437 pm and the one with the 120 second ash had a roughness of 429 pm. Although the ZEP is more resistant to the oxygen ash, it is not completely resistant. The ash has the effect of expanding the features and rounding out the corners due to the eroding of the edges. While junctions with a 30 second ash had an area of 0.30 square microns, the junctions with the 60 and 120 second ashes had areas of 0.37 and 0.40 square microns, respectively. Because of this degrading of the lithographic pattern it was decided to restrict the oxygen ash to 30 seconds.

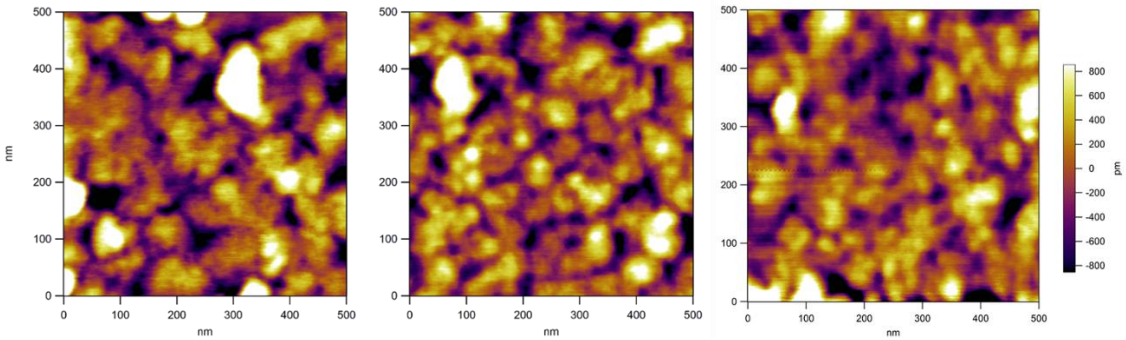

Figure 4.13: Effect of oxygen plasma clean on aluminum growth. Left: Sample with 30 second oxygen plasma clean has RMS rougness of 539 pm. Center: Sample with 60 second oxygen plasma clean has RMS roughness of 437 pm. Right: Sample with 120 second oxygen plasma clean has RMS roughness of 429 pm.

4.2.3 Deposition Process

After the patterned substrate is prepared, it is mounted on a substrate holder and loaded into the transfer tube. It is left in the transfer tube overnight to outgas. This outgassing must be done at room temperature because it was found that outgassing at elevated temperatures caused the Dolan bridge to crack, which created a shorted junction, as shown in Figure 4.14. The next morning the substrate is moved into the deposition chamber; at this point it has been outgassed sufficiently that the introduction of the photoresist covered substrate does not increase the pressure in the chamber by more than 10^{-11} Torr. The cryo panels are then cooled, and substrate is then rotated such that aluminum cell is angled correctly to deposit the base electrode. And the mask is put in place.

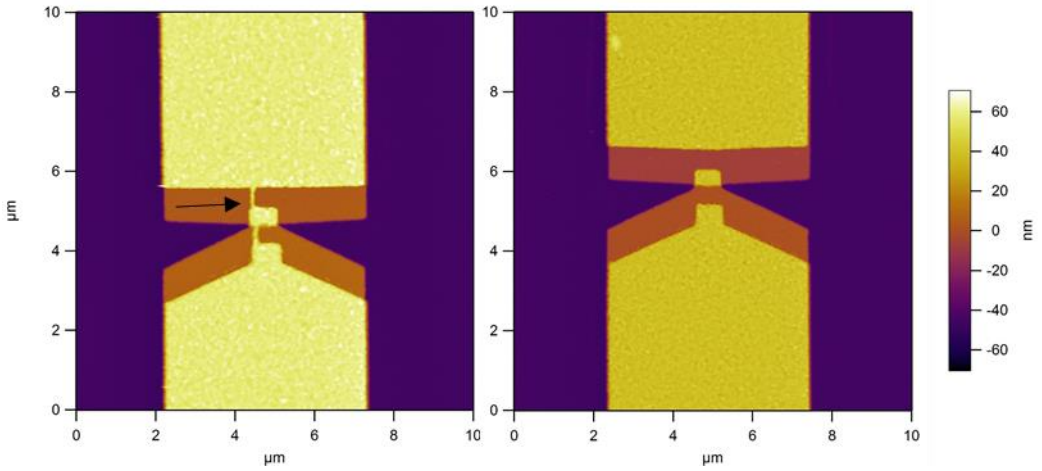

Figure 4.14: Left: outgassing at an elevated temperature causes the Dolan bridge to crack, shorting the junction. Right, a good junction with no crack.

The aluminum cell is then ramped up to 1125 °C over the course of 15 minutes. Once the cell reaches temperature, the shutter is opened and the deposition rate is allowed to stabilize for 5 minutes. The substrate mask is then removed and the deposition begins. The aluminum growth is crystalline due to the careful substrate preparation, however it is not as good a crystal as the aluminum films discussed above, due to the fact that this growth happens at room temperature. The base electrode is grown to a thickness of 450 Å, which takes 625 seconds in system E and 750 seconds in system F, and then the growth is stopped with the aluminum shutter and the aluminum cell is ramped down to an idle temperature of 800°C.

After the growth of the base electrode the barrier is grown. I have made transmons with two kinds of barriers, the first is a standard diffused barrier. After the base electrode is grown, the sample is transferred to the oxidation chamber. The oxidation chamber is filled with a mixture of 10% oxygen and 90% argon, to a desired pressure from 1 to 100 Torr. The oxygen is allowed to react with the aluminum surface for the desired amount of time. The thickness of the oxide barrier is controlled by the oxygen exposure dose which is the product of the partial pressure of oxygen and the exposure time. The critical current density of the junctions is plotted against the oxygen exposure dose in Figure 4.15. The transmons I have made had an exposure dosage of 7000 Torr-seconds, which gives a critical current density of about 70 nA/μm^2, which given that the junctions are of area 0.3 square microns brings the critical current to 21 nA. After the oxygen exposure the oxygen is pumped out, and the chamber is pumped with a cryopump for 30 minutes to allow the pressure to drop low enough to transfer into the tube. The sample is then returned to the growth chamber for the counter electrode deposition.

The other kind of barrier is a co-deposited oxide. Films incorporating these barriers are only grown in system E. When I am making a film with a co-deposited barrier I start by growing the base electrode to a thickness of only 420 Å and the mask is put in place. Then the aluminum cell is ramped down over 15 minutes to a temperature of 800 °C and held there for 5 minutes. Next the aluminum cell is ramped up to 1020 °C in 15 minutes. The aluminum shutter is opened and the aluminum deposition rate is allowed to stabilize for 5 minutes. This procedure of ramping the temperature down and then back up is used because the deposition rate was found to be hysteretic, and this procedure gives a repeatable deposition rate of 0.1 Å/s. Then the substrate mask is removed and the remaining 30 Å of the counter electrode is grown. Then the mask is put in place, and the oxygen injector is used to bring the chamber pressure up to $5x10^{-6}$ Torr of oxygen, with the aluminum cell still hot and the shutter opened. The mask in then removed and aluminum oxide is grown for the desired thickness. I have found that to get a critical current density of 70 nA/μm^2, which is used for the transmons, a growth time of 42 seconds is required. The growth is then stopped by closing the aluminum shutter, and the aluminum cell is ramped down to 800 °C. Oxygen is still injected into the system for 60 seconds after the aluminum is stopped. After the oxygen is turned off the chamber is allowed to pump back down to about 10^{-}

^{9} Torr, which takes approximately 45 minutes. Then the substrate is moved to the oxidation chamber, where it is exposed to oxygen using the procedure described above, for an exposure dose of 2500 Torr-seconds. This is to fill in any oxygen vacancies from the deposition process, and also to ensure that the side of the base electrode is oxidized, so that the counter electrode does not short to the base electrode at the edge of the overlap. The oxidation chamber is then pumped out and the sample is returned to the deposition chamber for the counter electrode deposition.

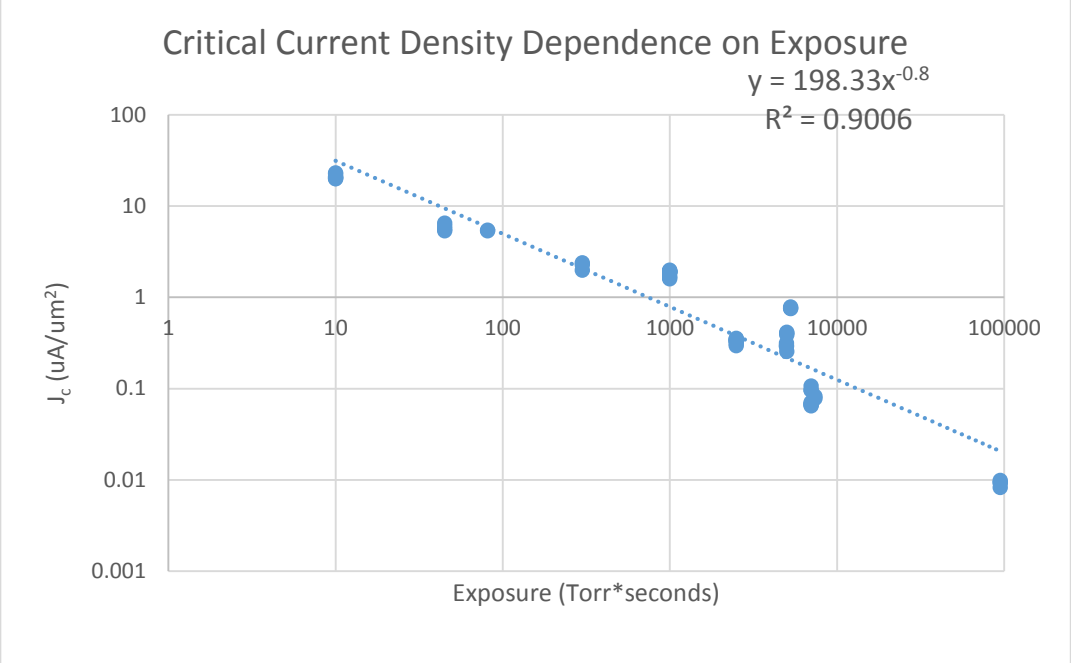

Figure 4.15: Josephson junction critical current density dependence on oxygen exposure dose for diffused barriers.

Once the sample is back in the chamber, it is rotated 180° from the position it was in for the base electrode deposition. The mask is then put in place, and the aluminum cell is ramped up to 1125 °C over 15 minutes. The shutter is opened and the deposition rate is stabilized for 5 minutes. Then, the substrate mask is removed and the aluminum is deposited for the desired thickness, in the case of the transmons I grew, the thickness was 450 Å. The counter electrode layer is polycrystalline, since it is grown on top of the barrier layer, which is amorphous. The growth is stopped with the aluminum shutter, and the aluminum cell is ramped down to its idle temperature of 800°C.

At this point, the cladding layer (if any) is grown. For details on the various cladding layers and their method of growth see section 4.3

The sample is then removed from the vacuum system via the load lock. It is removed from the substrate holder and soaked in acetone overnight to dissolve the photoresist and lift off the aluminum. Then next morning, it is sprayed with acetone to break up the, now unsupported aluminum above where the photoresist used to be, and to rinse it away. The acetone is rinsed away with IPA and the sample is blown dry with nitrogen. Care must be taken to spray very gently with nitrogen, if the nitrogen is blown too hard, it will ionize when traveling through the plastic hose and charge the capacitor paddles on the transmon which will cause a static discharge, ruining the junction.

The substrate now needs to be diced so that each transmon is on an individual chip. This is done using a diamond saw, but first the sample is coated in photoresist to protect the transmons from being covered in dicing debris (sapphire dust from the substrate, and debris from the blade being worn down). To prepare the sample for dicing it is baked at 150 °C for 3 minutes. Then MMA EL-9 is spun on at 2000 RPM, and it is baked at 150 °C for 5 minutes. Next AZ 5214 photoresist is spun on at 4500 RPM and baked at 150 °C for 5 minutes. The AZ 5215 is used because it is physically stronger than PMMA, and thus stands up better to the dicing. At this point the sample is diced. The photoresist and dicing debris is removed by first soaking in MicroChem Remover PG at 80 °C for 30 minutes, and then soaking in acetone overnight.

4.3 Cladding Layer

In this section I will discuss the various cladding layers I have made for transmons. The point of these layers is to provide a higher quality dielectric at the superconductor-vacuum interface than the native oxide formed by air reacting with aluminum.

The first type of device made was a control device, with no cladding layer. It was removed from vacuum immediately after the counter electrode was grown, a native oxide was formed on the surface from exposure to air. Next a diffusive oxide was formed in situ by exposure to UHP

oxygen. Then aluminum nitride cladding layers were made, first by nitridizing the top of the counter electrode with nitrogen plasma, followed by the growth of aluminum nitride by depositing aluminum in a nitrogen plasma environment.

4.3.1 In Situ Diffusive Aluminum oxide

The first cladding layer that I studied is in situ diffusive aluminum oxide. The idea is that since air contains not just oxygen, but also water, carbon dioxide and hydrocarbons, there should be more defects in the native oxide formed in air as compared to those formed by oxidation in UHP oxygen. One such defect is hydroxide groups, which have a magnetic moment and can act as TLS's reducing the coherence time.

For this cladding layer, after the counter electrode was grown, the sample was moved to the oxidation chamber, which was filled to about 60 Torr (actual 63.75) with 10% UHP oxygen in 90% argon. It was left to expose for 19 hours, which gives it an oxygen exposure dose of 2.066×10^{7} Torr-seconds. This should be sufficient to fully passivate the surface.

4.3.2 Co-Deposited Aluminum Oxide

The next cladding layer studied is co-deposited aluminum oxide, grown the same way as the co-deposited barriers. This should have less oxygen vacancies than a diffusive oxide—either from air or UHP oxygen—and thus have fewer TLS's and a longer coherence time.

After the counter electrode layer was grown, the aluminum cell was ramped down to 800 °C in 15 minutes, it was left there for 5 minutes and then ramped up to 1020 °in 10 minutes. The mask was put in place and the aluminum shutter was opened and the rate was allowed to stabilize for 5 minutes. Then the oxygen injector was used to bring the chamber pressure up to 5×10^{-6} Torr. The mask was pulled back and the aluminum oxide was grown for 60 seconds while the substrate was continuously rotated to ensure that no part of the surface was shadowed by the photoresist. This should be sufficient time to grow approximately 10 Å of aluminum oxide. The growth was then stopped with the aluminum shutter and the aluminum cell ramped down to its idle temperature of 800°C; the oxygen was injected for 60 seconds after the aluminum was stopped. After the oxygen was stopped, the chamber was pumped back down to approximately 10^{-9} Torr, which takes approximately 45 minutes, and the substrate is transferred to the oxidation

chamber where it is exposed to an oxidation dose of 7000 Torr-seconds to fill in any oxygen vacancies from the growth.

4.3.3 Diffusive Aluminum Nitride

The next surface cladding layer that I studied was diffusive aluminum nitride. This was done by exposing the surface of the counter electrode to nitrogen plasma in situ. The idea is to nitridize the surface enough to passivate it against oxidation, but to have a layer of aluminum nitride no thicker than necessary. Once the counter electrode is grown the sample is rotated such that the plasma source makes the same angle with the substrate that the aluminum did for the counter electrode growth, and then the MBE system substrate mask is put in place.

The first step to starting the plasma source is to purge the nitrogen line at 3 Torr for 10 minutes. Then the plasma source power supply was turned on and the RF power was ramped up to 60 W, and the RF matching unit was adjusted so that there was no reflected power. Next the precision leak valve was opened enough to allow enough nitrogen into the chamber to bring the chamber pressure to $8x10^{-6}$ Torr. The RF power was ramped up, while adjusting the RF matching network to keep the reflected power below 10 W, until a low brightness plasma is struck (around 200 W). Then the precision leak valve is adjusted to reduce the chamber pressure to $5x10^{-6}$ Torr, which causes the plasma to switch to high brightness mode. The plasma RF power is ramped up to 300 W, and the matching unit is adjusted to bring the reflected power to zero.

Once the plasma source is ready, the mask is removed from the substrate and the surface of the counter electrode is exposed to the plasma for 15 minutes, and then the substrate is rotated 90 degrees. This process is repeated until the plasma hits the sample from each of the four directions for 15 minutes, giving a total exposure time of 60 minutes.

Unfortunately, this procedure was not able to successfully create good transmons. Figure 4.16 shows the result of this procedure. The surface of the capacitor paddle appears to be covered in a strange residue. I tried to repeat this process several times, and this happened each time. I believe that the nitrogen plasma was able to work its way into grain boundaries and nitridize aluminum deeper into the counter electrode layer rather than just at the surface.

Because the aluminum nitride is larger than the original aluminum it expands and delaminates, causing the effect shown in Figure 4.16.

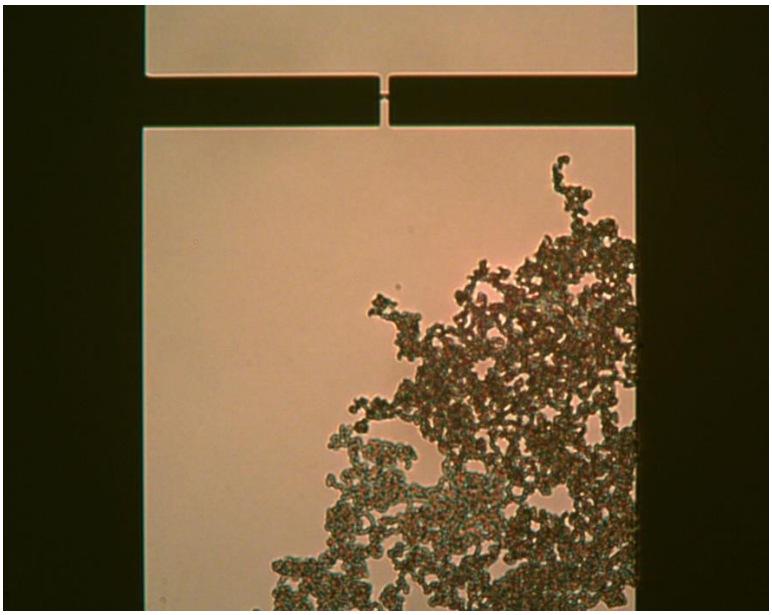

Figure 4.16: Diffusive nitridization causes strange growth on surface of capacitor paddles.

4.3.4 Co-Deposited Aluminum Nitride

The final cladding layer I studied is co-deposited aluminum nitride. Because each layer is nitridized as it is deposited rather than, needing nitrogen to diffuse in, it should need much less exposure to nitrogen plasma than the diffusive aluminum nitride, and so shouldn't be susceptible to the same problem caused by the long nitrogen exposure.

To grow this layer, once the counter electrode layer is finished, the aluminum cell is ramped down to 800 °C in 15 minutes, held for 5 minutes and then ramped up to 1020 °C in 10 minutes. The mask is put in place and the aluminum shutter is opened and the deposition rate is stabilized for 5 minutes. While the aluminum cell is stabilizing, the nitrogen plasma source is started using the procedure in section 4.3.3 to get a plasma in high brightness mode with a power of 300 W and a pressure of 5×10^{-6} Torr. The mask is then removed and the aluminum nitride is grown for 15 seconds at the same position as it was in for the counter electrode growth and then for 45 seconds while rotation continuously, for a total of 60 seconds. The growth is stopped with the aluminum shutter, and the sample is continued to be exposed to the nitrogen plasma for

another 60 seconds, and then the RF power is turned off to stop the plasma, and the precision leak valve is closed, stopping the flow of nitrogen.

Chapter 5 Testing results

In this section, I will discuss the testing results and the effects of the different cladding layers on the coherence of the qubits. I will begin by discussing room temperature DC measurements that were performed to ensure that the qubits were working properly before the more extensive RF measurements were performed. These DC measurements had to be performed carefully to prevent damage to the devices, which are very sensitive to electrostatic discharge. Next, I will discuss the technique used to measure the qubits. Rabi oscillations, T1 measurements, Ramsey fringes and spin echo measurements, which were discussed in section 2.3.2, all require measuring the state of the qubit, which is done by measuring how the interaction of the qubit affects the transmission of the cavity. Finally I will present measurement results. These measurements were kindly performed by Jaseung Ku of the Bezryadin research group. It was found that the qubit with in situ oxidation had increased coherence, while the qubit with the grown oxide cladding did not. The qubit with the aluminum nitride cladding at first behaved unexpectedly, however it turned out to be caused by a problem in measurement. After solving this problem, the aluminum nitride clad qubit showed a similar increase in T_1 as caused by in situ oxidation, however T_2 remained similar to that of the control qubit.

5.1 DC Measurements

Because the qubits are measured in a dilution refrigerator, the cooling down of which is both time consuming and expensive (due to the use of liquid helium), the resistance of the junctions is measured first, in order to ensure that the qubit works and has a critical current in the correct range. Because the junctions in these devices are small and have a low critical current, they are very sensitive to being damaged due to electrostatic discharge, so great care must be taken to perform these measurements without damaging the device.

An air ionizer is used to prevent the buildup of static charge. A grounded writ strap is worn to prevent the buildup of charge on the experimenter. The chip is placed on the probe station, using conductive tweezers. Each of the probes has a one kilo ohm resister and a low pass filter with a cutoff frequency of 1.9 MHz connected in series with it. The device is measured using

a four point measurement. Current was supplied by the use of a function generator, outputting a triangle wave at a frequency of 1 Hz. Current was measured, by connecting a 10 kilo ohm resistor in series with the device, and measuring the voltage across it. The voltage across both the device and the current sensing resistor were measured using a low noise preamplifier connected to a DAQ board. Before placing the probes on the device the leads were all shorted together. They were not connected to ground, because the ground in the lab was noisy enough to damage the junction. After the probes are placed on the capacitor paddles, the leads are unshorted. The voltage is turned on and the resistance of the junction is measured. The voltage is then stopped and the leads shorted again and the probes removed. Successful junctions have a resistance of about 8 kilo ohms.

5.2 RF Measurements

The measurements presented in this section were performed by Jaseung Ku, in the Bezryadin research group. I will first discuss how he measured the state of the qubit. Then I will present the data he collected and discuss the results.

5.2.1 Measurement Technique

. To measure the transmons, they are put into a 3D copper cavity and cooled in a dilution refridgerator. Microwave signals are sent into the cavity and the transmission is measured. Figure 5.1 shows the transmission amplitude vs frequency in the region near the qubit transition frequency. There is a peak at the qubit freqency that broadens with increasing power. At the higest power, a second peak at about 5.2 GHz appears; this is a two photon excitation to the second excited state of the qubit. It is shifted from the peak at the qubit frequency due to the anharmonicity of the qubit.

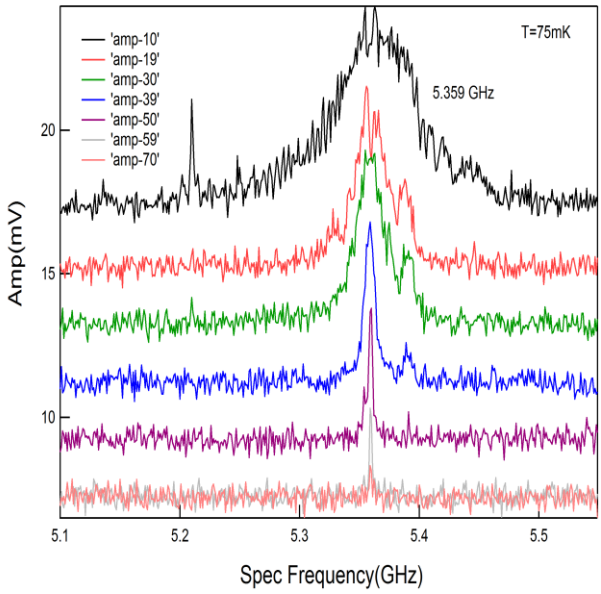

Figure 5.1: Spectrum of qubit transition at various microwave powers.

In order to make time domain measurements, the state of the qubit needs to be mseaured. The state of the qubit is measured using a circuit QED architecture [61]. A disperssive readout can be used. The state of the qubit shifts the resonance of the cavity as shown in Figure 5.2. To measure the state of the qubit, a pulse is sent in at frequency (for instance) $\omega_r - g^2/\Delta$ and the transmission is measured. A high transmission implies that the qubit is in the up state whereas a low transmission inplies the qubit is in the down state.

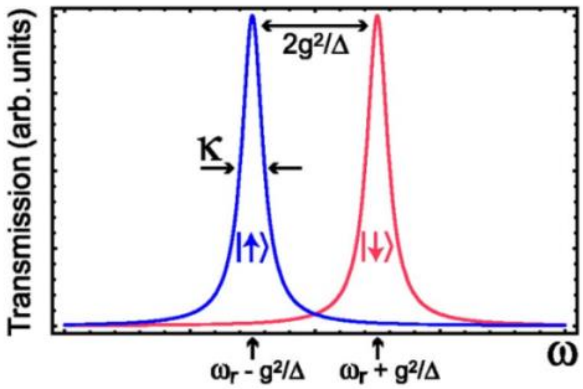

Figure 5.2: Qubit State shifts resonance of the cavity. Image from [61]

Unfortunately, the signal to noise ratio for the dispersive readoutis quite low. However, if the resonator readout power is increased, at a sufficiently high power level, an unexpected "bright mode" of high transmission appears at the bare cavity freqency [62]. The critical power at which this bright mode appears is dependent on the state of the qubit. When the qubit is in the excited state, the bright mode appears at a lower power as illustrated in Figure 5.3. By using this difference in turn on power, one can read out the state of the qubit by using a power such that the bright mode is achieved with the qubit in the excited state, but not with the qubit in the ground state. Figure 5.4 shows the difference in tranmission between the excited state of the qubit and the ground state, by selecteing the readout power that gives the largest difference, one can achiee the highest fidelity measurement.

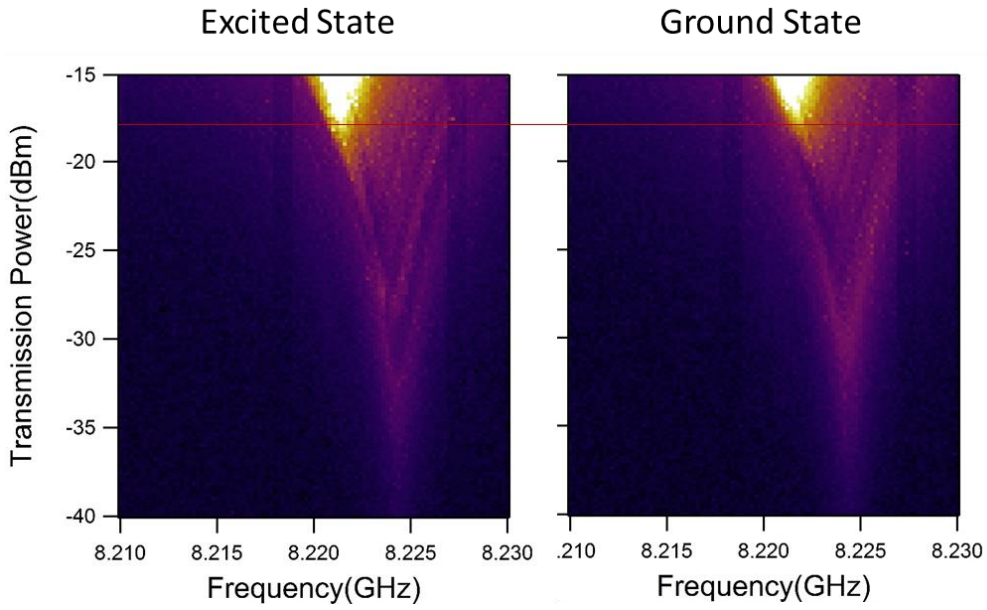

Figure 5.3: Bright state appears at high power. Red line helps illustrate that bright state turns on at lower power when the qubit is in the excited state.

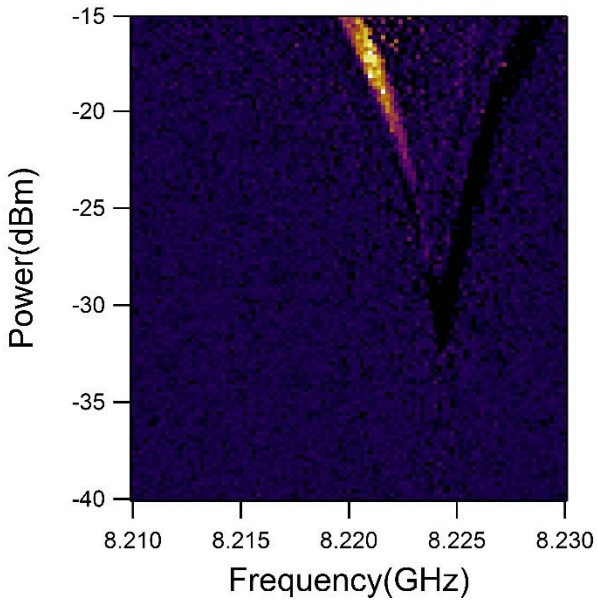

Figure 5.4: Difference in transmission between a qubit in the excited state and a qubit in the ground state.

5.2.2 Results: Control qubit

The control qubit had no surface treatment and was removed from vacuum immediately after the growth of the counter electrode layer. This qubit was found to have a T_1 of approximately 22 microseconds; this measurement is shown in Figure 5.5. Ramsey fringes were measured on this qubit as shown in Figure 5.6, which showed a T2* of 3.4 microseconds. A spin echo measurement shows a slight improvement over T_2*, with a T_2 of 4.2 microseconds. This measurement is shown in Figure 5.7. A second control qubit was measured. It had a T_1 of 26 microseconds, a T_2* of 6.2 microseconds and a T_2 of 6.6 microseconds. The graphs look very similar to those already shown and so are not presented here.

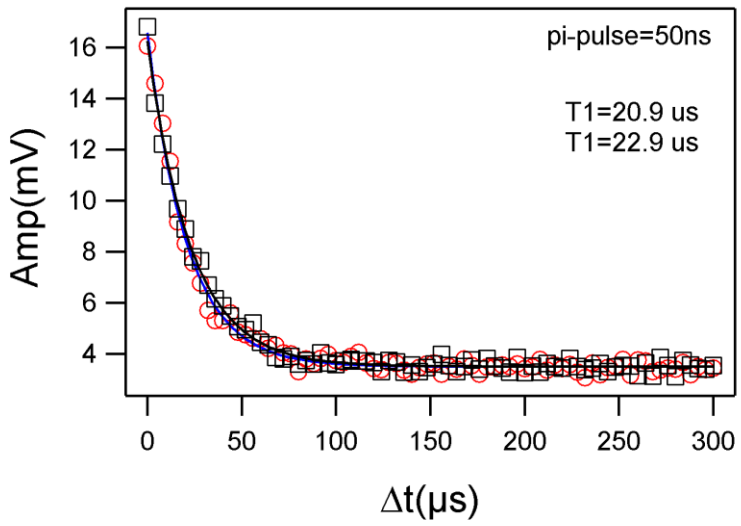

Figure 5.5: T_1 measurement of control qubit shows T_1 of approximately 22 microseconds.

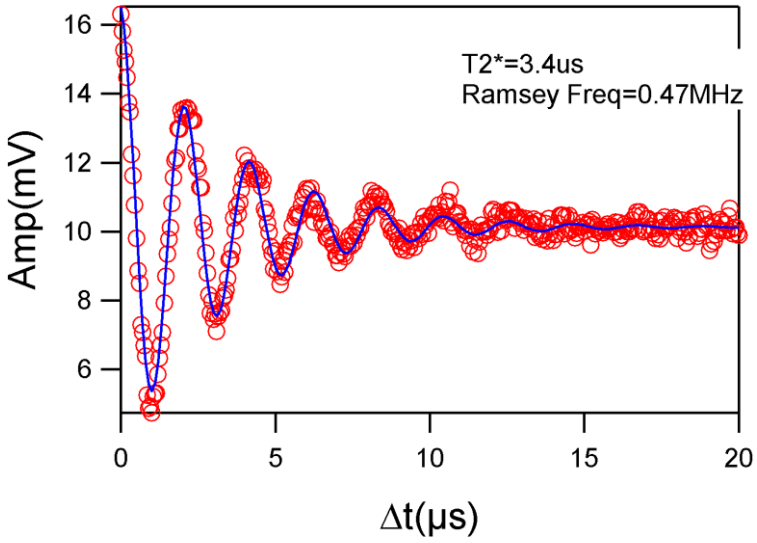

Figure 5.6: Ramsey fringes of control qubit show a T_2 of 3.4 microseconds.*

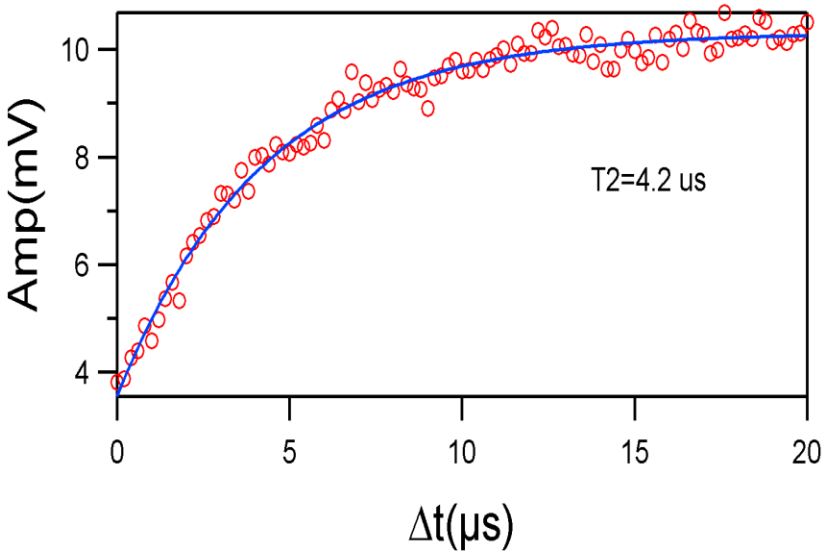

Figure 5.7: Spin echo measurement on control qubit shows T2 of 4.2 microseconds.

5.2.3 Results: In-Situ Oxidation

After the control qubit, a set of transmons was made which had a long in situ oxidation, in order to fully oxidize the surface before it was exposed to air. This qubit had a T_1 of 30.8 microseconds as shown in Figure 5.8. Ramsey fringes, shown in Figure 5.9, showed this qubit to have a T_2* of 7.3 microseconds. A spin echo measurement of this device shows a T2 of 8.3 microseconds. From these results, it is clear that in situ oxidation of the surface of the qubits presents an increase in coherence. The relaxation time (T1) showed a moderate improvement increasing form 22-26 microseconds with the control qubit, to 30 microseconds with this one. The dephasing time (T2) showed larger improvement increasing from 4-6 to 8 microseconds.

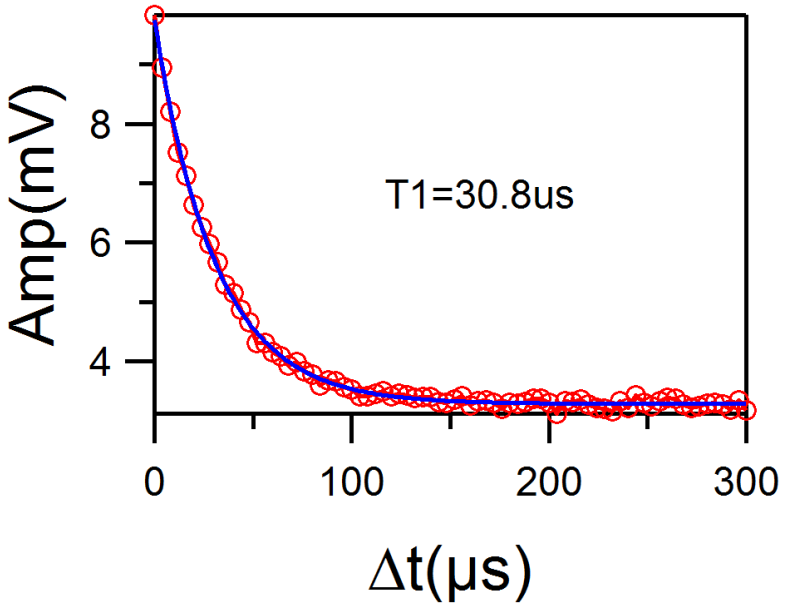

Figure 5.8: T_1 of qubit with in situ diffusive oxidation was 30.8 microseconds.

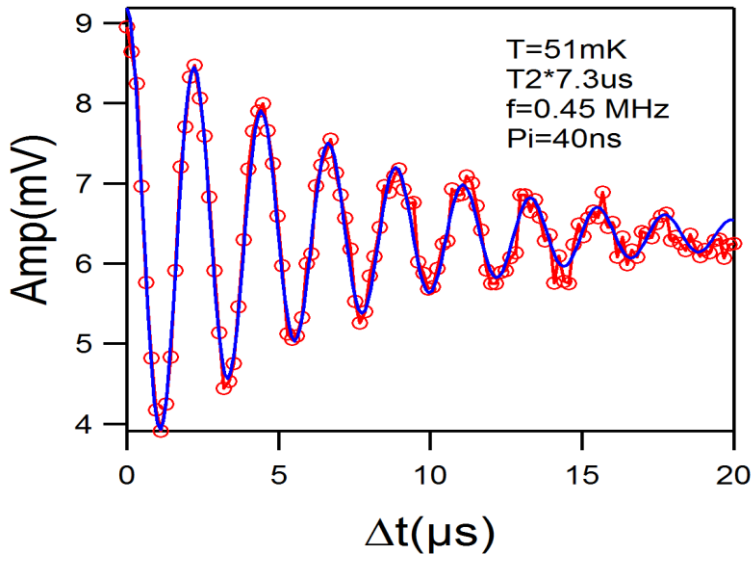

Figure 5.9: Ramsey fringes of qubit with in situ oxidation shows T_2^* = 7.3 microseconds.

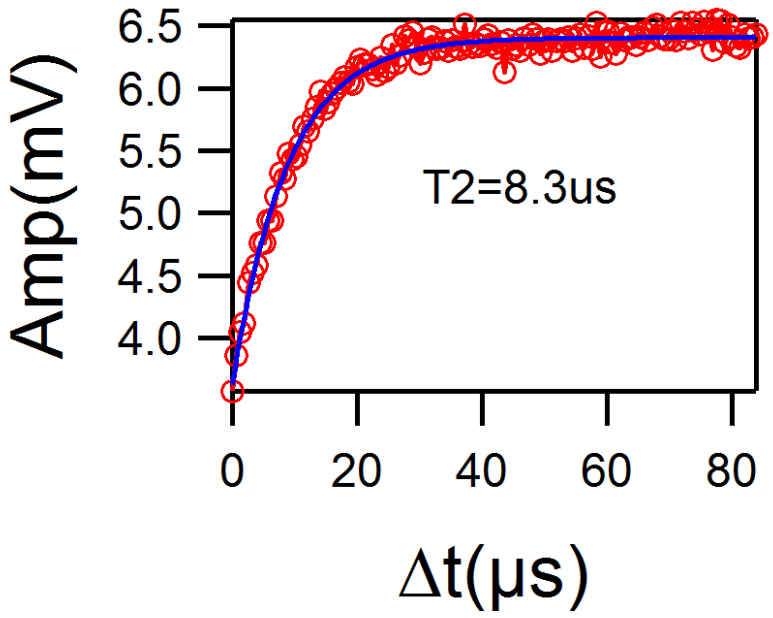

Figure 5.10: Spin echo measurement of qubit with long in situ oxidation gives a T_2 of 8.3 microseconds.

5.2.4 Results: Grown Oxide Cladding

After testing the qubit with the in situ oxidation, a qubit with an aluminum oxide cladding layer was tested. This cladding layer was grown by the co-deposition of aluminum and oxygen on the surface of the qubit. This qubit had a T_1 of 26 microseconds as shown in Figure 5.11. Ramsey fringes of this qubit showed a T_2* of 4.7 microseconds as shown in Figure 5.12. The spin echo measurement shown in Figure 5.13 showed a T_2 of 2.4 microseconds. It should be noted that this T_2 is shorter than T_2*, which should not happen. We repeated this measurement and found the same result. We were unable to discover the source of the suppressed T_2. However give the results of T_1 and T_2* it is clear that the co-deposited oxide cladding does not provide any increase in coherence compared with the control qubit.

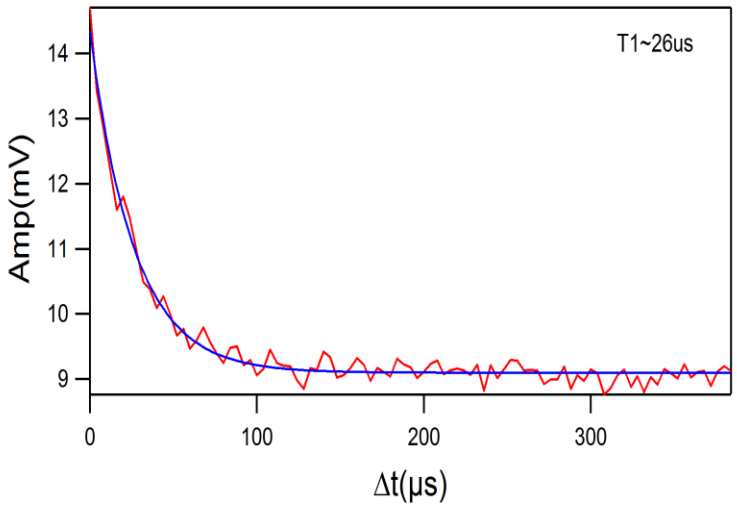

Figure 5.11: Qubit with co-deposited oxide cladding has T_1=26 microseconds.

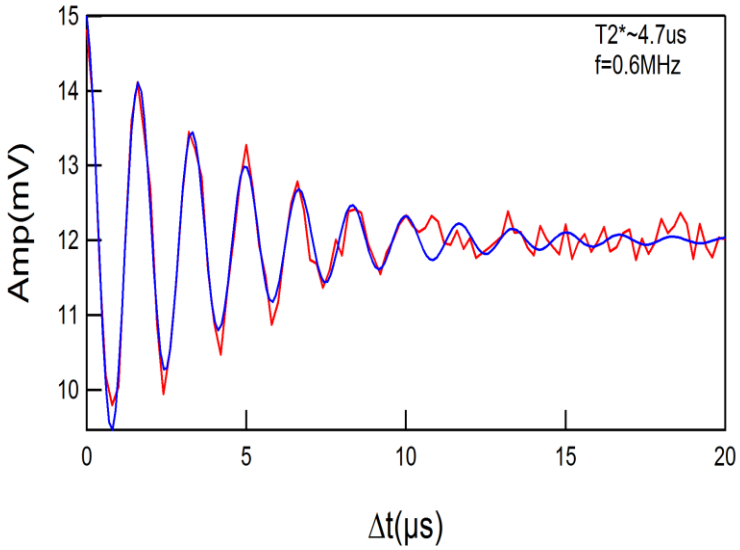

Figure 5.12: Ramsey fringes of qubit with co-deposited aluminum oxide cladding show a T_2 of 4.7 microseconds.*

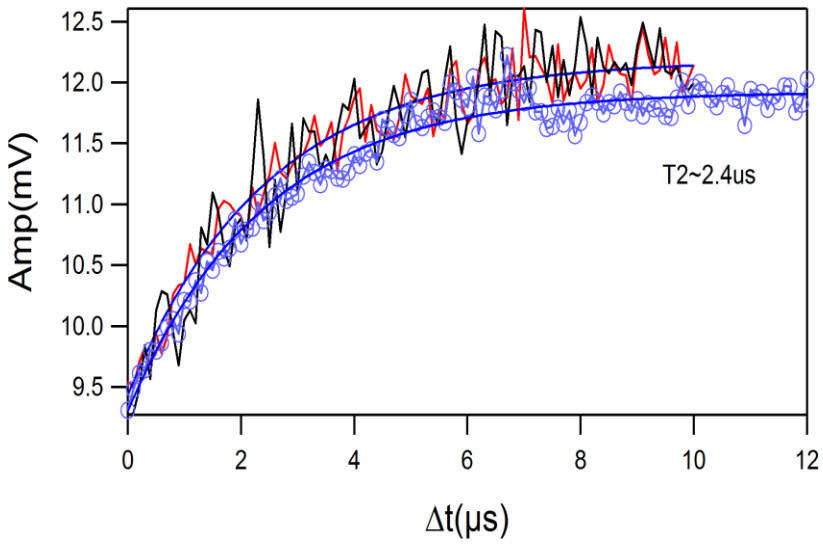

Figure 5.13: Spin echo measurement of qubit with co-deposited aluminum oxide cladding shows a T_2 of 2.4 microseconds.

5.2.5 Results: Aluminum Nitride

Finally, a qubit with an aluminum nitride cladding was tested. This cladding was grown by depositing aluminum in the presence of a nitrogen plasma. This qubit seemed to behave unexpectedly. First it was found that the amplitude of the Rabi oscillations was dependent on the frequency that the qubit was excited at; this is shown in Figure 5.14. This amplitude is suppressed at the qubit frequency f_{01}. Rabi oscillations were taken at different drive frequencies and plotted in a 2D plot as shown in Figure 5.15. Note that the Rabi frequency increases as the drive frequency gets further from the qubit frequency. This is expected and is given by:

$$\Omega = \sqrt{{\Omega_0}^2 - \Delta^2}$$

Where Ω, is the Rabi frequency, Ω_0 is the Rabi frequency at zero detuning, and Δ, is the detuning of the drive frequency f_s

$$\Delta = f_{01} - f_s$$

What is not expected is, the gray line at zero detuning. This is the suppression of the amplitude of the Rabi oscillations at the qubit frequency. Compare this to Figure 5.16, which shows Rabi oscillations at different frequencies for the qubit with the in situ oxidation. This qubit exhibits

the expected shift in the Rabi frequency at non-zero detuning, but the suppressed amplitude at the qubit frequency is absent.

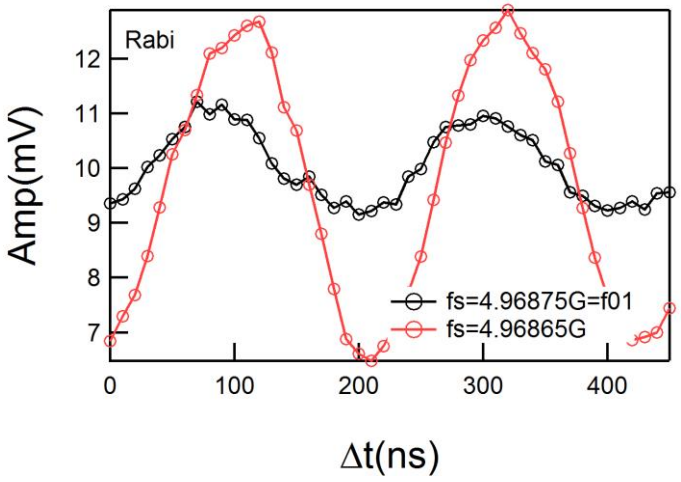

Figure 5.14: Amplitude of the Rabi Oscillations was found to be suppressed at the qubit frequency.

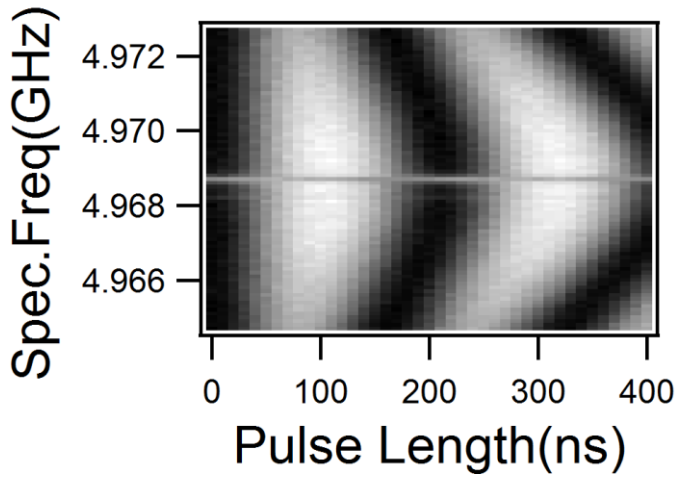

Figure 5.15: Rabi oscillations at different frequencies on the qubit with aluminum nitride.

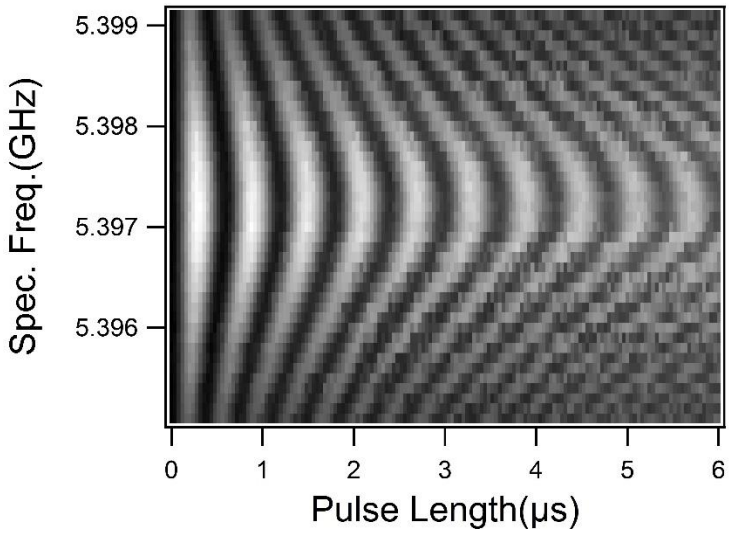

Figure 5.16: Rabi oscillations of qubit without aluminum nitride show no decrease of amplitude at qubit frequency.

After measuring Rabi oscillations on the qubit with the aluminum nitride cladding layer, the relaxation time was measured. Like the Rabi oscillations, T_1 was also dependent on the spectroscopic frequency that was used to excite the qubit. As shown in Figure 5.17, T_1 was suppressed at the qubit frequency, dropping to 3.2 microseconds on resonance, from 23 microseconds off resonance. Once off resonance, the relaxation time does not depend on the, amount of detuning. The other thing to note about this, is on resonance the qubit doesn't seem to decay all the way to the ground state. Instead, it quickly decays to a superposition of the ground and excited states and then stays there. Figure 5.18 shows the probability that the qubit remains in the excited state as a function of time and detuning frequency. Once again it shows a sharp difference at zero detuning.

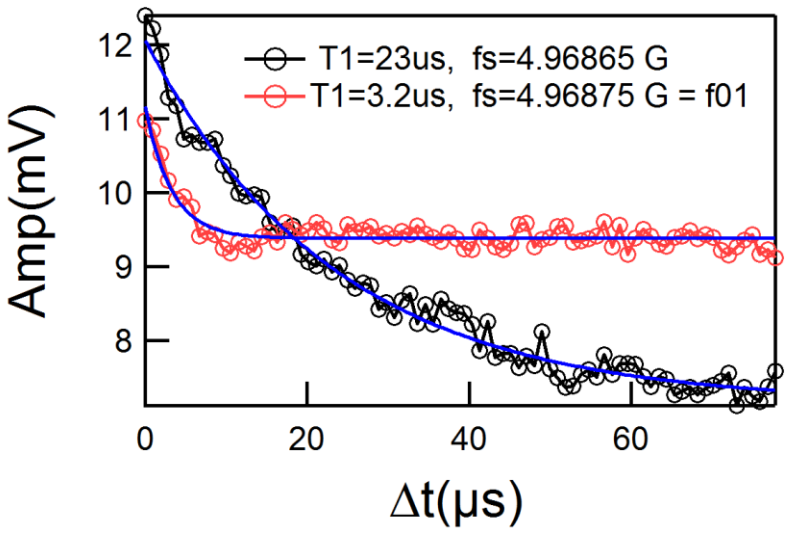

Figure 5.17: T1 was found to vary depending if the frequency the qubit was excited with was on or off resonance. At resonance T1 = 3.2 microseconds. Of resonance T1=

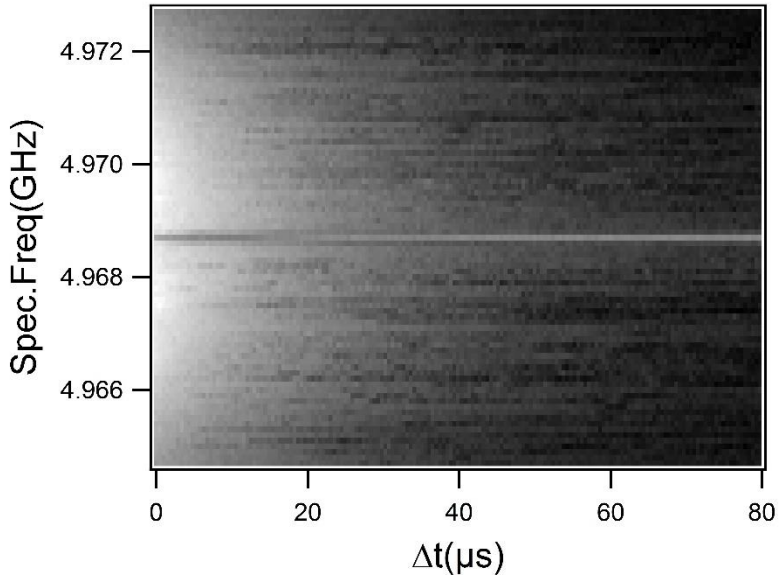

Figure 5.18 Qubit decay at different frequencies.

After measuring T_1, Ramsey fringes were taken to measure T_2*. Due to the experimental setup, Ramsey fringes cannot be taken at zero detuning. This is because the microwave pulse is created by modulating the amplitude of a single microwave carrier, rather than creating replica pulses. This means that the carrier of second π/2 pulse is always in phase with the first pulse, in terms of the measurement, the precession of the qubit state is measured in a rotating reference

frame, which rotates at the spectroscopic frequency. The precession rate, and thus the frequency of the Ramsey fringes are given by the detuning frequency. Since there is no (relative) precession at the qubit frequency, it is impossible to measure Ramsey fringes there. However, T_2* has been measured at different detuning frequencies, which give the same value in this case 5.2 microseconds; this is shown in Figure 5.19.

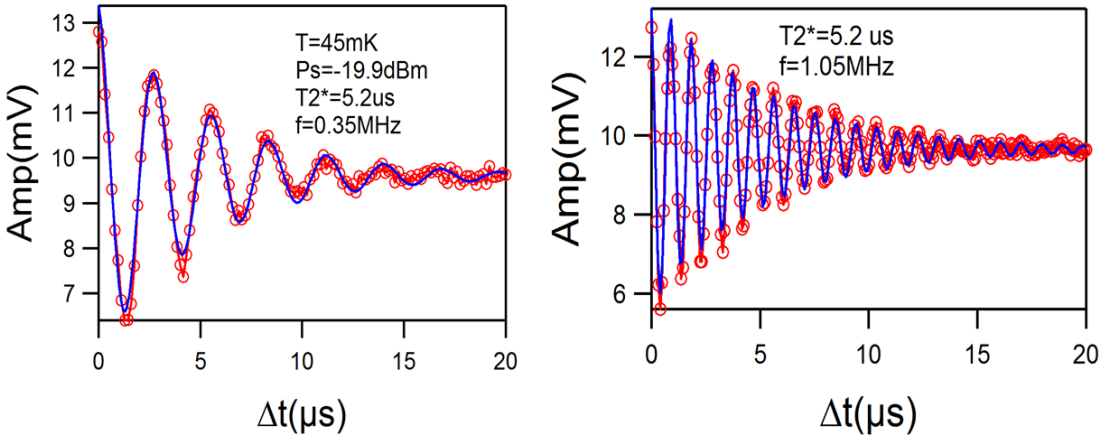

Figure 5.19: Ramsey fringes show the same T_2 at different detuning.*

Next, T_2 was measured using a spin echo measurement. This measurement is shown in Figure 5.20. T2 was found to be enhanced on resonance at 7.8 microseconds compared to 5.8 microseconds off resonance. It should be noted that the qubit does not start in the ground state at zero detuning as it should.

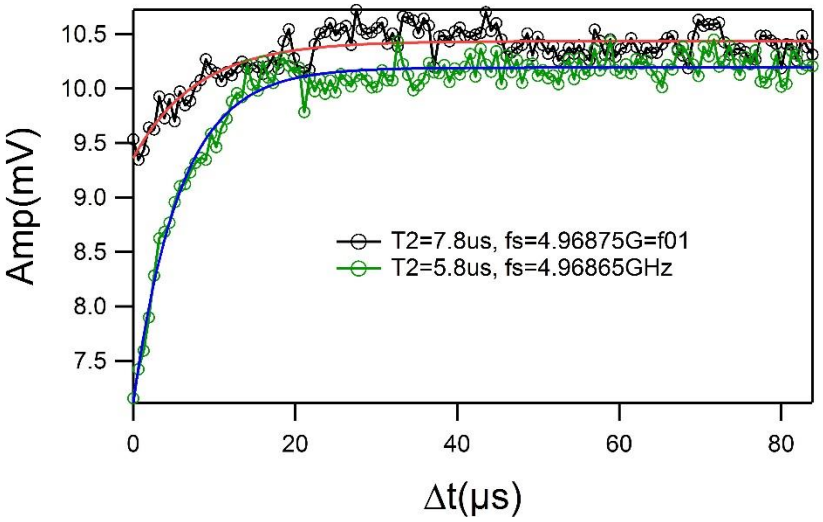

Figure 5.20: Spin Echo measurement gives enhances T2 at qubit frequency.

It turned out that this strange behavior was due to a measurement problem. The pulse which was used to excite the qubit was not turning off completely, i.e. the qubit was being driven continuously at a low power, with a short pulse of high power. This leakage was frequency dependent, and stronger at lower frequencies. It turns out the aluminum nitride coated qubit had the lowest frequency of any of the qubits measured due to slight variations in the oxygen exposure during the barrier growth. The other qubits were of a high enough frequency, that the microwave signal was sufficiently attenuated outside the pulse to avoid interacting with the qubit.

Once the measurement was modified to prevent this leakage, the strange behavior went away. The relaxation time was measured and it had a T1 of about 31 microseconds as shown in Figure 5.21. Ramsey fringes, shown in Figure 5.22, showed T2* to be 5.5 microseconds. Spin echo measurement showed T_2 to also be 5.5 microseconds. This qubit has the longest T1 measured of any of the qubits (though just barely longer than the qubit with in situ surface oxidation which had at T1 of 30 microseconds). T2, however was not remarkable, it was in between the two measurements for the control qubit and less than the in situ oxidized one.

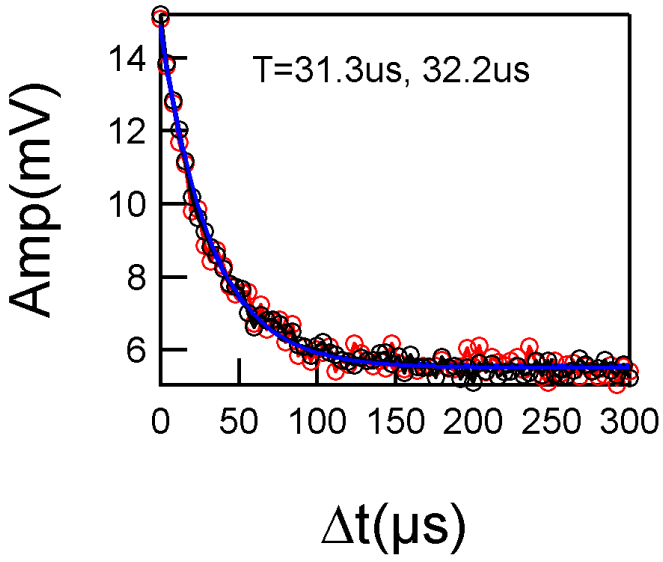

Figure 5.21: T_1 measurement (after eliminating microwave leakage) of aluminum nitride coated qubit shows a T_1 of about 31 microseconds.

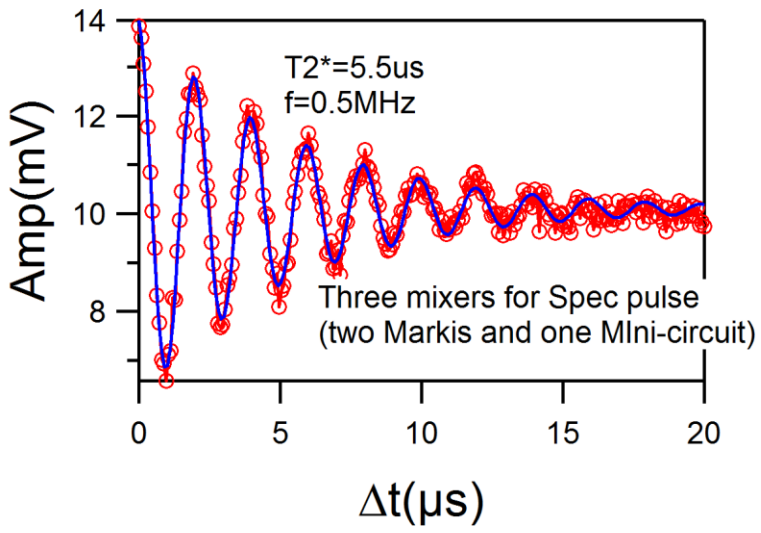

Figure 5.22: Ramsey measurement (after eliminating microwave leakage) of aluminum nitride coated qubit shows T_2 of 5.5 microseconds.*

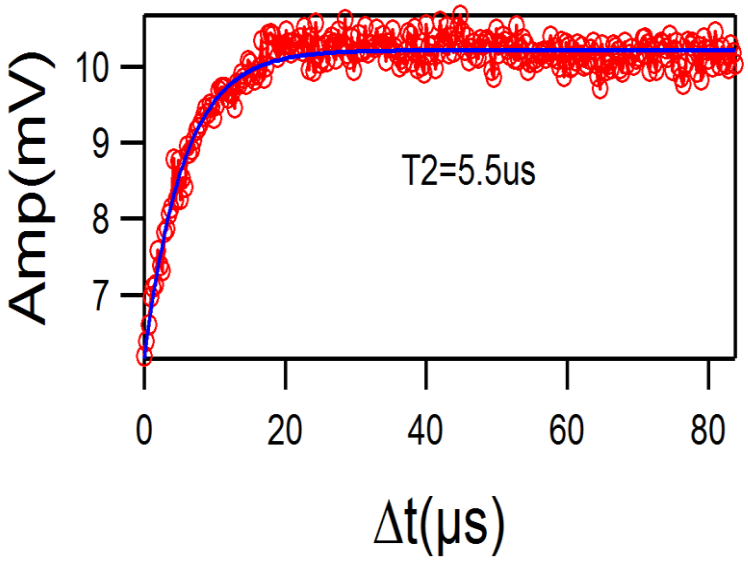

Figure 5.23: Spin echo measurement (after eliminating microwave leakage) of aluminum nitride coated qubit shows T_2 is 5.5 microseconds.

Chapter 6 Summary and Future Work

The goal of this project was to study the effects of using high quality in situ dielectrics on qubit coherence time. This work began by fabricating Josephson junctions out of niobium/aluminum-aluminum oxide/niobium trilayers. A self-aligned process was developed to fabricate the small junctions necessary for the creation of transmon qubits. However these qubits had a much lower coherence time than transmon qubits made from aluminum junctions. Theoretical work by Leppäkangas and Marthaler [47], showed that the coherence time of niobium qubits was limited by quasiparticle tunneling. The coherence time of the niobium qubit as 1.2 microseconds, in rough agreement with a calculation of 3.7 microseconds, calculated using the approach of Leppäkangas and Marthaler. Due to this short coherence time, the focus of the research shifted to studying aluminum qubits, which were not limited by quasiparticles, and thus the surface treatment might have some visible effect on the coherence time.

The work on aluminum started by studying the growth of aluminum on sapphire. It was found that by using c-plane sapphire, which had been annealed in oxygen at 1100°C and dipped in B.O.E., I was able to grow aluminum films with an RMS roughness of only 0.2 nm. Aluminum transmon qubits were then fabricated using the shadowmask process. It was found that surface treatement increased the coherence time of the qubits relative to those that were allowed to oxidize in air, but only slightly. Qubits with a cladding layer of aluminum nitride or diffusive oxidation had the largest T_1. Qubits with diffusive oxidation of the surface exhibited the largest T_2. The results are summarized in Table 6-1.

Overall the in situ oxidation presented the largest increase in coherence from the control qubit. However this increase is modest, which suggests that TLS's in the native oxide are not the limiting factor in coherence time, or that they exist in a similar density in different dielectrics. Given the small sample size (only a single qubit with in situ oxidation), it is difficult to say whether this modest increase is due to the oxidation or is just due to random chance.

Table 6-1: Summary of results of cladding on coherence time

Cladding	T1	T2*	T2
None	26.0	6.2	6.6
None (second device)	20.9, 22.9	3.4	4.2
Diffused Al2O3	30.8, 28.0	7.3, 5.0	8.3, 7.9
Grown Al2O3	26.0	4.2	2.4
Grown AlN	31.3, 32.2	5.5	5.5

6.1 Suggestions for future work

I see a number of possible future experiments to continue this work. First, this work needs to be extended to a larger sample size to verify the results. Next, junctions could be grown with an aluminum nitride barrier in a similar way to the co-deposited barrier as described in section 4.2.3. In addition to further study of the effects of aluminum nitride, other cladding layers could also be tested. One material of particular interest is silicon nitride. It has been shown that encapsulating superconducting quantum interference devices (SQUIDs) in silicon nitride reduces flux noise by an order of magnitude [63]. It would be interesting to see if silicon nitride provides a reduction in two level systems as well. Other possible cladding materials could include silicon dioxide and titanium dioxide.

Another approach is to grow a cladding layer of co-deposited aluminum oxide with a low pressure, to purposefully create oxygen vacancies. One could study the effect of increased oxygen vacancies on decreasing the coherence time.

Appendix A Detailed Description of Self-Aligned Process

In this appendix I will discuss each of the steps in this process. A schematic of this process is outlined in Figure A.1. Starting with an MBE trilayer film (Figure A.1 A), grown as outlined in the previous section, the film is etched into a narrow bar (Figure A.1 B) and then the sidewalls are electrically passivated by coating with a dielectric (Figure A.1 C). Next a wire-up layer of niobium with an aluminum cap is deposited across the device isolation bar (Figure A.1 D). The top electrode is etched away except where it is protected by the aluminum of the wireup (Figure A.1 E), leaving a junction formed where the wire-up crosses the device isolation bar, a schematic of which is shown in Figure A.1 F. Each of these steps is discussed in detail in the rest of this section.

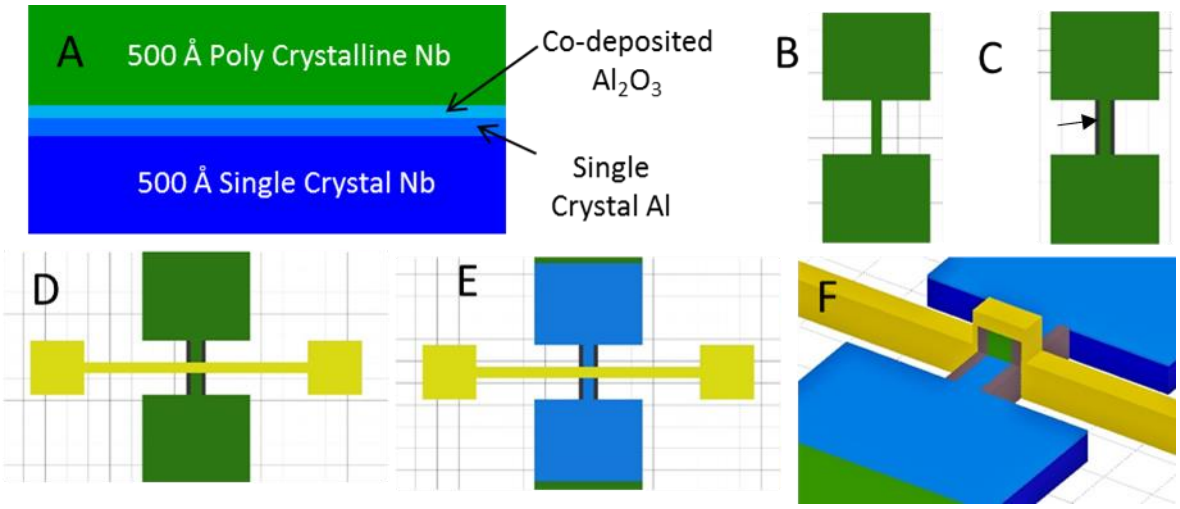

Figure A.1 Schematic of Self aligned process. Images courtesy of Allison Dove.

A.1 Device Isolation Lithography

The first step in the process of creating Josephson junctions (or transmons) from trilayer films is the device isolation etch which etches through all of the layers to the substrate. This defines both the junction width as well as leads and contact pads (and the antenna paddles for transmons). This step requires the patterning of both large features such as contact pads and lead which are on the order of millimeters, and small features such the bar that defines the junction width which is 1 micron or less. We have developed a process that uses both e-beam

lithography to define the small features, and deep UV lithography to define the large features. Both exposures are done on the same photoresist so than only one etching step is needed.

Our choice of resist is PMMA (polymethyl methacrylate) which is a polymer that acts as a positive resist due to the fact that that exposure breaks polymer chains and increases its solubility to methyl isobutyl ketone (MIBK). One advantage of PMMA resist is that its use of organic solvents for its development and removal is completely safe for the niobium and aluminum films, as opposed to the acid/base chemistry of, for instance, AZ resists which can etch metal films. Second PMMA is sensitive to both electron beam lithography and deep UV lithography. Disadvantages or PMMA are that it requires a very large exposure dose, which requires 10s of minutes of exposure with deep UV, and that it has very little resistance to RIE etching, often being etched much faster than the film being etched [64]. The specific resist we use for this step is MicroChem 950PMMA-A4—the 950 refers to the fact that the PMMA is of 950,000 molecular weight, and the A4 meaning that PMMA is dissolved in anisole at a concentration of 4 percent.

The first step to coating our samples with PMMA is to clean them with acetone and IPA, and then bake them at 150 °C on a hotplate to remove water adsorbed to the surface. The sample is then transferred to a spinner, and spun at 2000 rpm for 60 seconds. This is both to allow the sample to cool slightly and to test the vacuum that holds the sample to the spinner. Next PMMA is dropped on to the sample, and it is spun at 500 RPM for 3 seconds to spread the PMMA evenly over the sample, and then the spinner is ramped up to 2000 rpm and spun for 60 seconds to thin the layer of PMMA. According to MicroChem, 950PMMA-A4 spun at 2000 rpm, results in a thickness of approximately 3000 Å [65]. After spinning the sample is baked on the hotplate at 150 °C for 5 minutes to evaporate the solvent. At this point it is put back on the spinner and a second layer of PMMA is spun on using the same procedure (spin dry, drop on PMMA, spin slowly, spin faster) and is baked again to remove the solvent from the second layer. The reason for this double layer of PMMA will be discussed in the in section A.3.

Once the resist is prepared on the sample it is time for the deep UV exposure. This is done in a Karl Suss MJB 3 deep UV mask aligner. Because the intensity of the light changes over time as the bulb wears out, the intensity must be measured before each use to determine the

correct exposure time. The PMMA is exposed for a dose of 4500 mJ/cm^2. A typical intensity is about 1.5 mW/cm^2, which gives a 50 minute exposure. Quartz glass contact masks with chrome patterning are used. Standard soda-lime masks cannot be used because soda-lime glass absorbs deep UV. The mask is cleaned with acetone and IPA before each exposure; if it looks visibly dirty it is cleaned by immersing in a solution of Alconox detergent mixed with de-ionized (DI) water and scrubbed gently with a cotton ball. The mask aligner allows the user to move the sample relative to the mask using micrometers, which rotate the sample and move it in the x and y direction while looking down through the mask through a microscope. Once the sample is aligned, it is brought into contact with the mask and exposed for the desired time. This mask aligner can define features down to about 1 micron, limited by contact and diffraction.

After deep UV exposure the PMMA is developed in a mixture of 1 part MIBK to 3 parts IPA for 60 seconds. The development is stopped by dunking the sample into a bath of IPA and then blowing it dry with nitrogen. Afterwards it is baked at 100 °C for 90 seconds to remove any solvent from the development.

At this stage the sample is loaded into the e-beam lithography system. Electron beam lithography works by scanning a beam of electrons across the surface of the sample in order to expose a pattern in the resist. The e-beam lithography system I used is the Raith e-line. The system in essence consists of a scanning electron microscope (SEM) column and a precision controlled x-y stage, along with software to draw the desired pattern, rather than just scanning over a given region as in an SEM. Electron beam lithography has the advantage can pattern features down to about 10 nm. Since it writes following a pattern file, changes to the pattern are easily made, as opposed to optical lithography which requires a new mask to be created to make any changes to the pattern. The disadvantage of e-beam lithography is that it is slow to write large areas.

After loading the sample into the Raith, the beam voltage is ramped up to the desired setting. I used a beam voltage of 30 kV. Next the desired aperture is selected. A smaller aperture increases the maximum resolution, but lowers the beam current, increasing the necessary write time, and reduces visibility, making the beam tuning procedure more difficult. I used a 30 micron

aperture, which is a good balance between resolution and beam current. Once the aperture and voltage are selected, the beam current is measured, and used to calculate the dwell time necessary to give each region the desired dose. A typical beam current at these settings was 0.32 nA, and I used a dose of 560 $\mu A/cm^2$. Next the beam is focused and the stigmation and aperture alignment are adjusted to give a small round beam.

Once the beam is tuned up the sample is aligned to the pattern file, by finding the location of alignment marks that had been patterned in the PMMA during the deep UV lithography. The pattern is tiled into writefields, which are regions that are written by sweeping the beam, then the stage is moved to center on the next writefield. Smaller writefields give greater accuracy, but if a feature extends across the boundary between two writefields, there can be stitching errors due to errors in the positioning of the stage. My work was done using a 200 micron writefield, which was large enough to contain all of the features that were written using e-beam lithography. To improve the accuracy of the alignment, I used local alignment marks what were inside the writefield of each written feature.

After e-beam lithography is finished, the sample is developed again. It is once again developed in 3:1 IPA:MIBK, but this time the developer has been left in an ice bath for 30 minutes, where it stabilizes at a temperature of 2 °C. This low temperature development has two benefits. First a lower temperature development requires a higher dose to fully expose, and since the deep UV portion of the pattern was exposed for room temperature development, the effects of overdevelopment are minimized. The second benefit of cold development is that it increases the contrast of the PMMA, i.e. there is a sharper cutoff between being fully exposed and being unexposed [66]. After development the sample is again post-baked at 100 °C for 90 seconds.

A.2 Device Isolation Etch

Once the lithography is complete the etch needs to be performed. The first layer that need to be etched is the niobium counter electrode. This etch is done with a reactive ion etcher (RIE). An RIE works by exciting a plasma in a precursor gas, which ionizes it and accelerates the ions toward the substrate, which develops a potential difference relative to the plasma due to the build-up of charge from these ions. The ions interact with the material being etched both by

physical sputtering and chemical reaction with the ion. RIE has the advantage that under the proper conditions it can be very anisotropic, giving nearly vertical sidewalls and little undercut. It can also be very selective to different materials. The etching done for this work was done in a March CS-1701 RIE System, which has been modified with the addition of a turbo pump to give a lower base pressure and thus fewer contaminants in the precursor gas, and with a throttling valve placed between the pump and the RIE chamber to control the pressure. This RIE system has a very high etch rate of PMMA compared to the etch rate of niobium, so I developed an etch recipe that etched niobium well while etching PMMA the least. This etch is referred to as the standard niobium etch. This etch recipe and others used in this section are described below

Standard niobium etch Gas: 40 sccm of SF_6, Pressure: 200 mTorr, RF Power 35 W, Time: Variable

Standard Clean Gas: 43 sccm of O_2, Pressure: 200 mTorr, RF Power 200 W, Time: 600s

Oxygen Ash Gas: 43 sccm of O_2, Pressure: 200 mTorr, RF Power 35 W, Time: Variable

The first step in preparing the RIE to etch niobium is to run the standard clean recipe. This is to remove any photoresist that has been re-deposited on the walls of the chamber during previous etches. Afterwards the standard niobium etch recipe is run for 3 minutes, to season the walls of the chamber. Next the sample is loaded and the chamber is pumped for 5 minutes, in order to achieve base pressure. Next the oxygen ash recipe is run for 10 seconds, this is to remove any photo-resist residue that left in the exposed regions after development and give a clean niobium oxide surface for etching. Next the standard niobium etch recipe is run, for a length of time to over-etch the top electrode. For typical thickness a 50 second etch is used. The etch stops completely at the barrier underneath. The over etch is used to ensure a clean aluminum oxide surface.

Fluorine chemistry is unable to etch aluminum/aluminum oxide, chlorine based gasses are necessary to etch these with and RIE. Chlorine based gasses require an RIE system with a load lock to prevent venting residual gas from being vented into the air, and so cannot be safely used with this RIE. Chlorine based RIE also is much more aggressive in attacking photoresist than SF6 is, it is also not selective between aluminum and niobium. Because of these reasons, a wet

chemical etch was used to remove the aluminum layer. The etchant chosen was Transene Aluminum etchant type D (referred in this document simply as Transene), a commercial etchant formulated specifically to etch aluminum. It contains phosphoric acid, sodium-m-nitrobenzene sulfonate, and acetic acid. It is quite viscous which helps minimize undercutting. It also does not attack niobium.

Transene etches better at elevated temperatures. To achieve this about 40 mL of Transene is poured into a small beaker which is placed in a water bath on a hotplate controlled with a temperature probe. The temperature probe is placed in the water and the hotplate is set to a temperature of 50 °C. It is then left to stabilize for 10 minutes. The sample is then etched until the aluminum is fully etched, this is evident from a color change, plus another 10 seconds. This usually takes 70-80 seconds.

After the aluminum etch, the RIE is once again seasoned with a 3 minute run of the standard niobium etch recipe. Then the sample is loaded into the RIE and it is pumped for 5 minutes. Then the standard niobium etch is run for (typically) 50 seconds, to etch the base niobium electrode. After this etch is complete the oxygen ash is run for 30 seconds, to remove any polymer that may deposited from the fluorine interacting with the photoresist. At this stage the device isolation etch is complete, and the sidewalls now need to be electrically isolated to prevent the wire up from shorting to the base electrode.

A.3 Sidewall Dielectric Coating

The sidewalls of the trilayer need to be electrically isolated to prevent shorting to the wireup layer. However, the top of the counter electrode layer must remain uncovered so that the wire up layer can make contact. This is accomplished by coating the sample with a dielectric while the photoresist which was used to define the device isolation etch is still in place. This photoresist protects the top surface from being coated, and then, when the photoresist is removed, only the dielectric which was deposited directly on the substrate or sidewalls remains.

The dielectric is deposited by means of Atomic layer deposition (ALD). Atomic layer deposition is a process that uses two (or) precursors that react on the surface of a sample, in a self-limiting way, to deposit a film, one molecular layer at a time. Typically the process works by

exposing the sample to the first precursor, which for metal oxides, is often (and for the ALD all depositions in the present work) water vapor. The water vapor adsorbs to the surface of the sample, and residual water vapor is flush away by a purge gas (in this case nitrogen). Next the second precursor is introduced. This is typically an organometallic compound, such as trimethyl aluminum. This second precursor reacts with the adsorbed water layer, creating a single layer of the metal oxide. This process is repeated until the desired thickness is achieved. ALD has the advantage that it provides a conformal coating, not directional like many other deposition techniques. It also allows for a precisely controlled thickness. It has the disadvantage that it is a slow process, with each layer taking anywhere from a few seconds to a few minutes. The depositions for this project were done in a Cambridge Nanotech Savannah ALD system.

We used aluminum oxide as out dielectric. The precursors for aluminum oxide are water vapor and trimethyl aluminum. The deposition chamber is heated to 100 °C, the first precursor (water vapor) is introduced into the chamber, it is allowed to react for 5 seconds, then it is pumped out and the chamber is purged for 65 seconds, then the second precursor (trimethyl aluminum) is introduced, allowed to react for 5 seconds, and then purged for 65 seconds. This adds up to 140 seconds per layer. Before the device isolation etch is started, the recipe for depositing aluminum oxide is started with the ALD empty. This is to coat the inside of the chamber, covering any contamination that might be in the chamber. During the etching, enough time goes by that the walls of the ALD chamber have been coated with at least 15 layers. After the device isolation etch is finished, the sample is removed from the RIE and immediately loaded into the ALD chamber. It is allowed to thermalize with the floor of the chamber for 5 minutes, and then 40 layers are deposited.

After the ALD alumina is deposited, the photoresist needs to be removed and the alumina lifted off. This turns out to not be easy. Because the ALD alumina is conformal, it completely encapsulates the photoresist, preventing solvent from reaching the photoresist and removing it (see Figure A.2). Attempts to break up the alumina coating the photoresist by sonicating in acetone were able to remove the alumina from the top of large features, but it left alumina coated photoresist on top of small features as shown in the left side of Figure A.3.

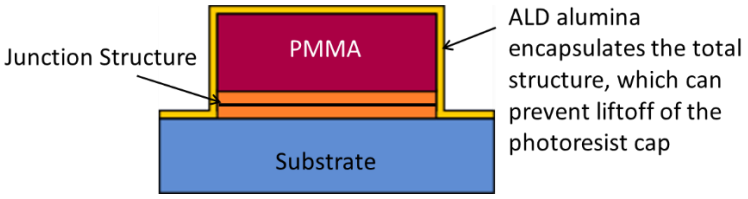

Figure A.2: ALD Alumina encapsulates photoresist, preventing liftoff

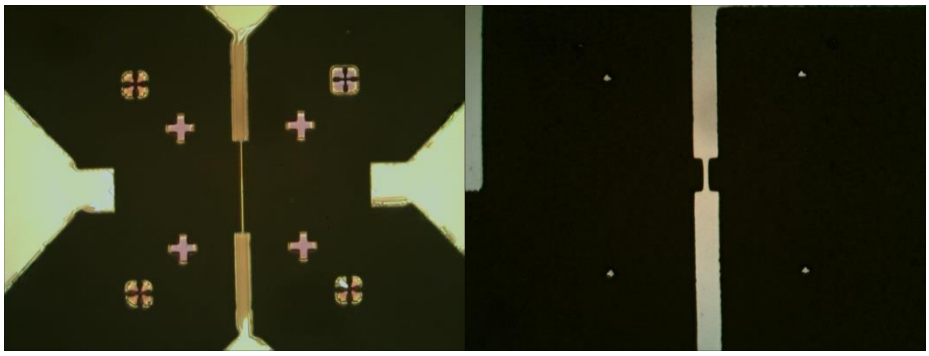

Figure A.3: Left Sonication in acetone removes ALD Alumina from the top of large features, but not from small features. Right: Wiping with cotton while submerged in Remover PG, then placing in agitated, heated Remover PG completely removes ALD alumina.

A procedure was found to successfully remove the alumina and photoresist. The first step is to hold the sample vertically in a bath of Remover PG that has been heated to 80 °C and is being agitated by a magnetic stirring bar spinning at 800 RPM for 10 minutes. Remover PG is an N-Methyl-2-pyrrolidone (NMP) based solvent made by MicroChem, designed for complete removal of PMMA. Then the sample is placed in a petri dish filled with Remover PG and wiped gently with a cotton ball. Then it is placed back into the spinning Remover PG for another 10 minutes. This process is repeated until the sample is visibly clean in a microscope. It was also found that thicker PMMA improved this lift off, which is why PMMA was spun on twice to get a double thick layer before the lithography as mentioned in section Appendix A. The right side of Figure A.3 shows the clean surface of the top electrode after successful liftoff of alumina.

The use of ALD deposited titanium dioxide was also investigated. It has been found that while ALD deposited alumina will grow on PMMA, ALD deposited titanium dioxide will not [67]. The precursor for the deposition of titanium dioxide is Tetrakis(dimethylamido)titanium (TDMAT). The growth chamber temperature is 200 °C; each precursor is allowed to react for 1

second and is purged for 10 seconds. It was found that in order to achieve a good insulating sidewall coating, with no leakage current, the titania had to be grown 400 layers thick. It was indeed found that the titania did not grow on the PMMA, and thus the PMMA was able to be removed simply by soaking the sample in acetone. Unfortunately do to the extreme thickness of titania needed, a single sample used up nearly all of the precursor that the ALD system held, and so this was not viable for us.

A.4 Wire up

At this point, it is time for the wire up step. This step deposits niobium to make contact with the counter electrode. On top of the niobium, aluminum is deposited to act as an etch mask. Aluminum is chosen, because it is resistant to the RIE niobium etch. Another advantage of aluminum is that it is also a superconductor, and can be left in place without degrading the quality of the qubit.

The first step in the wire up is lithography. This step also uses both deep UV and e-beam lithography, however since there are now features to align both of these patters to, it can be done with a single development. This step uses a different resist profile than the one used for the device isolation etch. To prepare this resist, first the sample is baked on the hotplate at 150 °C for 3 minutes, then MicroChem (8.5) MMA EL-9 copolymer is spun on at 2000 RPM. This is a mixture of PMMA and 8.5% methacrylic acid at a 9% solution in ethyl lactate. This spins to a thickness of about 4500 Å thick [65]. It requires very little exposure to develop MMA so it overexposes when it receives the full dose necessary to expose PMMA. This causes the MMA to be undercut relative to the PMMA that will be spun on top of it, which aids in lift off. The sample is then baked at 150 °C for 5 minutes. Then 950 PMMA A2 is spun on 4000 RPM which gives a thickness of about 250 Å [65]. Then it is baked again at 150 °C for 5 minutes. Next aquaSAVE is spun on at 1500 RPM and baked at 70 °C for 5 minutes. AquaSAVE is a water soluble conductive polymer made by Mitsubishi Rayon. Because the substrate is insulating, and the metallic film has been patterned into isolated islands, the sample will have a tendency to charge up during e-beam lithography. AquaSAVE prevents this by providing a conducting layer over the entire sample, allowing a path for electrons to discharge.

After the resist is prepared, the sample is loaded into the e-beam lithography system and the pattern is written with an exposure dose of 500 μC/cm^2, which is slightly higher than the exposure for the device isolation step. This is necessary due to the addition of aquaSAVE on top of the resist. Next, the aquaSAVE is removed by rinsing in de-ionized water for 60 seconds. This is necessary because the aquaSAVE absorbs deep UV light, and would prevent exposure. The sample is then exposed in the deep UV mask aligner for a dose of 6000 mJ/cm^2, a higher dose than in the device isolation step to expose properly for cold development. Then the sample is developed in 3:1 IPA:MIBK at 2 °C.

At this point the sample is loaded into a magnetron sputtering system. In sputtering, a high voltage is used to cause free electrons to collide with a low pressure non-reactive gas (in this case argon) knocking electrons off, leaving positively charged ions. The ions are then accelerated toward the cathode, which is made of the source material. When they ions hit the source material the kinetic energy is transferred to the target and atoms and clusters of atoms are ejected, which then deposit on the substrate. Magnetron sputtering adds a magnetic field to confine the free electrons increasing the ionization rate of the gas.

After the sample is loaded into the sputtering system it is pumped for an hour to reach a base pressure of about 2x10^{-7} Torr. Then the sample is given a brief ion mill (approximately 3 seconds) to clean up the surface, and allow the wire up deposition to stick well. Ion milling is essentially the reverse of sputtering, argon ions are accelerated at the substrate and atoms at the surface are ejected. After the ion mill 900 Å of niobium is deposited, at a pressure of 6 mTorr and with an emission current of 0.5 A. This sample is rocked back and forth during this deposition to aid step coverage. After the niobium deposition, 360 Å of aluminum is deposited at an argon pressure of 10 mTorr and a current of 0.15 A, also while rocking the sample back and forth.

After the deposition, the niobium and aluminum are lifted off by soaking in acetone for 60 minutes. The undercut in the photoresist, from the PMMA/MMA bilayer ensures that the metal deposited directly on the substrate is not joined to the metal on top of the photoresist. When the photoresist is dissolved the metal deposited on the substrate remains while the metal

on top of the photoresist is freed, and is rinsed away when the substrate is removed from the acetone bath and sprayed with acetone.

After the lift off has been completed, the substrate is loaded into the RIE (which had previously had a standard clean recipe run), and allowed to pump for the usual 5 minutes. It is then given a 10 second oxygen ash. Next it is removed from the RIE and is dipped in 1 part sulfuric acid (H2SO4) in 5 parts deionized water for 40 seconds. These steps are to ensure that all of the photoresist residue has been removed, to ensure good etching. The sample is the placed back in the RIE, pumped for 5 minutes, and then the standard niobium etch is run for 60 seconds. This etches away the top electrode everywhere that it is not covered by the wire up, which has aluminum on top that acts as an etch mask. This leaves a Josephson junction formed where the wire crosses the device isolation bar. Figure A.4 shows a micrograph of a completed junction, which has an area of 1 square micron.

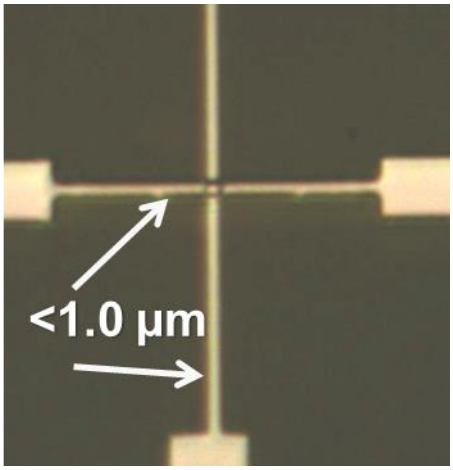

Figure A.4: Micrograph of a completed junction, with an area of 1 square micron

References

[1] P. W. Shor, "Algorithms for quantum computation: discrete logarithms and factoring," in *35th Annual Symposium on Foundations of Computer Science*, Los Alamitos, CA, 1994.

[2] L. K. Grover, "Quantum mechanics helps in searching for a needle in a haystack," *Physical Review Letters,* vol. 79, no. 2, pp. 325-328, 1997.

[3] R. P. Feynman, "Simulating Physics with Computers," *International Journal of Theoretical Physics,* vol. 21, pp. 467-888, 1982.

[4] T. D. Ladd, F. Jelezko, R. Laflamme, Y. Nakamura, C. Monroe and J. L. O'Brien, "Quantum computers," *Nature,* vol. 464, p. 45, 2010.

[5] J. L. O'Brien, A. Furusawa and J. Vuckovic, "Photonic quantum technologies," *Nature Photonics,* vol. 3, p. 687, 2009.

[6] J. P. Home, D. Hannek, J. D. J. J. M. Amini, D. Leibfried and D. J. Wineland, "Complete Methods Set for Scalable Ion Trap Quantum Information Processing," *Science,* vol. 325, p. 1227, 2009.

[7] N. A. Gershenfeld and I. L. Chuang, "Bulk Spin-Resonance Quantum Computation," *Science,* vol. 276, p. 350, 1997.

[8] M. Steffen, "Viewpoint: Superconducting Qubits Are Getting Serious," *Physics 4,* vol. 103, 2011.

[9] Y. Nakamura, Y. A. Pashkin and J. S. Tsa, "Coherent control of macroscopic quantum states in a single-Cooper-pair box," *Nature,* vol. 398, p. 786, 1999.

[10] C. Rigetti, J. M. Gambetta, S. Polett, B. L. T. Plourde, J. M. Chow, A. D. Córcoles, J. A. Smolin, S. T. Merkel, J. R. Rozen, G. A. Keefe, M. B. Rothwell, M. B. Ketchen and M.

Steffen, "Superconducting qubit in a waveguide cavity with a coherence time approaching 0.1 ms," *Physical Review B,* vol. 86, p. 100506, 2012.

[11] R. McDermott, "Materials Origins of Decoherence in Superconducting Qubits," *IEEE Transactions on Applied Superconductivity,* vol. 19, p. 2, 2009.

[12] D. Deutsch, "Quantum Theory, the Church-Turing Principle and the Universal Quantum Computer," *Proc. R. Soc. Lond A,* no. 400, pp. 97-117, 1985.

[13] D. Deutsch and R. Jozsa, "Rapid Solution of Problems by Quantum Computation," *Proceedings of the Royal Society of London Series A,* vol. 439, no. 1907, pp. 553-558, 1992.

[14] M. A. Nielsen and I. L. Chuang, Quantum Compuation and Quantum Information, Cambridge: Cambridge University Press, 2010.

[15] D. P. DiVincenzo, "The Physical Implementation of Quantum Computation," *Fortschr Phys,* vol. 48, no. 9, pp. 771-783, 2000.

[16] B. D. Josephson, Superconductivity, R. D. Parks, Ed., New York: Marcel Dekker, 1969.

[17] M. H. Devoret and J. M. Martinis, "Course 12 Superconducting qubits," *Les Houches,* vol. 79, pp. 443-485, 2004.

[18] B. D. Joshephson, "Possible new effects in superconductive tunnelling," *Physics Letters,* vol. 1, no. 7, p. 251, 1962.

[19] T. Van Duzer and C. W. Turner, Superconductive Devices and Circuits, 2nd ed., Upper Saddle River, New Jersey: Prentice-Hall, 1999.

[20] Wikipedia, "Superconducting tunnel junction," 2013. [Online]. Available: http://en.wikipedia.org/wiki/Superconducting_tunnel_junction. [Accessed 10 April 2014].

[21] V. Bouchiat, D. Vion, P. Joyez, D. Esteve and M. H. Devoret, "Quantum coherence with a single Cooper pair," *Physica Scripta,* vol. T76, p. 165, 1998.

[22] J. M. Martinis, S. Nam and J. Aumentado, "Rabi Oscillations in a Large Josephson-Junction Qubit," *Physicsl Review Letters,* vol. 89, p. 117901, 2002.

[23] T. P. Orlando, J. E. Mooij, L. Tian, C. H. van der Wal, L. S. Levitov, S. Lloyd and J. J. Mazo, "Superconducting Persistent-Current Qubit," *Physical Review B,* vol. 60, no. 22, pp. 15398-15413, 1999.

[24] J. Koch, T. M. Yu, J. Gambetta, A. A. Houck, D. I. Schuster, J. Majer, A. Blais, M. H. Devoret, S. M. Girvin and R. J. Schoelkopf, "Charge-insensitive qubit design derived from the Cooper pair box," *PHYSICAL REVIEW A,* vol. 76, p. 042319, 2007.

[25] A. Cottet, *Implementation of a quantum bit in a superconducting circuit, Ph.D. Thesis,* Universite Paris VI, 2002.

[26] J. Clarke and F. K. Wilhelm, "Superconducting Quantum Bits," *Nature,* vol. 453, no. 19, pp. 1031-1042, 2008.

[27] E. M. Purcell, "Spontaneous emission probabilities at radio frequencies," *Physical Review,* vol. 69, p. 681, 1946.

[28] H. Paik, D. I. Schuster, L. S. Bishop, G. Kirchmair, G. Catelani, A. P. Sears, B. R. Johnson, M. J. Reagor, L. Frunzio, L. I. Glazman, S. M. Girvin, M. H. Devoret and R. J. Schoelkopf, "Observation of High Coherence in Josephson Junction Qubits Measured in a Three-Dimensional Circuit QED Architecture," *Physical Review Letters,* vol. 107, p. 240501, 2011.

[29] W. D. Oliver and P. B. Welander, "Materials in superconducting quantum bits," *MRS Bulletin,* vol. 38, p. 816, 2013.

[30] I. I. Rabi, "Space Quantization in a Gyrating Magnetic Field," *Physical Review,,* vol. 51, p. 652, 1937.

[31] A. Ustinov, "Superconductivity Lecture 12," [Online]. Available: http://www.phi.kit.edu/ee2.bak/scripts/Superconductivity-12.pdf. [Accessed 13 April 2014].

[32] N. F. Ramsey, "A Molecular Beam Resonance Method with Separated Oscillating Fields," *Physical Review,* vol. 78, p. 695, 1950.

[33] D. Vion, A. Aassime, A. Cottet, P. Joyez, H. Pothier, C. Urbina, D. Esteve and M. H. Devoret, "Manipulating the Quantum State of an Electrical Circuit," *Science,* vol. 296, p. 886, 2002.

[34] J. A. Schreier, A. A. Houck, J. Koch, D. I. Schuster, B. R. Johnson, J. M. Chow, J. M. Gambetta, J. Majer, L. Frunzio, M. H. Devoret, S. M. Girvin and R. J. Schoelkopf, "Suppressing charge noise decoherence in superconducting charge qubits," *Physical Review B,* vol. 77, p. 180502, 2008.

[35] R. W. Simmonds, K. M. Lang, D. A. Hite, S. Nam, D. P. Pappas and J. M. Martinis, "Decoherence in Josephson Phase Qubits from Junction Resonators," *Physical Review Letters,* vol. 93, p. 077003, 2004.

[36] B. L. T. Plourde, T. L. Robertson, P. A. Reichardt, T. Hime, S. Linzen, C.-E. Wu and J. Clarke, "Flux qubits and readout device with two independent flux lines," *Physical Review B,* vol. 72, p. 060506, 2005.

[37] C. T. Rogers and R. A. Buhrman, "Nature of Single-Localized-Electron States Derived from Tunneling Measurements," *Physical Review Letters,* vol. 55, p. 859, 1985.

[38] R. T. Wakai and D. J. van Harlingen, "Low-Frequency Noise and Discrete Charge Trapping in Small-Area Tunnel Junction DC SQUID's," *Applied Physics Letters,* vol. 49, no. 10, pp. 593-595, 1986.

[39] C. T. Rogers and R. A. Buhrman, "Composition of 1/f Noise in Metal-Insulator-Metal Tunnel Junctions," *Physical Review Letters,* vol. 53, no. 13, pp. 1272-1275, 1984.

[40] D. J. van Harlingen, T. L. Robertson, B. Plourde, P. A. Reichardt, T. A. Crane and J. Clarke, "Decoherence in Josephson-junction qubits due to critical-current fluctuations," *Physical Review B,* vol. 70, no. 6, pp. 4517-4530, 2004.

[41] L.-C. Ku and C. C. Yu, "Decoherence of a Josephson qubit due to coupling to two-level systems," *Physical Review B,* vol. 72, p. 024526, 2005.

[42] S. Oh, K. Cicak, J. S. Kline, M. A. Sillanpää, K. D. Osborn, J. D. Whittaker, R. W. Simmonds and D. P. Pappas, "Elimination of two level fluctuators in superconducting quantum bits by an epitaxial tunnel barrier," *Physicsal Review B,* vol. 74, p. 100502, 2006.

[43] P. B. Welander, T. J. McArdle and J. Eckstein, "Reduced leakage current in Josephson tunnel junctions with codeposited barriers," *Applied Physics Letters,* vol. 97, no. 23, p. 233510, 2010.

[44] J. Wenner, R. Barends, R. C. Bialczak, Y. Chen, J. Kelly, E. Lucero, M. Mariantoni, A. Megrant, P. J. J. OMalley, D. Sank, A. Vainsencher, H. Wang, T. C. White, Y. Yin, J. Zhao, A. N. Cleland and J. M. Martinis, "Surface loss simulations of superconducting coplanar waveguide resonators," *Applied Physics Letters,* vol. 99, no. 11, p. 113513, 2011.

[45] A. Megrant, C. Neill, R. Barends, B. Chiaro, Y. Chen, L. Feigl, J. Kelly, E. Lucero, M. Mariantoni, P. J. J. O'Malley, D. Sank, A. Vainsencher, J. Wenner, T. C. White, Y. Yin, J. Zhao, C. J. Palmstrom, J. M. Martinis and A. N. Cleland, "Planar superconducting resonators with internal quality factors above one million," *Applied Physics Letters,* vol. 100, p. 113510, 2012.

[46] J. B. Chang, M. R. Vissers, A. D. Córcoles, M. Sandberg, J. Gao, D. W. Abraham, J. M. Chow, J. M. Gambetta, M. Beth Rothwell, G. A. Keefe, M. Steffen and D. P. Pappas, "Improved superconducting qubit coherence using titanium nitride," *Applied Physics Letters,* vol. 103, p. 012602, 2013.

[47] J. Leppäkangas and M. Marthaler, "Fragility of flux qubits against quasiparticle tunneling," *Physical Review B,* vol. 85, p. 144503, 2012.

[48] G. Catelani, S. E. Nigg, S. M. Girvin, R. J. Schoelkopf and L. I. Glazman, "Decoherence of superconducting qubits caused by quasiparticle tunneling," *Physical Review B,* vol. B86, p. 184514, 2012.

[49] J. J. Toppari, T. Kühn, A. P. Halvari, M. L. J. Kinnunen and G. S. Paraoanu, "Cooper-pair resonances and subgap Coulomb blockade in a superconducting single-electron transistor," *Physical Review B,* vol. 76, p. 172505 , 2007.

[50] P. B. Welander, *Epitaxial Aluminum Oxide Thin Films on Niobium (110): A Study of Their Growth and Their Use Superconducting Tunnel Junctions, Ph.D. Thesis,* University of Illinois at Urbana Champaign, 2007.

[51] S. M. Durbin, J. .. Cunningham and C. P. Flynn, "Growth of Single Crysta lMetal Superlattices in Chosen Orientations," *Journal of Physics F: Metal Physics,* vol. 12, p. L75, 1982.

[52] G. Gutekunst, J. Mayer and M. Rühle, "Atomic structure of epitaxial Nb-Al2O3 interfaces I. Coherent regions," *Philosophical Magazine A,* vol. 75, no. 5, p. 1329, 1997.

[53] A. Wildes, J. Mayer and K. Theis-Bröhl, "The growth and structure of epitaxial niobium on sapphire," *Thin Solid Films,* vol. 401, p. 7, 2001.

[54] T. Wadayama, "Reflection High Energy Electron Diffraction : RHEED," Tohoku University, [Online]. Available: http://www.material.tohoku.ac.jp/~kaimenb/e_genri.html. [Accessed 13 March 2014].

[55] V. Ambegaokar and A. Baratoff, "Tunneling Between Superconductors," *Physical Review Letters,* vol. 11, p. 486, 1963.

[56] R. C. Dynes, V. Narayanamurti and J. P. Garno, "Direct measurement of quasiparticle-lifetime broadening in a strong-coupled superconductor," *Physical Review Letters,* vol. 41, p. 1509, 1978.

[57] H. Paik, S. K. Dutta, R. M. Lewis, T. A. Palomaki, B. K. Cooper, R. C. Ramos, H. Xu, A. J. Dragt, J. R. Anderson, C. J. Lobb and F. C. Wellstood, "Decoherence in dc SQUID phase qubits," *Physical Review B,* vol. 77, p. 214510, 2008.

[58] D. L. Creedon, Y. Reshitnyk, W. Farr, J. M. Martinis, T. L. Duty and M. E. Tobar, "High Q-factor sapphire whispering gallery mode microwave resonator at single photon energies and millikelvin temperatures," *Applied Physics Letters,* vol. 98, p. 222903, 2011.

[59] G. J. Dolan, "Offset masks for liftoff photoprocessing," *Applied Physics Letters,* vol. 31, no. 5, p. 337, 1977.

[60] Zeon Corporation, "ZEP 520A Technical Report," October 2010. [Online]. Available: http://www.zeonchemicals.com/pdfs/ZEP520A.pdf.

[61] A. Blais, R.-S. Huang, A. Wallraff, S. Girvin and R. Schoelkopf, "Cavity quantum electrodynamics for superconducting electrical circuits: An architecture for quantum computation," *Phys. Rev. A,* vol. 69, no. 6, p. 062320, 2004.

[62] M. D. Reed, L. DiCarlo, B. R. Johnson, L. Sun, D. I. Schuster, L. Frunzio and R. J. Schoelkopf, "High-Fidelity Readout in Circuit Quantum Electrodynamics Using the Jaynes-Cummings Nonlinearity," *Physical Review Letters,* vol. 105, p. 173601, 2010.

[63] S. L. Sendelbach, *Investigations of 1/f Flux Noise in Superconducting Quantum Circuits, Ph.D. Thesis,* Madison: University of Wisconsin, 2013.

[64] S. A. Campbell, The Science and Engineering of Microelectronic Fabrication, New York: Oxford University Press, 1996.

[65] MicroChem Corp., "Nano PMMA and Copolymer," 2001. [Online]. Available: http://www.microchem.com/pdf/PMMA_Data_Sheet.pdf.

[66] B. Cord, J. Lutkenhaus and K. K. Berggren, "Optimal temperature for development of poly(methylmethacrylate)," *Journal of Vacuum Science & Technology B,* vol. 25, p. 2007, 2007.

[67] E. Färm, M. Kemell, M. Ritala and M. Leskelä, "Selective-Area Atomic Layer Deposition Using Poly(methyl methacrylate) Films as Mask Layers," *The Journal of Physical Chemistry C,* vol. 112, no. 40, pp. 15791-15795, 2008.